ANALYSIS OF THERMO-MECHANICAL CHARACTERISTICS OF THE LENS™ PROCESS FOR STEELS USING THE FINITE ELEMENT METHOD

By

Phillip Roger Pratt

A Thesis
Submitted to the Faculty of
Mississippi State University
in Partial Fulfillment of the Requirements
for the Degree of Master of Science
in Mechanical Engineering
in the Department of Mechanical Engineering

Mississippi State, Mississippi

December 2008

ANALYSIS OF THERMO-MECHANICAL CHARACTERISTICS OF THE LENS™ PROCESS FOR STEELS USING THE FINITE ELEMENT METHOD

By

Phillip Roger Pratt

Approved:

Sergio D. Felicelli Professor of Mechanical Engineering (Thesis Director)	John T. Berry Professor of Mechanical Engineering (Committee Member)
Mark F. Horstemeyer Professor of Mechanical Engineering (Committee Member)	Steven R. Daniewicz Professor of Mechanical Engineering (Graduate Coordinator)

Sarah M. Rajala
Dean of the Bagley College of Engineering

Name: Phillip Roger Pratt

Date of Degree: May 2, 2008

Institution: Mississippi State University

Major Field: Mechanical Engineering

Major Professor: Sergio D. Felicelli

Title of Study: ANALYSIS OF THERMO-MECHANICAL CHARACTERISTICS OF THE LENS™ PROCESS FOR STEELS USING THE FINITE ELEMENT METHOD

Pages in Study: 105

Candidate for Degree of Master of Science

Laser Engineered Net Shaping (LENS™) is a rapid-manufacturing procedure that involves complex thermal, mechanical, and metallurgical interactions. The finite element method (FEM) may be used to accurately model this process, allowing for optimized selection of input parameters, and, hence, the fabrication of components with improved thermo-mechanical properties. In this study the commercial FEM code SYSWELD® is used to predict the thermal histories and residual stresses generated in LENS™-produced thin plates of AISI 410 stainless steel built by varying the process parameters laser power and stage translation speed. The computational results are compared with experimental measurements for validation, and a parametric study is performed to determine how the thermo-mechanical properties vary with these parameters. Thermal calculations are also performed with the code ABAQUS® to evaluate its potential use as a modeling tool for the LENS™ process.

ACKNOWLEDGEMENTS

The author expresses his sincere gratitude for the assistance and guidance received through the course of this research. I would like to thank Dr. Sergio Felicelli for offering me a graduate research assistant position at Mississippi State University and for his guidance during this study. I would also like to thank Dr. Liang Wang for his invaluable assistance, as well as David Baker and Kiran Solanki for their technical support. I would also like to thank Dr. John Berry who gave much needed advice and direction, as well Dr. Camden Hubbard of Oak Ridge National Laboratory for his assistance with neutron diffraction measurement. Additionally, I want to thank the Center for Advanced Vehicular Systems and my team leader, Dr. Paul Wang, for the resources and opportunities provided to me.

TABLE OF CONTENTS

CHAPTER

LIST OF TABLES

LIST OF FIGURES

NOMENCLATURE

$\frac{dy}{dt}$	Translation velocity of stage
P_L	Laser power
T	Temperature
$\frac{dT}{dt}$	Heating/cooling rate
$\frac{dT}{dy}$	Translation velocity of stage
T_o	Initial temperature
T_a	Ambient temperature
T_l	Liquidus temperature
T_s	Solidus temperature
h	Convective heat transfer coefficient
ε	Surface emissivity
σ	Stefan-Boltzmann constant (5.67e-08 W/m^2K^4)
k	Thermal conductivity
c_p	Specific heat
A0	Power intensity
Δt	Idle time
H	Height

$\boldsymbol{d_{hkl}}$	Spacing between crystalline lattice planes
λ	Neutron wavelength
2θ	Diffraction angle
h, k, l	Miller indices
$\vec{\boldsymbol{Q}}$	Diffraction vector
$\vec{\boldsymbol{q}}_{incident}$	Vector of travel of incident neutrons
$\vec{\boldsymbol{q}}_{diffracted}$	Vector of travel of diffracted neutrons
$\boldsymbol{\varepsilon_{hkl}}$	Strain in lattice planes with orientation, *hkl*
$\bar{\boldsymbol{d}}_o$	Average reference lattice spacing for X,Y, and Z directions
$\boldsymbol{\sigma}_{\mathrm{hkl}}$	Stress accompanying lattice strain, $\boldsymbol{\varepsilon_{hkl}}$
E_{hkl}	Modulus of elasticity in direction normal to *hkl* plane
σ_Z	Component of residual stress in Z-direction
σ_Y	Component of residual stress in Y-direction
σ_X	Component of residual stress in X-direction
L_{ij}	Latent heat of transformation from phase *i* to *j*
A_{ij}	Fraction of phase *i* transformed to *j* per unit time
$Q_r(X,Y,Z)$	Distributed input energy density
Q_o	Magnitude of energy input density
r_e	Initial radius of laser beam
r_i	Reduced radius of laser beam

z_e	Upper plane on which initial radius located
z_i	Lower plane on which reduced radius located
f_i	Volume fraction of of phase *i*
$f_{austenite}$	Volume fraction of austenite
f_{M_i}	Fraction of martensite after thermal cycle *i*
f_{M_o}	Fraction of tempered martensite
f_{A_i}	Fraction of retained austenite after thermal cycle *i*
f_{A_o}	Fraction of retained austenite from previous thermal cycle *o*
M_s	Martensite start temperature
T_i	Lowest temperature reached in thermal cycle *i*\
E^{Total}	Total strain
E^E	Elastic strain
E^P	Total plastic strain
E^{CP}	Classical macroscopic plastic strain
E^{Thm}	Thermo-metallurgical strain
E^{TRIP}	Transformation-induced-plasticity (TRIP) strain
$\sigma_y^i(T)$	Temperature-dependent yield strength of phase *i*
$F(f)$	Empirical phase-dependent function
σ_{eq}	Effective stress
S_{ij}	Deviatoric stress

$\Delta E_{A\rightarrow M}^{Thm}$	Difference in thermal strain between two phases considered
$\boldsymbol{\sigma}_{y}^{A}$	Yield strength of austenite (or softer phase in arbitrary case
$h\left(\frac{\boldsymbol{\sigma}_{eq}}{\boldsymbol{\sigma}_{y}}\right)$	Nonlinearity function applied if $\sigma_{eq} \geq 0.5\sigma_y$
$\bar{\boldsymbol{\rho}}(T)$	Average temperature-dependent density
$\bar{c}_p(T)$	Average temperature-dependent specific heat
$\bar{k}(T)$	Average temperature-dependent thermal conductivity
$\bar{L}(T)$	Average temperature-dependent latent heat of melting
dt	Length of time step
L_e	Length of element set in direction of laser travel

CHAPTER 1

INTRODUCTION AND LITERATURE REVIEW

1.1 Introduction

Laser Engineered Net Shaping (LENS™) is a rapid manufacturing technology developed by Sandia National Laboratories (SNL) that combines features of powder injection and laser welding toward component fabrication. Several aspects of LENS™ are similar to those of single-step laser cladding. However, whereas laser cladding is primarily used to bond metallic coatings to the surfaces of parts that have already been produced with traditional methods [1], LENS™ involves the complete fabrication of three-dimensional, solid metallic components through layer by layer deposition of melted powder metal.

In this process, a laser beam is directed onto the surface of a metallic substrate to create a molten pool. Powder metal is then propelled by an inert gas, such as argon or nitrogen through converging nozzles into the molten pool. Depending upon the alignment of the nozzle focal point with respect to that of laser, then powder is then melted either mid-stream or as it enters the pool. As the laser source moves away, the molten material then quickly cools by conduction through the substrate, leaving a solidified deposit.

The substrate is located on a 3 or 5-axis stage capable of translating in the X and Y-directions. Initially, a 3-D CAD model is created to represent the geometry of a desired component. The CAD model is then converted to a faceted geometry composed of multiple slices used to direct the movement of the X-Y stage where each slice represents a single layer of deposition. During the build, the powder-nozzle/laser/stage system first traces a 2-D outline of the cross section represented by each slice I the X-Y plane and then proceeds to fill this area with an operator-specified rastering pattern. The laser/nozzle assembly then ascends in the Z-direction so that the next layer can be added. This process is repeated for consecutive layers, until completion of the 3-D component [2]. This feature is illustrated schematically in Figure 1.

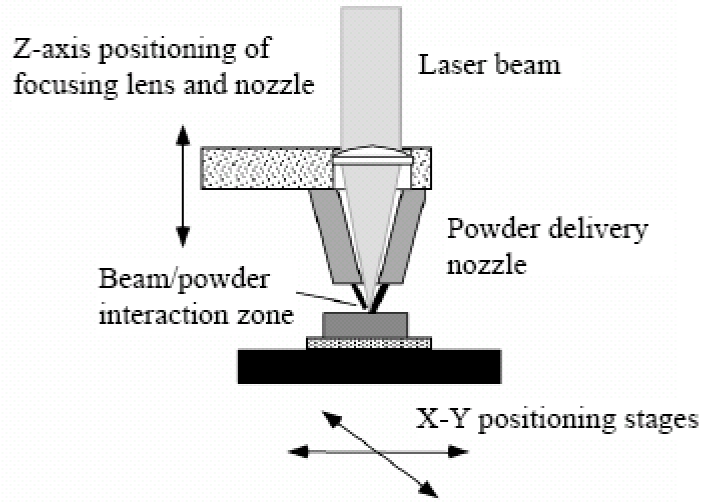

Figure 1. Schematic of LENSTM deposition process.

The ability of LENS™ to manufacture products at near net shape has the potential to revolutionize the production of small-lot metallic products by decreasing the time and cost associated with post-process machining. LENS™ can also be implemented to perform repair operations in situations that would otherwise require fabrication of replacement parts [3]. Furthermore, in a study conducted by Griffith *et al*. [4] into the mechanical properties of LENS-deposited™ AISI 316, the researchers recorded a 100% increase in yield strength over that of the wrought alloy. Griffith *et al.* [4] theorized that the improved mechanical performance was derived from a very fine grain structure measured in the deposited material as a result of the extremely high cooling rates observed during LENS™ deposition.

A thorough understanding of the thermo-mechanical characteristics inherent with the LENS™ process could lead to increased quality in LENS™-fabricated products by a better selection of LENS™ process parameters, thus leading to a wider acceptance of this technique in the manufacturing industry. The LENS™ process exhibits complex thermo-mechanical-metallurgical behavior as it involves the laser-induced melting, solidification, and re-melting of successive layers of powder metal by a moving heat source, i.e. the laser, in the presence of a large heat sink, i.e. the substrate, as well as other sources of heat loss, such as that due to convection and radiation. The thermal history generated during the building of part determines the metallurgical phases present within the finished product and, hence, its mechanical properties. Thermal strains, metallurgical transformations, and phase interactions that occur during the process induce residual stresses that limit the service loads that may be applied to LENS™ products in the field. Large thermal strains can also lead to geometric distortions that take part dimensions out of tolerance. The thermo-mechanical-metallurgical properties are heavily dependent upon the process parameters, i.e. the heat input from the laser, the translation speed of the X-Y stage, the flow rate of metal powder, and various others. Accordingly, it is important that computational tools are developed to effectively predict the thermo-mechanical-metallurgical properties of LENS™ parts for any particular combination of process parameters.

The goals of this study were the generation of a process map for optimal selection of the parameters laser power and stage speed to limit residual stresses and the development of computational tools to accurately predict the magnitudes and distributions of residual stresses in LENS^{TM}-produced components. The development of a process map involved analyzing experimental measurements of residual stresses in seven thin plates of AISI 410 stainless steel produced by LENS^{TM} with different values of laser power and translation speed. The measurements were collected using the neutron diffraction method. The advancement of a computational tool involved the use of a coupled thermo-mechanical-metallurgical model to simulate the various physical aspects of the plate depositions for similar process conditions. The modeling calculations were performed with the finite element method (FEM), using the welding analysis software SYSWELD® and the general purpose finite element (FE) package, ABAQUS®. For verification of accuracy, the numerically predicted residual stresses were then compared to the measured values, while several calculated thermal characteristics were compared to corresponding experimental values measured during the depositions of the plates. The next section presents a comprehensive literature review of previous efforts to relate process parameters to the thermo-metallurgical characteristics of LENS^{TM} components, as well as studies involving the measurement of residual stresses in LENS^{TM} deposits. Additionally, previous efforts to computationally model the process are examined.

For subsequent descriptions of the LENS^{TM} deposition of thin plates and the related process parameters, the coordinate system shown in Figure 2 will be adopted.

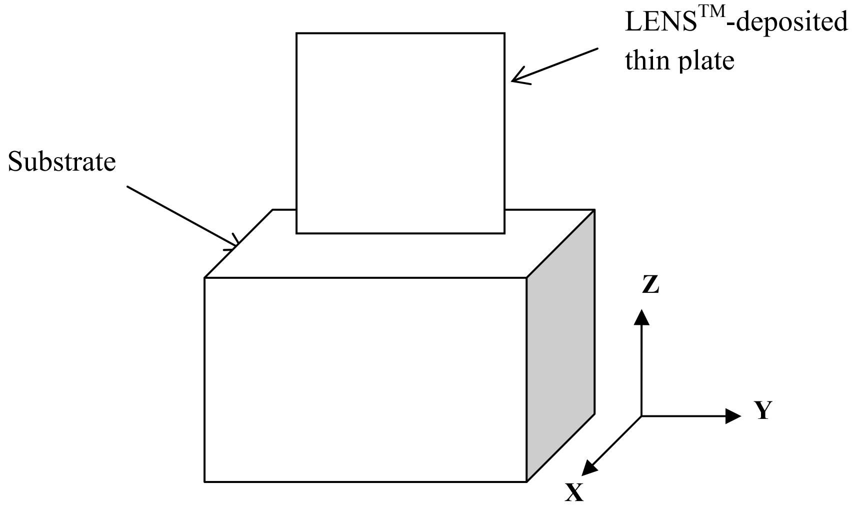

Figure 2. Coordinate system applied to LENS™ thin plates.

For the arrangement shown in the figure, "height" refers to Z-directional plate dimension, while "width" and "depth" refer to Y-directional and X-directional plate dimensions, respectively.

1.2 Literature Review

1.2.1 Experimentally Measured Effects of Process Parameters in LENS™

Keicher *et al.* [5] evaluated the effects of process parameters on multi-layer deposition of laser-melted powder Inconel® 625 in a process similar to both laser cladding and LENS™. The group initially examined various parameters, including laser irradiance, stage translation speed, powder flow rate, powder particle size, and the size of each Z-directional increment between layers and their effect on heat affected zone (HAZ) size generated during the build. The HAZ was defined in this study as the melted region below the surface of the substrate and was examined post-build via metallographic analysis. The group conducted a substantial number of tests with three variations of six process parameters. Their initial findings clearly indicated that the dominant parameters were stage speed ($\frac{dy}{dt}$) and laser irradiance, defined as the power per unit area directed onto a surface by the laser. The tests were performed at laser irradiances of 345, 549, and 774 W/mm^2 and $\frac{dy}{dt} = 8.47, 21.17$, and 33.9 mm/s.

The results showed a slight increase in the depth of the HAZ with decreasing $\frac{dy}{dt}$ for each level of irradiance with an approximately 0.05 mm difference between the maximum and minimum speeds for all irradiances. A larger increase was seen with increasing irradiance and constant speed, with an approximately 0.1mm difference recorded between the high and low irradiances for any $\frac{dy}{dt}$. The researchers also observed a critical input laser power of approximately 220 W after which little no growth in HAZ occurred.

Hofmeister *et al.* [6,7] performed in situ experimental measurements of the temperature distributions in LENS™ thin plates of AISI 316 stainless steel produced with a range of laser powers (P_L) and translation speeds during two studies at SNL. The purpose of the studies was to calculate the 1-D temperature gradients ($\frac{dT}{dy}$) and cooling rates ($\frac{dT}{dt}$) in the direction of stage travel (*y*) from the observed temperature profiles as $f(P_L, \frac{dy}{dt})$. Thermal imaging was performed with two high-speed CCD cameras. Sample plates of AISI 316 were produced at laser powers of 212 W, 365 W, and 410 W and translation speeds of 5.93 mm/s, 7.62 mm/s, and 9.31 mm/s.

After analyzing the thermal images, the group plotted isotherm lines over the sample plates to observe the distributions of temperatures. In this study, the molten pool created by the laser was defined as the region with temperature at or above the liquidus of AISI 316 ($T \geq 1673$K). The group measured 1-D temperature gradients in the direction of stage travel and calculated the accompanying cooling rates by multiplying the gradient by the stage speed ($\frac{dT}{dt} = \frac{dy}{dt} * \frac{dT}{dy}$) . The researchers found that the highest cooling rates occurred between the solidus and liquidus isotherms (1645 K < T < 1673 K) and dropped off slightly at and below the liquidus.

The results showed that the thermal characteristics of a particular build were strongly dependent on P_L and $\frac{dy}{dt}$. Generally, Hofmeister *et al.* [6,7] found higher cooling rates (approximately -1000 K/s) between the solidus and liquidus and smaller molten pool lengths in the Y-direction in cases of low P_L, and high $\frac{dy}{dt}$. Conversely, lower cooling rates (approximately -100 K/s) and larger molten pool lengths were calculated in cases of high P_L, low $\frac{dy}{dt}$. The group identified a relationship whereby the cooling rate is inversely proportional to the square root of the molten pool length. Hofmeister *et al.* [6,7] concluded that the second case of parameters, which involved higher heat input, longer heating time, and longer heat sink conduction path, resulted in greater bulk heating of the sample plates and, thus, shallower temperature gradients at the solid/liquid interface. Figure 3 is a plot of the recorded temperature as a function of distance from the molten pool center for various laser powers.

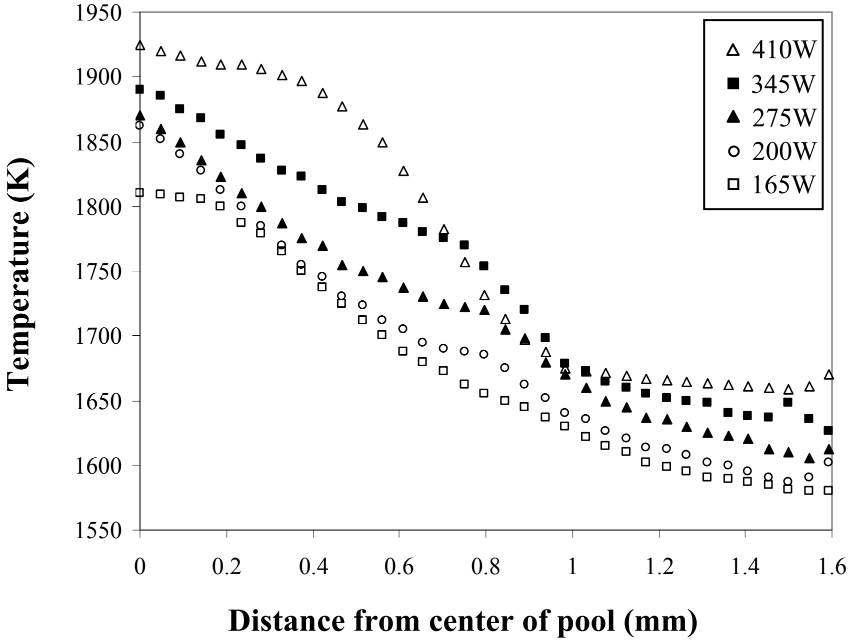

Figure 3. Temperature distribution in top layer of AISI 316 plate as measured by Hofmeister *et al.* for various laser powers from Reference [6].

Though the molten pool size showed sensitivity to the applied laser power, the dimensions remained relatively constant above the value of P_L = 275 W. Keicher *et al.* [5] reported a similar effect whereby the HAZ grew little above P_L = 220 W.

A subsequent parametric study by Hofmeister *et al.* [8] using the same set of process parameters yielded the results shown in Figure 4.

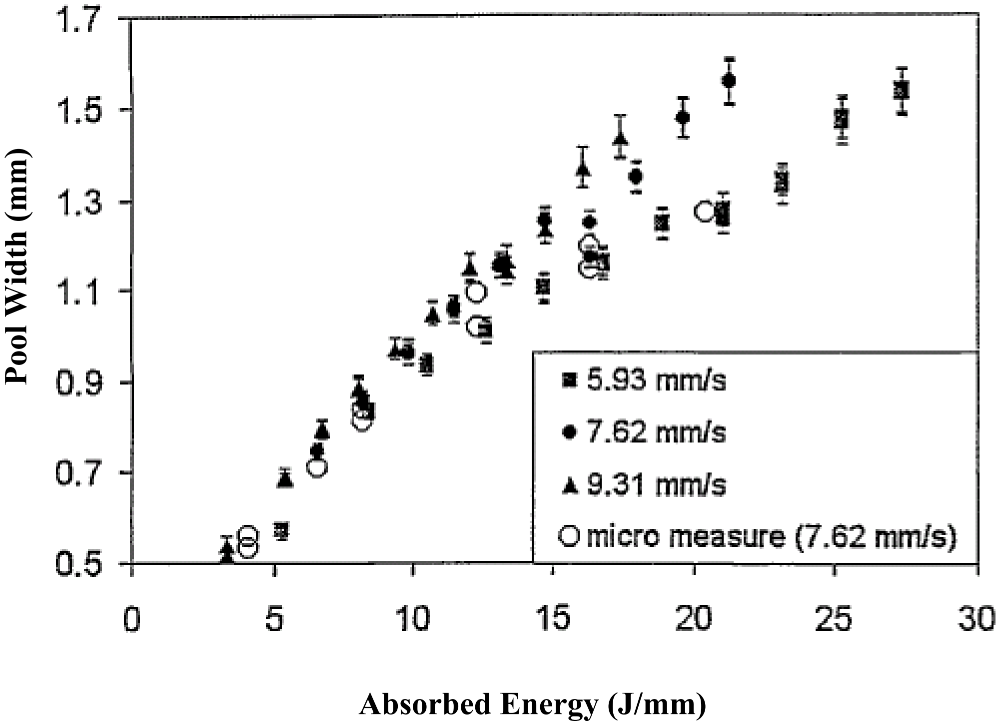

Figure 4. Depth of melt pool (mm) in Z-direction for different values of stage speed (mm/s) and absorbed energy (J/mm) from Reference [8]

The pool width in Figure 4 is the depth of the molten pool in the Z-direction, while the absorbed energy is the product of laser power (P_L) and absorptivity (= 0.35) divided by the stage speed ($\frac{dy}{dt}$) and the pool width. These results closely match the relationship of HAZ and speed and heat input to HAZ observed by Keicher *et al.* [5] for their laser deposition process.

Yet another study conducted by Smugeresky *et al.* [9] examined the effects of process parameters on the measured hardness in thin plates of AISI 316. Using input laser powers of P_L = 150, 300, and 600 W and $\frac{dy}{dt}$ = 4.2, 8.5, and 16.9 mm/s, the group reported a tendency toward higher measured hardness with increasing stage speed for some input power. Also, the hardness appeared to increase with reduction in P_L at some $\frac{dy}{dt}$.

Khalen and Kar [10] performed an investigation into the effects of a several parameters on the resulting yield strength of AISI 304 stainless steel thin plates in process identical to LENS^{TM} termed laser-aided direct rapid manufacturing (LADRM). This team sought to generate a range of input parameter values within which components with acceptable mechanical properties could be deposited. Their approach involved using the Buckingham Π-Theorem to express the process variables associated with heat transfer and powder mass flux in terms of 14 dimensionless parameters. Laser power and stage translation speed were two variables under consideration with experiments values of P_L=300, 400 W and $\frac{dy}{dt}$ = 5.1, 7.6, 10.2, 12.7, and 15.2 mm/s examined. The team recorded temperature profiles during the builds using a pyrometry system and found larger melt pool sizes and lower cooling rates for P_L = 400 W. Additionally, mechanical testing of the plates after deposition revealed higher yield strengths for cases of P_L = 400 W. These results at first seem contradictory, since the higher cooling rates observed for cases of P_L = 300 W would form finer grained microstructures that should provide strengthening. However, Khalen and Kar [10] theorized that the larger molten pools created at higher laser power serve to relieve residual stresses in the previously deposited layer.

1.2.2 Measurement of Residual Stresses in LENS^{TM}

Rangaswamy *et al.* [11,12] sought to experimentally measure residual stresses in LENS^{TM} deposits using the neutron diffraction method, the details of which are discussed in Section 2.2.2. The measurements were performed on LENS™-produced rectangular plates of AISI 316. The neutron data was collected at several points methodically distributed within the geometry of the samples, as shown in Figure 5, to provide a map of the stress distribution. At these locations the cross-section of entering and exiting neutron beams created 2.0 mm^3 gauge volumes within which elastic strains were measured.

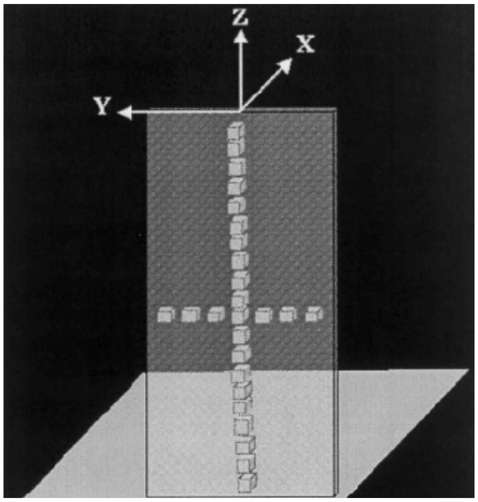

Figure 5. Distribution of gauge volumes for neutron diffraction measurement of residual stress within LENS™ thin plate of AISI 316 from Reference [11].

Rangaswamy *et al.* [11] then calculated the axial components of residual stress through Hooke's law. Each stress component was then plotted against position within the plate, first, along the height (Z-direction) on the sample vertical centerline, and next, along the width (Y-direction) on the plate horizontal centerline. These plots are shown in Figure 6.

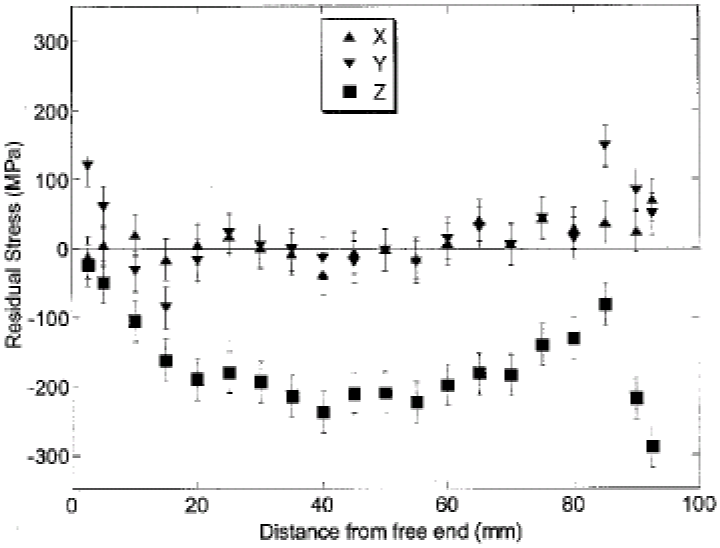

(a)

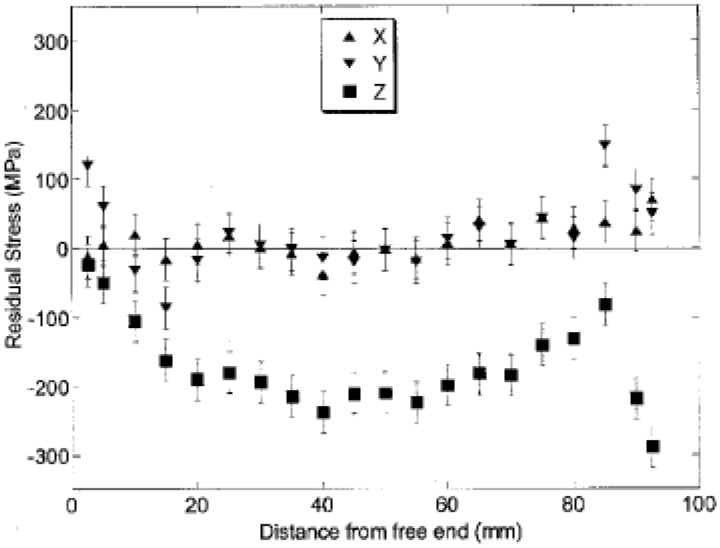

(b)

Figure 6. Axial stress components along centerlines of AISI 316 thin plate in (a) Z-direction and (b) Y-direction from Reference [11].

The results show that the Z-component of stress dominates the stress state within the plate, which is largely compressive close to the center of the sample. Along the vertical centerline, the Z-component of stress decreases significantly near the top surface of the plate, while the Y-component is non-zero at this location. At the other end, closer to the substrate, the Z-component sharply increases, while the other two components are non-zero. Rangaswamy *et al*. [11] attribute the complex stress state at this location to reaction forces from the substrate and martensitic transformation in the lower deposited layers. Along the horizontal centerline, the Z-component stresses are compressive near the center and tensile near the edges. The other two stress components are compressive on one side of the centerline and tensile on the other. All stress components appear, though, to balance to an equilibrated state.

In a previous study, Rangaswamy *et al.* [11] had experimentally determined the yield strength of LENS™-produced AISI 316 specimens through monotonic tension testing as 441 MPa. Accordingly, the maximum measured compressive stress within the thin plate, approximately 215 MPa, represented nearly half the yield of the material. These measurements show that the residual stress imparted to thin plates during the LENS™ are substantial and, without the added step of heat treating, would seriously affect the performance of LENS™ components in the field.

1.2.3 Computational Modeling of the LENS^{TM} Process

1.2.3.1 Thermal Analyses

Hofmeister *et al.* [6] offered some limited finite element calculations in to model the deposition of a single-pass AISI 316 thin plate. The group modeled the laser melting as a moving boundary problem for which the solid/liquid interface follows the moving heat source across the surface being deposited. The boundary problem was solved using a computationally expensive method that involved the storage of all calculated data at the end of each time increment followed by the updating of all boundary conditions at the beginning of the subsequent increment [13]. The deposition of new material was simulated with an "element birthing" technique, in which new elements were introduced into the domain at a specified initial temperature. This method has also been termed "element activation" and has been previously used to model multi-pass welding [14].

The domain represented a plate 25.4 mm wide and 76.2 mm tall composed of layers one element in thickness. Each new element was introduced into the domain at an initial temperature of $T = 1377$ °C (AISI 316 melting point) or $T = 1627$ °C (case of superheating) to represent the laser heat source. The only heat transfer mode considered was conduction through the substrate. The elements were assigned thermal material properties for a generalized stainless steel. The results showed a steep temperature gradient near the molten pool which levels to a steady state condition further from the pool. These results are in agreement with measured data, such as that shown in Figure 3. However, a detailed parametric investigation was not undertaken.

Riqinq *et al.* [14] also developed a 3-D model for simulating LENS^{TM} deposition of an AISI 316 thin plate. Their approach was similar to that of Hofmeister *et al.* [6], except that the moving solid/liquid interface was reduced to a fixed boundary problem using an immobilization transformation. The material deposition was accounted for by a similar element activation method and the laser heat source was represented by setting the initial temperature of each new element equal to the melting temperature of AISI 316. As in Reference [6], only conduction heat transfer was considered to occur.

The computational domain was 11mm wide, 6.5 mm tall, and 0.25 mm thick and composed of 8-node cubic 0.5 mm x 0.25 mm x 0.13 mm elements. Each newly activated element was held at the melting temperature for the length of time needed to simulate a 5mm/s stage translation speed. Temperature-independent thermal properties of AISI 316 were applied to the domain. The computed temperature profiles were compared to experimental values measured with a two-wavelength pyrometry system for an AISI 316 thin plate produced with $\frac{\mathrm{dy}}{\mathrm{dt}} = 5$ mm/s and $P_L = 240$ W. The calculated and measured temperature profiles showed good agreement with both indicating a sharp temperature gradient near the solid/liquid interface that dramatically decreased with distance.

An in-depth study was conducted by Wang and Felicelli [15] who sought to quantify the effects of varying input parameters and modes of heat transfer in the LENS™ deposition of a 2-D thin plate of AISI 316 using MULTIA, a research code generally used to model solidification in castings. For simplicity, only melting of the final layer was simulated, while the lower layers were assigned a uniform initial temperature obtained from the Hofmeister measurements [6]. The addition of new elements to the domain was not modeled, but instead the whole top layer was present throughout the build. The location of the solid/liquid interface was solved in the same manner as in Reference [6].

Rather than model the heat source as an initial temperature condition, Wang and Felicelli [15] applied a Gaussian-distributed heat flux load to the top of the plate. They also applied boundary conditions along top and vertical plate edges to account for losses due to convection to the chamber atmosphere and radiation emitted from the part. The latent heat of melting was also included in the governing equation.

In order to validate the accuracy of the model, Wang and Felicelli [15] compared their calculated results to the findings of Hofmeister and *et al.* [6] for $\frac{dy}{dt} = 7.62$ mm/s and $P_L = 275$ W by simulating the LENS™ deposition of a 10 mm tall, 25 mm long plate of AISI 316 using input values $\frac{dy}{dt} = 8$ mm/s and power intensity of 1.36e06 K/m, which approximately corresponds to $P_L = 275$ W. The mesh was composed of 100,000 bilinear square elements $5.0e^{-2}$ mm on a side, to which published thermal material properties of AISI 316 were assigned. The researchers selected a convective heat transfer coefficient, $h = 100$ W/m^{2}K, and emissivity, $\varepsilon = 0.62$, to describe the heat losses due to convection and radiation, respectively. To validate the numerical results, Wang and Felicelli [15] plotted the simulated temperature as a function of distance from the center of the molten pool and superimposed the experimental plot shown in Figure 2 for $P_L = 275$ W over his calculated values. The combined plot, shown in Figure 7, demonstrates good agreement between the numerical and measured temperature profiles.

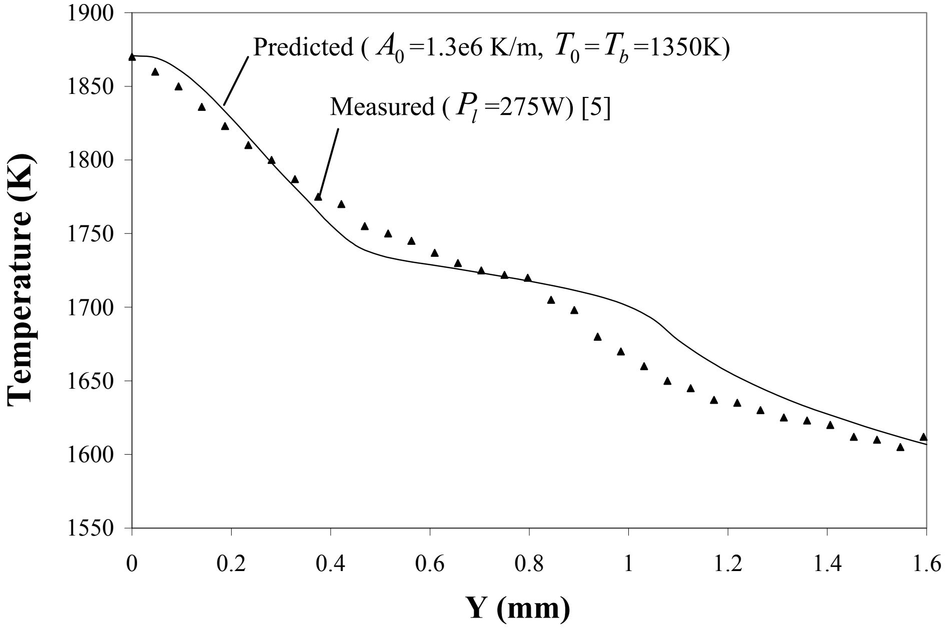

Figure 7. Numerical and experimental temperature measured from center of molten pool in top layer of LENS™ AISI 316 deposit with P_L=275W from Reference [15].

Wang and Felicelli [15] next performed a parametric study similar to that done by Hofmeister *et al.* [8] to determine if the same trends in cooling rates and thermal gradients were observable for different laser power. He repeated the previous simulation using five power intensity values, revealing that the temperature gradient at the edge of the molten pool increases substantially with laser power, while the cooling rate decreases. The resulting plots are shown in Figure 8 where A0 indicates power intensity.

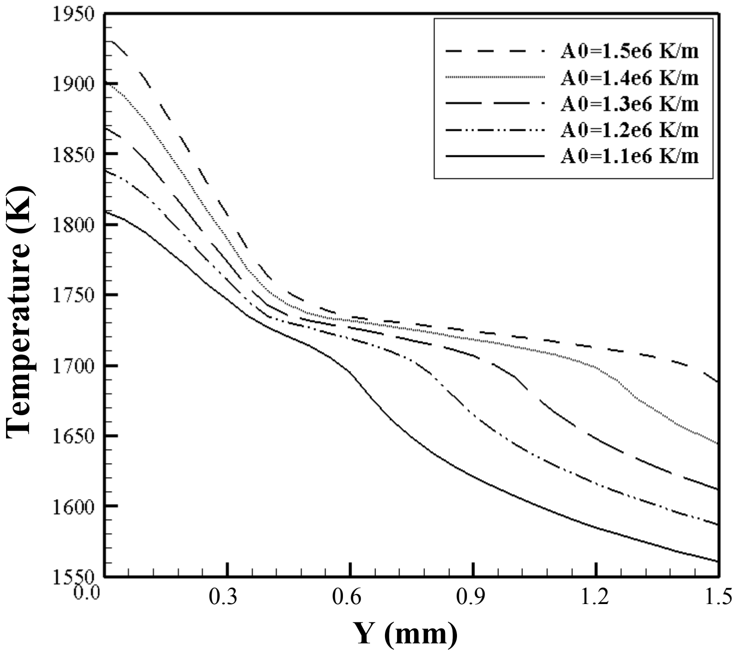

Figure 8. Temperature measured from center of molten pool in top layer for various laser powers from Reference [15].

These same trends were recorded in the experimental study, suggesting that the model could accurately predict the thermal behavior of LENS™.

A similar study was conducted by Neela and De [16] to study the effects of translation speed and laser power on the resulting temperature profiles using the general purpose FE package, ABAQUS® 6.6. The researchers used an element activation/deactivation similar to those previously seen in References [6] and [14] to model the deposition of a thin plate of AISI 316 with temperature-dependent thermal conductivity and specific heat according to a liner, and quadratic relation, respectively. As in Reference [15], the heat source was described by a Gaussian-distributed heat flux, which was applied to the domain through the ABAQUS® subroutine DFLUX. Neela and De [16] simulated the building of a 15 mm wide, 6.25 mm tall, 1 mm thick plate discretized into a mesh of 25200 8-node, C3D8T heat transfer elements. The process parameters considered were P_L = 165, 200, 275, 345, and 410 W and $\frac{dy}{dt}$ = 5-10 mm/s. Their calculated temperature profiles for an active layer are shown in Figure 9.

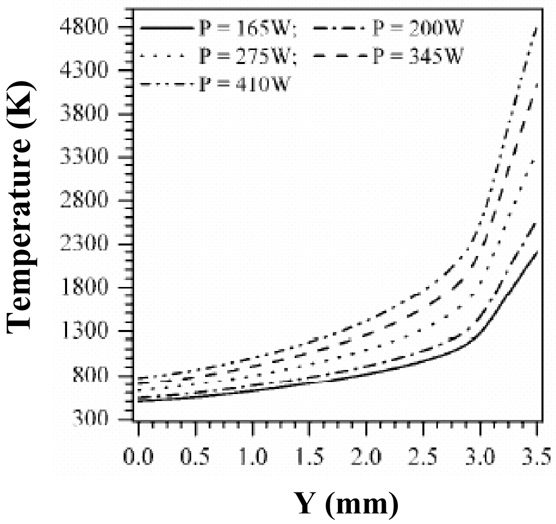

(a)

Figure 9. Temperature in direction opposite to laser travel for (a) variable laser power and (b) variable stage speed from Reference [16].

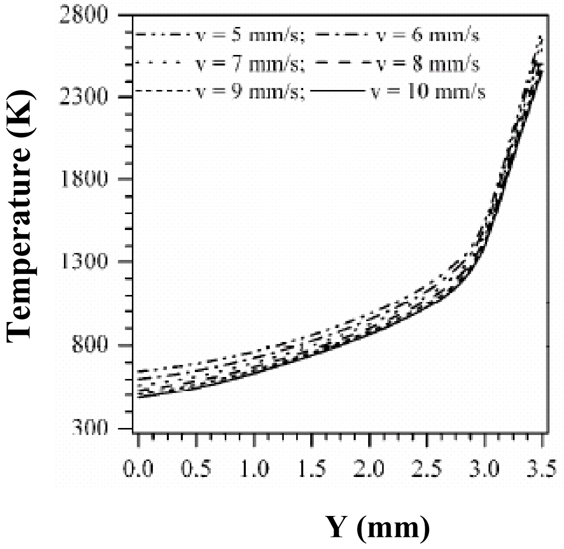

(b)

Figure 9 (Continued).

The predicted trend in Figure 9(a) for increasing P_L matches that calculated by Felicelli and Wang [15], and the relations in both 9 (a) and 9 (b) are supported by the experimental molten pool data recorded by Hofmeister *et al*. [8]. The authors noted that any calculated temperatures greater than 2800 K were not realistic, since the material would boil above this temperature.

1.2.3.2 Coupled Analyses

Several efforts have been made to relate resultant mechanical properties to the thermal histories generated during LENS™, as well as in various other laser deposition processes. Deus and Mazumder [17] attempted to predict the residual stresses resulting from a laser cladding deposition of C95600 copper alloy onto an AA333 aluminum alloy substrate. Since residual stresses would be generated by the heterogeneous thermal expansions of the deposited and substrate materials, accurate stress calculations would also require accurate prediction of the temperature fields created during the build. Accordingly, Deus and Mazumder [17] developed a 2-D thermo-mechanical model using the finite element package ABAQUS 5.4. The model implementation did not employ a direct coupling of thermal and mechanical processes, but rather used the calculated temperature fields as input for the mechanical constitutive model in a weak-coupling scheme. As in References [15] and [16], the laser source was described by a Gaussian-distributed heat flux and material deposition was simulated with an element activation technique.

The constitutive model used was a simplified temperature-dependent, elastic-perfectly plastic type, meaning that any strengthening beyond yield the point, which was determined by a Von Mises criterion, was not considered for either material. Though Deus and Mazumder [17] recognized the many simplifications used to define the model, they argued that the calculated results would be qualitatively accurate.

The researchers performed a series of purely heat transfer simulations to determine a combination of laser power and travel speed that would result in an acceptable laser clad, i.e. the molten pool extending to the deposit/substrate interface, but not below it. This condition was achieved with an absorbed laser power of 210 W and a translation speed of 12.5 mm/s. The resulting stress-strain calculations showed that plastic strain was generated during the deposition, but that it was restricted to areas where melting had taken place. Residual stresses in the Z-direction were measured with those above the deposit/substrate interface having tensile values and those below, compressive.

Another thermo-mechanical study was performed by Labudovic *et al.* [18] to predict residual stresses in a process identical to LENS^{TM} termed the direct laser metal powder deposition process. A 3-D coupled model was implemented through the FE package ANSYS® for the deposition of a 50 mm x 20 mm x 10 mm thin plate of MONEL 400 onto a substrate of AISI 1006. The deposition was modeled with an ANSYS® element activation option similar to those already presented. Energy input density was modeled as a moving Gaussian distribution through the ANSYS® Parametric Design Language subroutine. The constitutive model was a temperature-dependent visco-plastic model, in which viscous effects were neglected by ignoring it the associated term in the equation of state. As in Reference [17], a weak coupling formulation was used by ANSYS® to approximate the coupled solution.

In order to qualify the thermal calculations, a parametric study was performed to compare computational and experimental molten pool sizes for various combinations of input variables. The process parameters used were P_L = 400, 600, and 800 W and $\frac{\mathrm{dy}}{\mathrm{dt}}$ = 5, 10, and 15 mm/s. Experimental measurements were taken using a high shutter speed camera to capture molten pool size. Additionally, the thermal model was solved analytically for temperature isotherms and compared to both computed and observed results. These comparisons are shown in Figure 10.

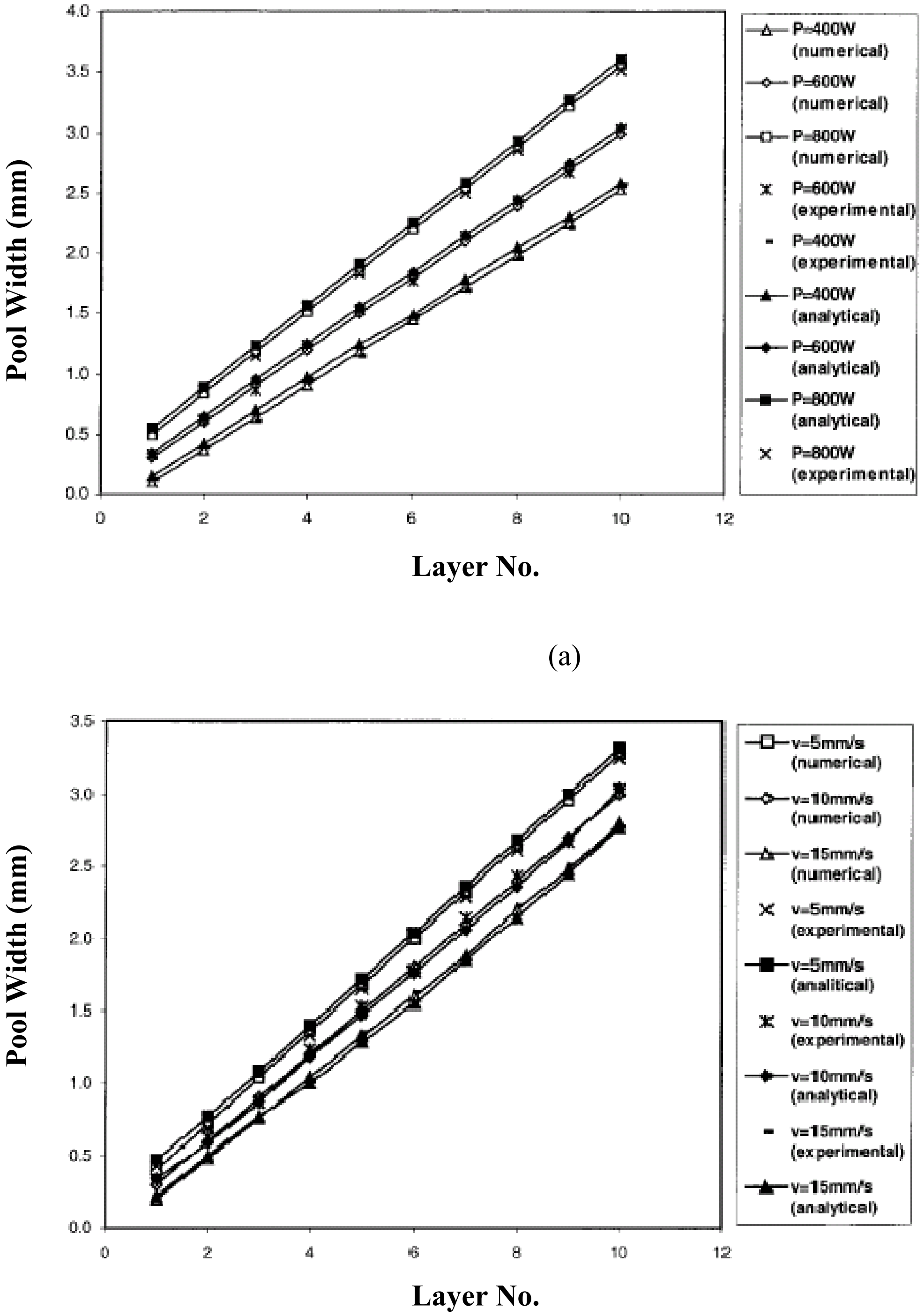

(a)

(b)

Figure 10. Variation in molten pool size for various laser powers and translation speed from Reference [18].

Excellent agreement is obtained amongst all three solutions. The relationships between molten pool size and the input parameters are similar to those already presented in Figures 8, 9, and 4 from Reference [15], [16] and [8], respectively.

Having validated the thermal calculations, Labudovic *et al.* [18] proceeded with the calculation of residual stresses for the case of P_L=600 W and $\frac{dy}{dt}$=10 mm/s. The modeling results were compared to experimental values obtained with X-ray diffraction for validation, and are shown here as Figure 11.

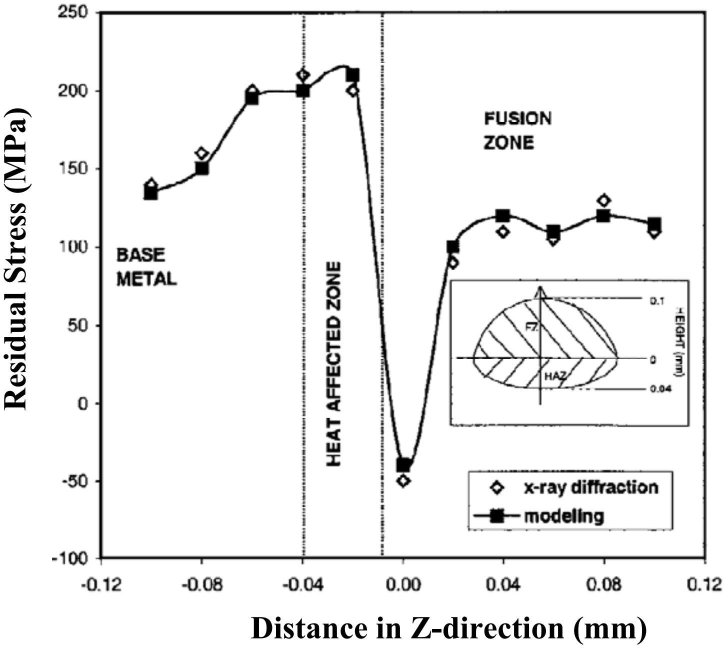

Figure 11. Distribution of residual stress in deposit/substrate interfacial region of MONEL 400 thin plate from Reference [18].

As with the thermal calculations, the predicted stresses closely match the experimental values. The weakly coupled thermo-mechanical analysis is capable of accurately approximating the induced stresses.

Several authors have also attempted to capture the relationship between thermal and metallurgical processes in laser powder metal deposition, since the resulting microstructure significantly influences the mechanical properties of the finished part. Costa *et al.* [19] performed a series of computational tests to determine the effect on substrate size and idle time (time between depositions of consecutive layers) on the resulting thermal histories and subsequent microstructural transformations in laser powder deposition of thin plates of AISI 420 stainless steel. The goal of the study was to predict the final distributions of austenite and martensite phases in the plates considering different substrate masses and idle times.

The group employed a direct coupling formulation for their thermo-metallurgical model whereby calculated temperature fields were used as input for a semi-empirical Koïstinen-Marbürger thermo-kinetic model to calculate the proportions of austenite, martensite, and tempered martensite phases. The calculated phase fractions were then used to update the thermal properties of the alloy, which were defined as temperature-dependent weighted averages of the constituent phases. These updated properties (specific heat, latent heat, thermal conductivity, density) were then used to calculate the temperature field for the subsequent time step, thereby enacting the direct coupling.

The calculations were performed in ABAQUS® for a 10 mm x 1 mm x 0.5 mm plate composed of ten deposited layers. As in previous studies, the ABAQUS® element activation procedure was used to model the deposition, whereby new elements entered the domain with an initial temperature equal to the liquidus of AISI 420. Additionally, the heat source was defined as a Gaussian-distributed energy input density. The cases studied all considered $P_L = 325$ W and $\frac{dy}{dt} = 10$ mm/s, while values of Δt, idle time, were 1, 2, 3, 4, 5, and 10 seconds. The substrate masses studied were 13.5 g and 102.8 g.

The thermal results showed a similar cooling effects for large Δt and large substrate, in which a deposited layer experienced a significant reduction in temperature prior to the deposition of the next layer. Conversely, small values of Δt or small substrate, inhibited cooling between layer depositions, and result in comparatively large molten pool depths that initiated re-melting in previously deposited layers.

The variation in temperature profiles had profound effects on the subsequent microstructural distributions. For cases of large Δt and/or large substrate, the heated regions reached sufficient temperatures to induce austenitic transformation, but then rapidly cooled below the martensite initiation temperature, transforming in a tempered martensite phase. This process occurred in previously deposited layers as well, causing successive generations of martensitic tempering in each layer and heterogeneous final microstructure. For cases of small Δt and/or small substrate, conduction through the substrate was insufficient to cool below the austenization temperature in the top six layers. Accordingly, these layers remained austenitic until all ten layers had been deposited, after which a uniform cooling to room temperature occurred that resulted in 1^{st} generation martensite microstructure in this region of the plate.

The distribution of hardness in the final part was directly dependent on the phases present and, accordingly, on the idle time and substrate dimensions used. This dependency is shown in Figure 12, which plots hardness values along the vertical plate centerline for different idle times and a large substrate.

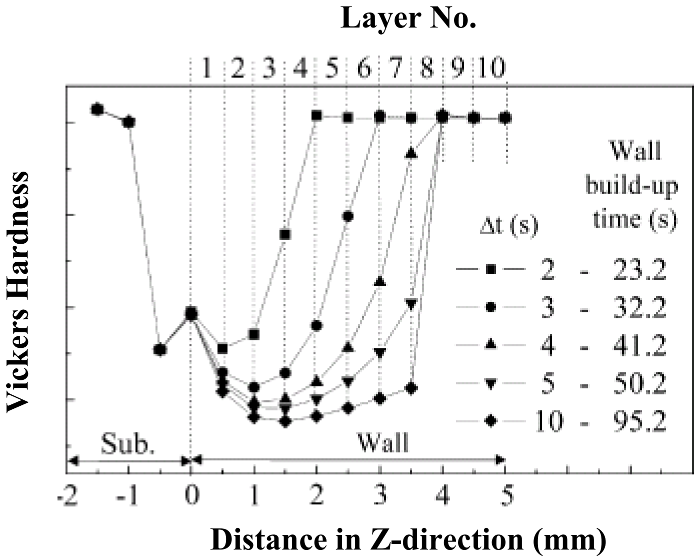

Figure 12. Distribution of hardness in AISI 420 plate as function of idle time, Δt from Reference [19].

Wang *et al.* [20] used a coupled thermo-metallurgical model to predict the temperature fields in LENS^{TM}-deposited thin plates of X20Cr13 for different values of P_L and $\frac{dy}{dt}$. The modeling results were compared to experimental temperature measurements taken via radiation pyrometry during LENS^{TM} fabrication of AISI 410 thin plates using the same process parameter values. The group showed the chemical composition of the two alloys to be nearly identical and thus valid for comparison. Computational modeling was performed with the FE software SYSWELD®, an analysis package designed to perform welding simulations. A coupling scheme similar to that seen in Reference [19] was used, as well as the same Koïstinen-Marbürger phase transformation model. The phases considered were retained austenite, martensite, and tempered martensite.

The computational domain represented a 10 mm x 1 mm x 0.5 mm thin plate composed of ten layers. The deposition was modeled with a “dummy element” method, in which whole layers were added to the domain at the beginning of the time step following the completion of the previous layer. Regions of the layer were activated in response to the location of the heat source through a change of thermal properties, whereby those elements forming layers yet to be deposited were given excessively low thermal property values that prevented them from interacting thermally with the deposited regions. For layers in the process of deposition, elements were assigned the values of X20Cr13 for some initial volume fraction of phases and allowed to heat up, but were switched to austenite($\mathrm{f}_{\mathrm{austenite}} = 1.0$) when the austenization temperature of X20Cr13 was reached. Once austenitized, the elements were considered to be in the ‘deposited’ condition and allowed to undergo phase transformation according to the kinetic model as they heated and cooled throughout the build process.

Ten experimental samples were deposited with combinations of input parameters, P_L = 300, 450, and 600 W and $\frac{\mathrm{dy}}{\mathrm{dt}}$ = 2.5, 4.2, and 8.5 mm/s. The sample plates each consisted of 25 single-pass layers. The widths of the plates (Y-direction) varied somewhat from sample to sample, yet were all within 22-38 mm. The height (Z-direction) remained constant at 15 mm, while the thicknesses ranged from 1 mm to 3 mm based upon input parameters – more powder melted at larger laser powers and lower translation speeds.

The corresponding simulations were performed with conical Gaussian-distributed input energy densities of 300, 450, or 600 W/mm^3 and assumed a distribution of 1.0mm^3. The moving heat source was modeled with a SYSWELD® subroutine using the same values as those in the experimental builds. The heat source moved in the same direction for each layer and was deactivated between consecutive layer depositions for a specified idle time, Δt, that depended on the velocity of the source. The computational domain was chosen to represent an actual plate 25 mm long, the length of several of the samples. Accordingly, the value of Δt was specified to account for the excluded 15mm of deposition. Wang *et al.* [20] proposed that this approximation was valid, since the large cooling rates measured by thermal pyrometry for the experimental samples indicate that the heating effects are highly localized. Their measured cooling rates are shown in Figure 13.

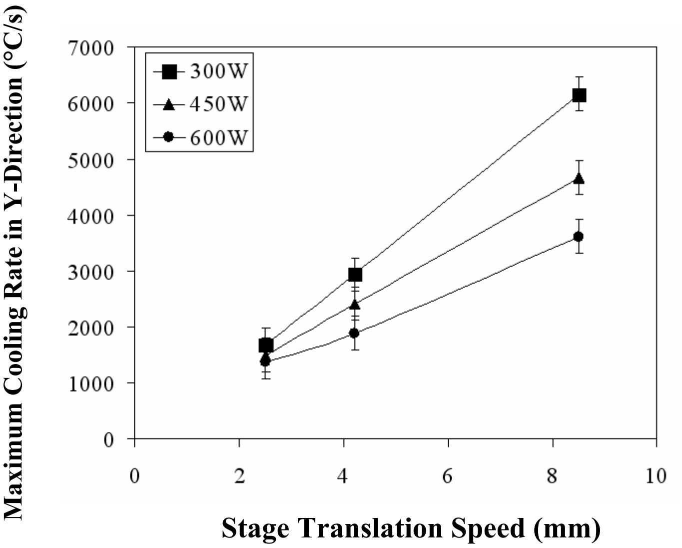

Figure 13. Maximum measured cooling rate along travel direction from Reference [20].

These extreme levels of cooling suggest that a newly deposited or, newly re-heated, region of the plate quickly returns to room temperature after moving away from the laser.

The calculated temperature along the direction opposite to that of the moving heat source is shown in Figure 14 with increasing distance from the center of the molten pool. The observed distribution in the corresponding experimental sample is also plotted for comparison.

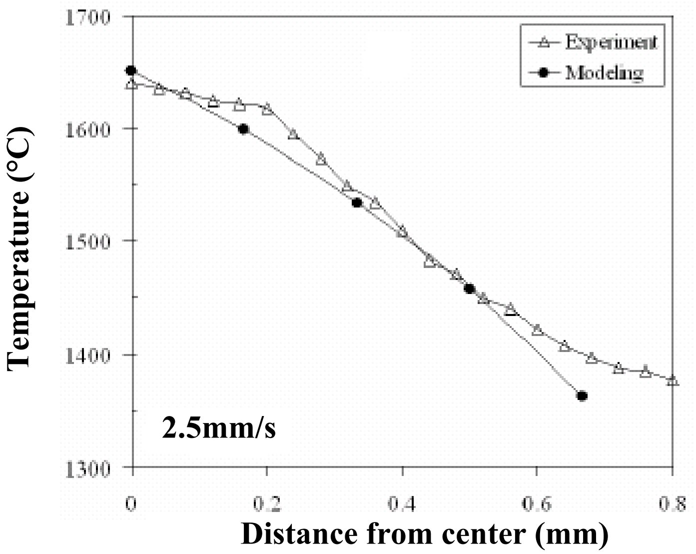

Figure 14. Calculated temperature along direction opposite to moving heat source for 600 W and 2.5 mm/s and corresponding measurements for Sample 4 from Reference [20].

As shown in Figure 14, the calculated temperature distribution closely matched the measured values in the direction opposite to the relative travel of the laser. Similarly, the same temperature change with distance from the center of the molten pool in the Z-direction, i.e. with increasing depth, is shown for both results in Figure 15.

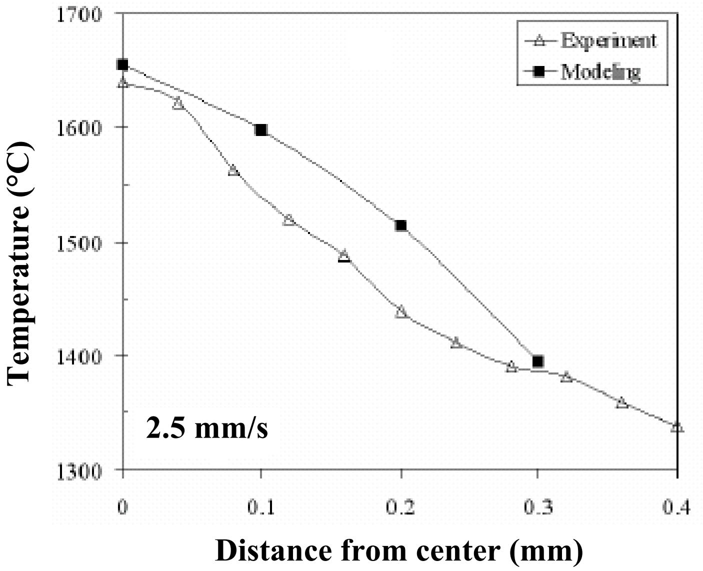

Figure 15. Calculated temperature along depth direction for 600 W and 2.5 mm/s and corresponding measurements for Sample 4 from Reference [20].

In both directions, the model closely approximates the change in temperature with increasing distance from the molten pool center.

1.2.3.3 Process Optimization

Several authors have published studies into the optimization of the LENS^{TM} process to produce favorable thermal or mechanical properties. Hofmeister *et al.* [7] observed via radiation pyrometry that the molten pool increases with height in the deposition of a thin plate at constant laser power and translation speed as the substrate and lower layers accumulate heat. The same effect was observed by Wang *et al.* [20] both experimentally and numerically, and numerically by Labudovic *et al* [18]. Hofmeister *et al.* [7] proceeded to present metallographic results that gave an increased grain size in the upper layers of an AISI 316 thin plate compared to the lower layers. This microstructural gradient coincided with decreasing cooling rates and increased molten pool size with distance from the substrate, and likely indicates a similar gradient in mechanical properties. This conclusion is supported by the computational findings of Costa *et al.* [19] shown graphically in Figure 12.

In an effort to produce a uniform distribution of microstructure and mechanical properties throughout the deposited layers, Hofmeister *et al.* [8] devised a closed-loop feedback control system that was intended to maintain a steady molten pool size throughout the deposition process. The feedback controller was incorporated into the pyrometry system used to measure the thermal phenomena of the deposition. A program was integrated into the system that reduced the input laser power when the molten pool area exceeded an operator-specified value. The results shown in Figure 16 compare the molten pool sizes of cases run with and without the feedback system for the deposition of a thin-walled square perimeter for advancing periods of the build.

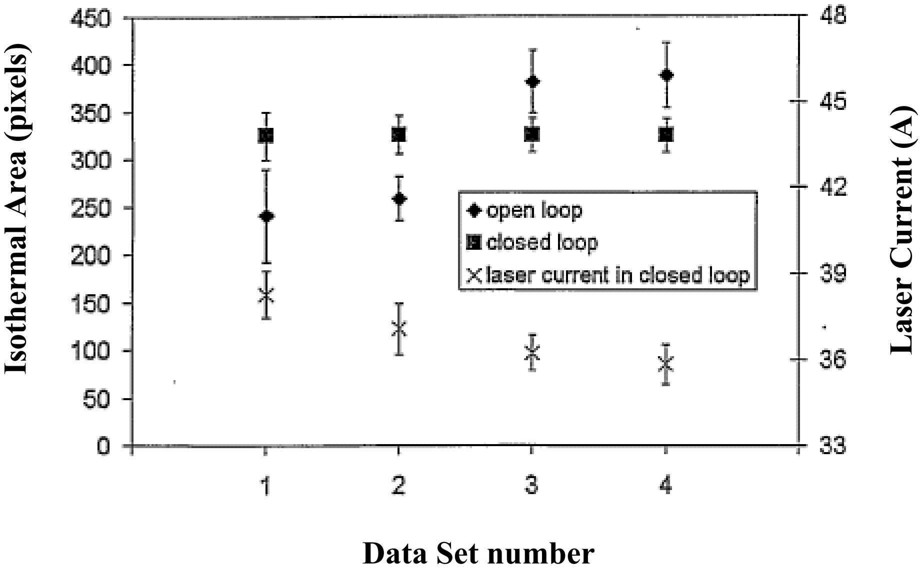

Figure 16. Molten pool size of closed-loop and open loop systems at various stages of deposition from Reference [8].

The plot shows that the isothermal area, i.e. the molten pool area detected by the CCD camera, increases with time throughout the build in the open loop system, which corresponds to a constant laser power setting. However, the molten area remains nearly constant when the closed-loop system is implemented. The figure also shows the decrease in current used by the laser for a closed loop system as the laser power is decreased with successive depositions. The decline in laser current during the four data sets represents a 10% decrease in laser power that was required to maintain the specified molten pool size. Hofmesiter *et al.* [8] speculated that such a control system would be for producing consistent and predictable results in LENS^{TM} depositions.

In an effort to model the controlled-loop feedback mechanism presented in Reference [8], Wang *et al.* [21] applied sequences of decreasing input energy densities to generate a steady molten pool throughout the LENS^{TM} deposition of a thin plate. Wang *et al.* [21] performed the calculations for the deposition of a ten layer plate in SYSWELD® using the same mesh presented in Reference [20], as well as the same boundary and initial conditions. The energy density load was again represented by a Gaussian function with 1.0 mm^3 distribution and the plate material chosen as multi-phased X20Cr13 stainless steel, for which the thermal properties and continuous cooling transformation (CCT) diagram were available in the SYSWELD® database.

Wang *et al.* [21] first considered a deposition at $\frac{dy}{dt} = 7.62$ mm/s, performing numerous simulations to determine the sequence of energy density settings necessary to maintain a pool length of approximately 2.0 mm in the Y-direction. Having already calculated a laser efficiency of approximately 36.4% through comparison of simulated results to the experimental findings of Hofmeister *et al.* [6], the group found the sequence of P_L that would be used for the build. The sequence and the temperature distributions for several layers are shown in Figure 17. The size of the molten pool is shown to remain nearly constant throughout the build, yet some growth can be observed in length (Y-direction) and depth (Z-direction) as the deposition advances.

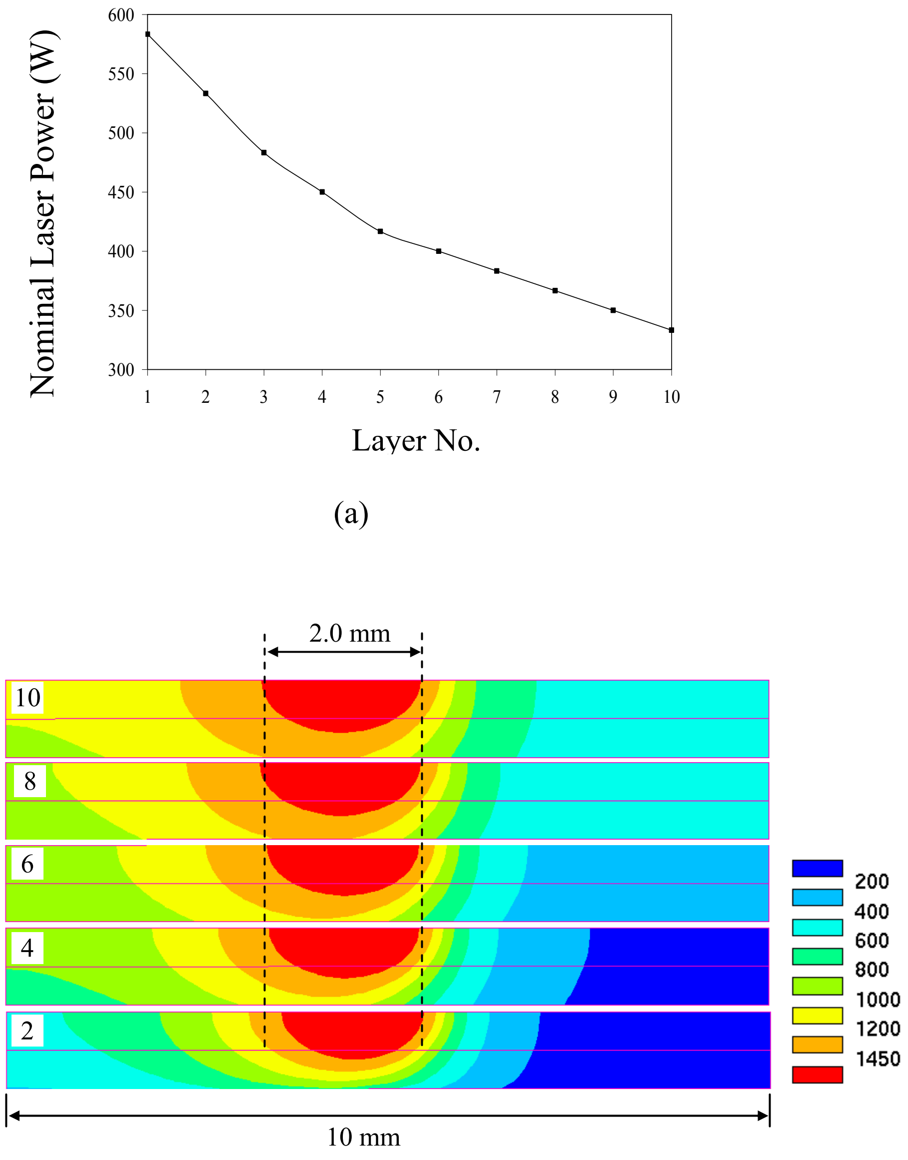

(a)

(b)

Figure 17. Laser power (P_L) used for each layer to maintain molten pool size of approximately 2 mm at $\frac{dy}{dt}$ = 7.62 mm/s. (b) Molten pool size and temperature distribution during deposition of Layer 2, 4, 6, 8, and 10 when laser at center of plate width from Reference [21].

The resulting thermal histories for each layer are presented in Figure 18, which is a plot of temperature vs. time for points located at the centers of Layers 1, 3, 5, and 10 along the vertical plate axis during the entire build process. The plot indicates that the maximum temperature generated at the midpoint of each layer changes little throughout the deposition when the optimization scheme is applied. The temperature below which martensite begins to precipitate is indicated in Figure 18 as $M_s = 350$ °C. After each laser pass, the temperature in Layer 1 quickly cools to below M_s only to be heated above it again during the next pass. Layer 3 shows similar behavior with less cooling, however, beginning with Layer 5 and continuing to Layer 10, cooling is insufficient to reach M_s. The plot shows that despite the laser power reduction, the resulting distribution of 1st generation and tempered martensite will be similar to that predicted by Cost *et al.* [19].

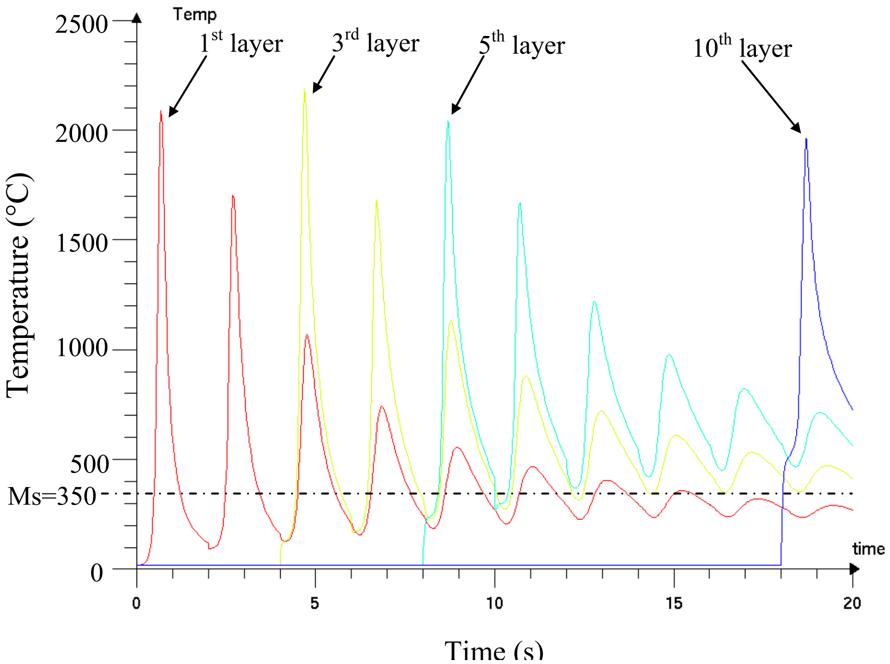

Figure 18. Temperature vs. time at center width of the plate for Layers 1, 3, 5, and 10 from Reference [21].

Wang *et al.* [21] next plotted the progression of the cooling rates at the plate center for Layers 1, 3, 5, and 10 through the build process, which is shown in Figure 19. Figure 19 shows that even though the molten pool remains nearly constant for all layers, the cooling rates are still significantly reduced for the case of optimized power settings.

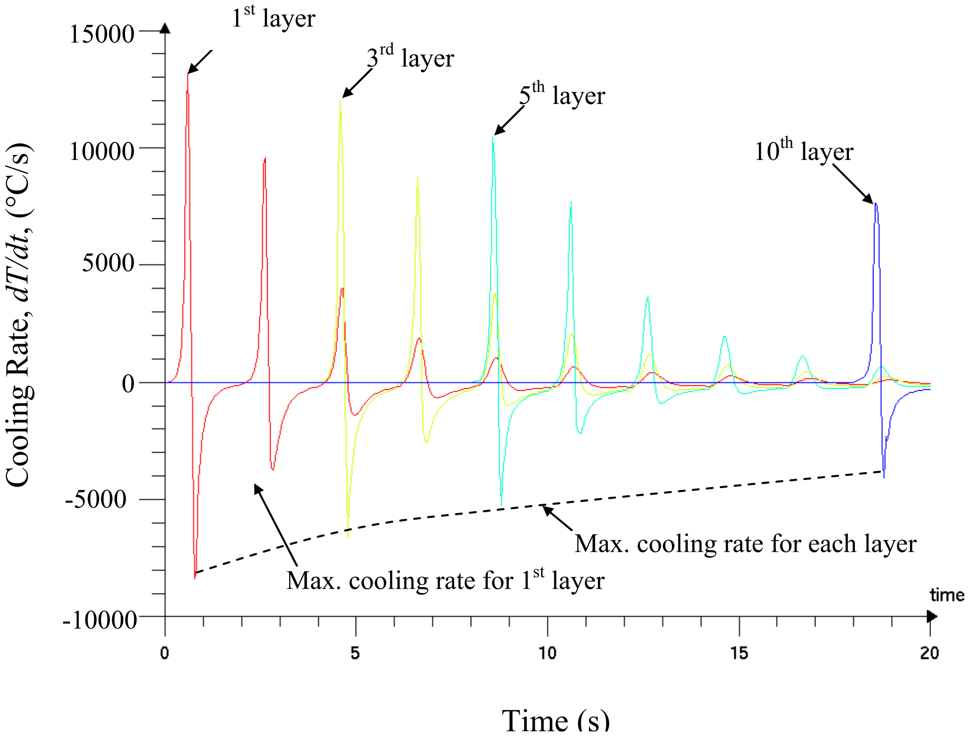

Figure 19. Cooling rate vs. time at center width of the plate for Layers 1, 3, 5, and10 from Reference [21].

Wang *et al*. [21] next applied the molten pool optimization process to the cases of $\frac{dy}{dt} = 2.5$ mm/s and $\frac{dy}{dt} = 20$ mm/s to determine the effect of varying the laser translation speed on the molten pool dimensions. Repeating the previous procedure, Wang *et al.* [21] found the necessary sequences to maintain a molten pool length of 2 mm. Figure 20 is a plot of for each layer at the three translation speeds. The plot shows that the required laser power increases with $\frac{dy}{dt}$. The resulting molten pool geometry at the midpoint of Layer 10 for each value of $\frac{dx}{dt}$ is shown in Figure 21. The figure shows that the shape of the molten pool changes with $\frac{dy}{dt}$, becoming elongated in the Y-direction and shallower in the Z-direction with higher speed. Accordingly, the model predicts less re-heating of the previously deposited layers with increased $\frac{dy}{dt}$ and the average value of P_L for the ten layers.

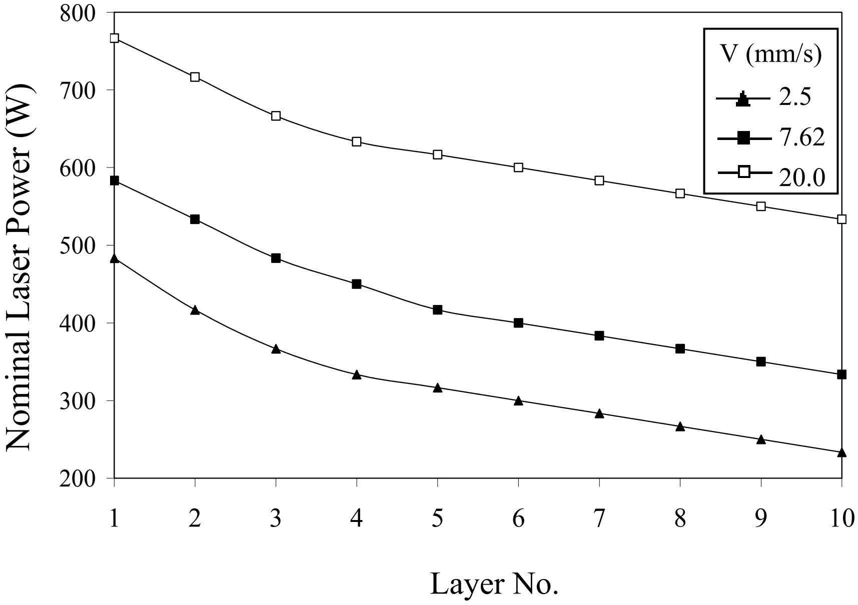

Figure 20. Applied laser power (P_L) used for each layer to maintain molten pool size of approximately 2 mm at $\frac{dy}{dt}$=2.5, 7.62, 20.0 mm/s from Reference [21].

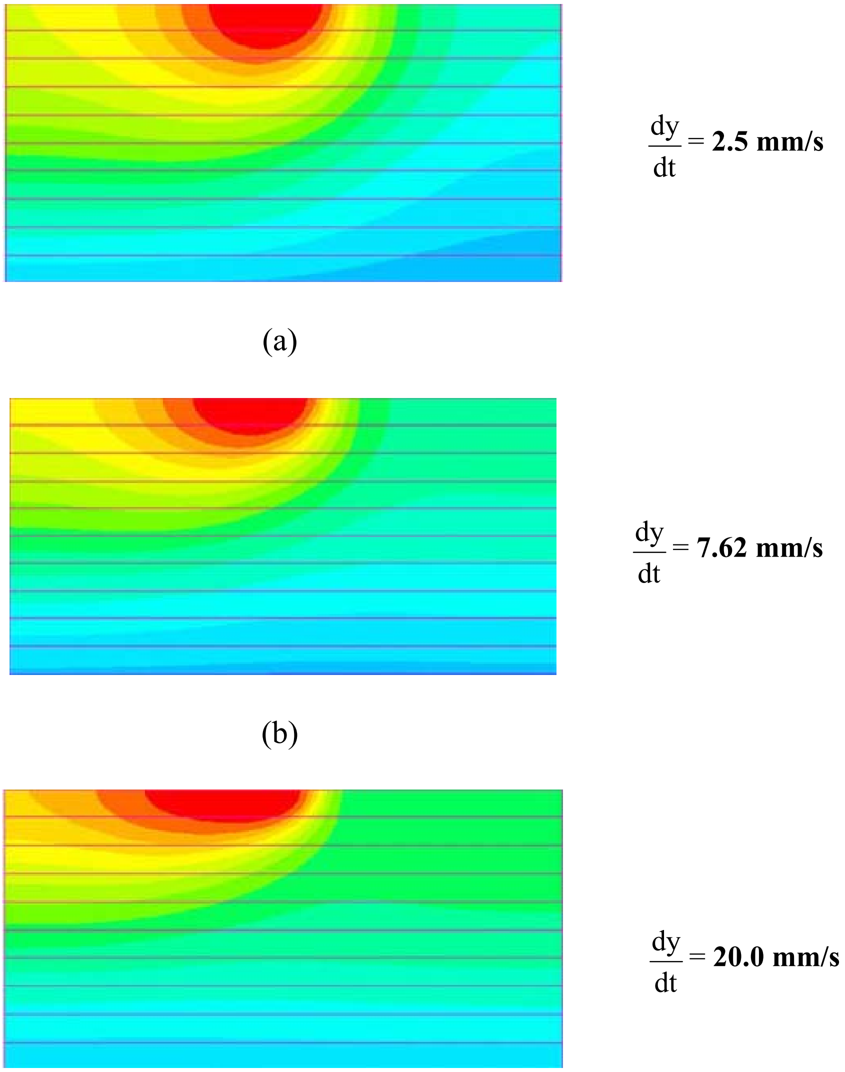

(a)

(b)

(c)

Figure 21. Molten pool size and shape at center of plate in Layer 10 at $\frac{dy}{dt}$ = (a) 2.5 mm/s, (b) 7.62 mm/s, (c) 20 mm/s from Reference [21].

Vasinonta *et al.* [22] sought to create a process map for generating steady molten pool sizes and limiting residual stress magnitudes. Accordingly, the group performed a series of weakly-coupled thermo-mechanical analyses using a 2-D FE model to simulate the heating of a thin plate of AISI 304 stainless steel of some height, *H*. The mesh was composed of 4-node bilinear elements and calculations were performed using ABAQUS®. Unlike other studies, Vasinonta *et al.* [22] chose to model the laser as a point source rather than a distributed energy density. Additionally, the convection and radiation were neglected.

Based upon analytical modeling of a moving heat source performed by Rosenthal, Vasinonta *et al.* [22] selected three features of the process for non-dimensionalization: molten pool length, layer height (height of at which deposition is occurring), and melting temperature. The group then performed a series of thermal simulations with input parameters P_L and $\frac{dy}{dt}$ ranging from 43.2 W-165 W and 5.93 mm/s-9.31 mm/s, respectively. The calculations were performed for temperature-independent material properties and were used to generate a surface of dimensionless pool length as a function of dimensionless melting temperature and plate height. The resulting 3-D plot showed a strong dependence of pool length on melting temperature for all values of non-dimensional H. A strong dependency on non-dimensional H was only observed for case of short walls. Based on the non-dimensionalized parameters, which were normalized with P_L and $\frac{dy}{dt}$, Vasinonta *et al.* [22] predicted values of molten pool size for different translation speeds and laser powers, as shown. These modeling results are plotted against experimental data in Figure 22. The plot shows good agreement at all laser powers for $\frac{dy}{dt}$ = 7.62 and 9.31 mm/s, though deviation is seen at $\frac{dy}{dt}$ = 5.93 mm/s.

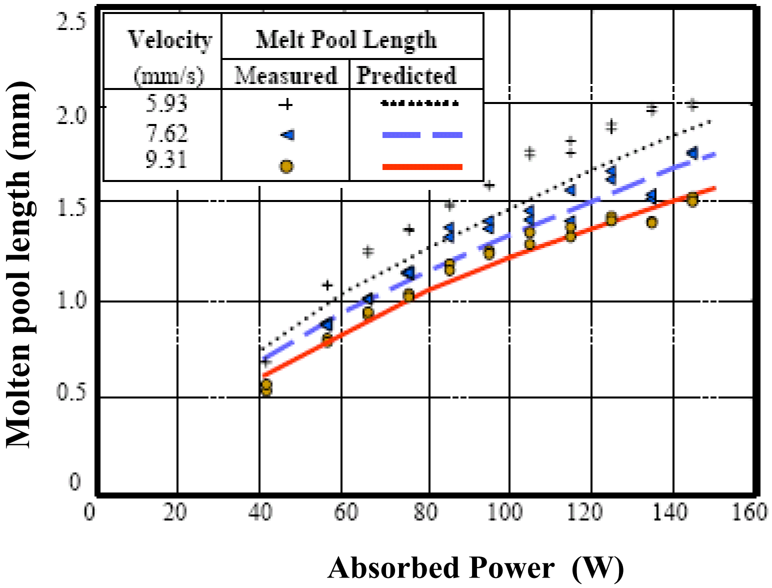

Figure 22. Molten pool size as function of P_L and from non-dimensional process map from Reference [22].

The group also developed a non-dimensionalization procedure for temperature gradient as a function of non-dimensional height and non-dimensional temperature along the top of the plate. Once again, these variables were described in terms of P_L and $\frac{dy}{dt}$. The generated surface showed a strong dependency of temperature gradient on temperature along the upper plate edge and, as seen with melt pool length, on non-dimensional height only for short plates. Vasinonta *et al.* [22] proceeded with a series of thermo-mechanical simulations using different P_L and $\frac{dy}{dt}$ and plotted the ratio of maximum residual stress magnitude to yield strength as a function of temperature gradient. The results revealed a strong dependency of residual stress magnitude on the temperature gradient, which represented the heterogeneous temperature distribution responsible for thermal strains in the LENS$^{\text{TM}}$. The modeling results are shown in Figure 23 for various values of P_L, $\frac{\text{dy}}{\text{dt}}$, and preheat temperature of the substrate.

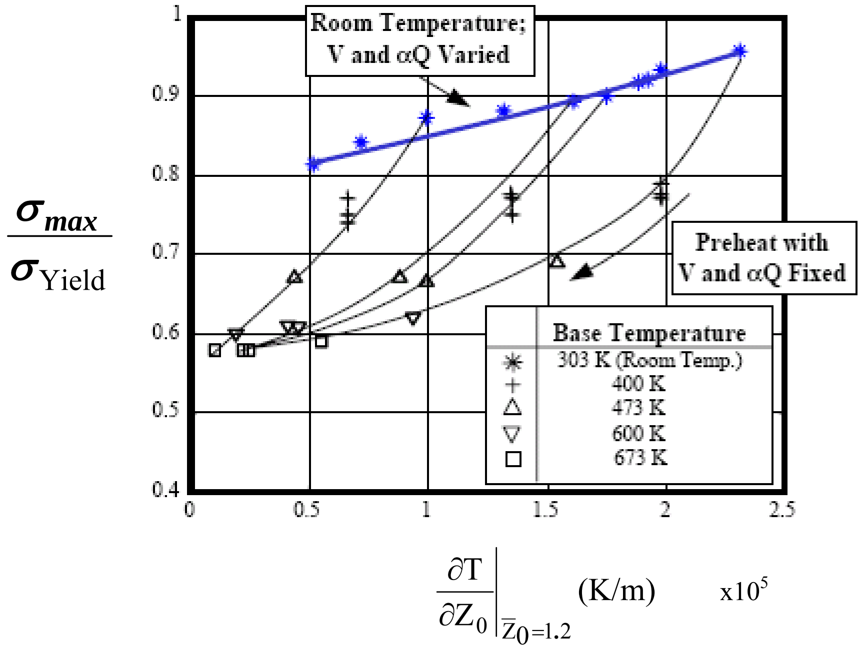

Figure 23. Maximum residual stress as function of temperature gradient from Reference [22].

Based on the figure, Vasinonta *et al.* [22] theorized that two methods exist for reducing the stress magnitudes. Firstly, reduction of the temperature gradient through modification of P_L and $\frac{\text{dy}}{\text{dt}}$, and secondly, altering the yield stress of the material through preheating of the substrate. The plot predicted a 20% decrease in stress for a room temperature substrate by reducing the temperature gradient and a 40% decrease at through preheating to 673 K for a temperature gradient of 0.5. Vasinonta *et al.* [22]

concluded that the generated process maps could be used for optimizing both the stress state and molten pools if proper modification of P_L and $\frac{\mathrm{dy}}{\mathrm{dt}}$ are considered.

CHAPTER 2

ANALYSIS OF THIN PLATES PRODUCED BY LENS™

2.1 Overview

In order to select the appropriate values of the process parameters, laser power and translation speed needed to minimize residual stresses in LENS^{TM} components, their relationships must be better understood. Rangaswamy *et al.* [11,12] measured the residual stresses at several locations within LENS^{TM} thin plates using neutron diffraction, while Labudovic *et al.* [18] used X-ray diffraction to measure the stresses near the deposit/substrate interface for a LENS^{TM} plate deposit. However, neither of these studies examined the role of process parameters in determining the stress magnitudes or distributions. Furthermore, Vasinonta *et al.* [22] restricted their measurements to the lower regions of the plate and selected a measurement technique, X-ray diffraction, which is only capable of nanometer scale penetration into the material.

Accordingly, the effort presented here involves measurement by neutron diffraction of LENS^{TM}-deposited thin plates of AISI 410 stainless steel produced using different combinations of laser power and translation speed. The distributions and the magnitudes of the internal stresses were analyzed to determine if a process map can be generated for optimizing the selection of values for these inputs. Furthermore, the experimental data were compared with numerical results to qualify a FE model developed for predicted residual stresses in LENS^{TM} thin plates. The computational simulations were performed with SYSWELD® using a coupled thermo-mechanical-metallurgical model and the mesh presented by Wang *et al.* [20].

Additionally, a multi-phase internal state variable model that may provide better accuracy for the prediction of residual stresses is presented. Since this constitutive model cannot be easily implemented in SYSWELD®, the experimental plate depositions are simulated with a thermal model using ABAQUS® 6.7. These results were compared to the SYSWELD® calculations, as well as to experimental thermal data from collected by Wang *et al.* [20] to verify the use of ABAQUS® for modeling LENS^{TM}.

2.2 Experimentation

2.2.1 Introduction

In order to relate the resulting residual stresses from the LENS™ build process to the process parameters laser power and stage translation speed, seven of the ten AISI 410 stainless steel thin plates presented by Wang *et al.* [20] are selected for stress measurement. The plates were fabricated at the facilities of Optomec®, a private company specializing in LENS™ manufacturing and repair, using a LENS™ 850M machine. This machine is equipped with a 3kW IPG laser and a 5-axis stage for part deposition. The process parameters used in the building of each plate are shown in Table 1.

Table 1. Sample LENS™ plates of AISI 410 and corresponding input parameters.

No.	**Laser Power (W)**	**Laser Speed (mm/sec)**	**Length of Part (mm)**	**Powder Flow Rate (cm^3/sec)**
1	300	2.5	38.1	37.85
2	300	2.5	22.1	37.85
3	300	4.2	25.4	50.47
4	600	2.5	25.4	37.85
5	600	4.2	25.4	44.16
6	450	2.5	25.4	37.85
7	450	4.2	25.4	50.47
8	300	8.5	38.1	88.3
9	450	8.5	38.1	82.01
10	600	8.5	38.1	88.3

The sample plates each consisted of 25 single-pass layers. The widths of the plates (Y-direction) varied somewhat from sample to sample, yet were all within 22-38mm. The height (Z-direction) remained constant at 15 mm, while the thicknesses ranged from 1 mm to 3 mm based upon process parameters – larger laser powers and lower travel speeds melt more powder. A representative sample plate is shown in Figure 24.

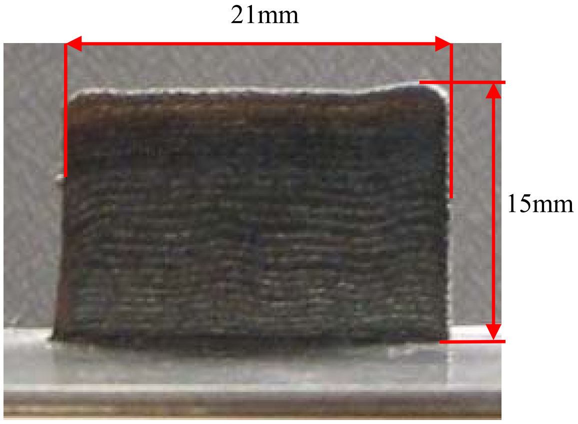

Figure 24. LENS™-produced thin-walled plate of AISI 410.

2.2.2 Experimental Procedure

Several methods are available for determining residual stress, such as holographic interferometry by hole-drilling, the contour method, and X-ray diffraction. However, in most cases such methods are destructive in nature or are only capable of measuring stress close to free surfaces. Neutron diffraction, however, a long established measurement technique, is capable of deep penetration into solid materials for stress determination in a nondestructive fashion. Accordingly, this option was chosen to measure the stress distribution within the LENS™ AISI 410. Due to limited availability of the diffraction instrumentation, only seven of the ten plates produced by Wang *et al.* [20] could be measured.

The neutron diffraction measurements were performed at the High Flux Isotope Reactor (HFIR) facility at Oak Ridge National Laboratory on the NSFR2 diffractometer. The neutron diffractometry system at HFIR, shown in Figure 25, makes use of a single crystal silicon monochromator that selects neutrons of a particular wavelength (monochromatic) from the reactor stream to bombard the measured sample.

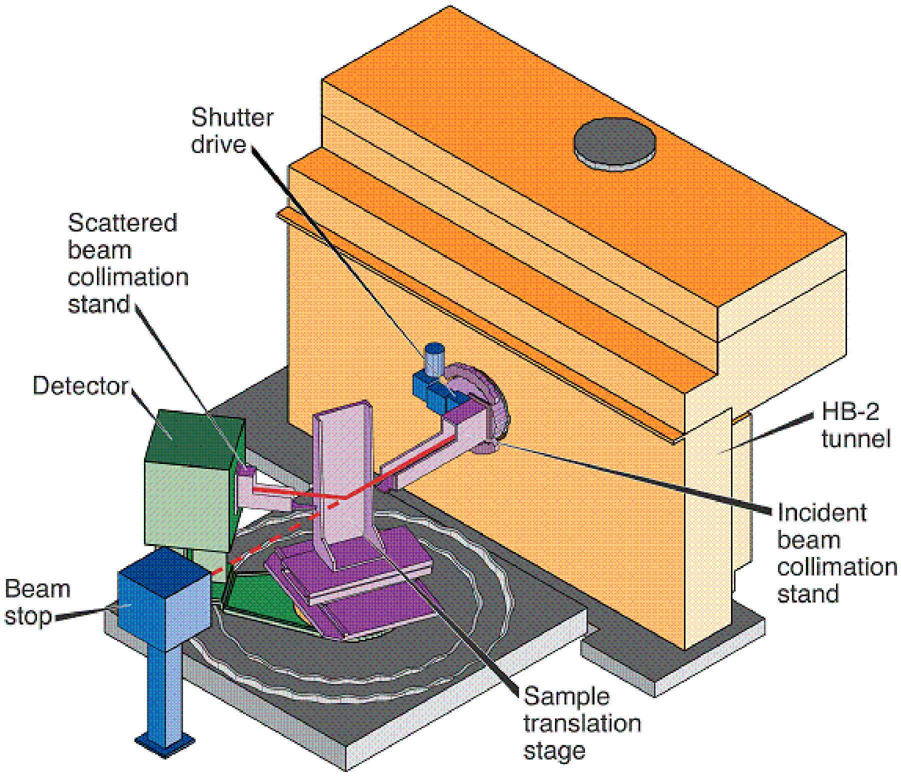

Figure 25. Neutron diffractometry arrangement at HFIR.

Upon contacting the sample material, some neutrons are diffracted by crystalline lattice planes of a certain orientation that is dependent on the selected neutron wavelength. If the path difference of the particles as they diffract from different individual planes is some integer of the wavelength, the neutrons interfere constructively, and the intensity peak is recorded by seven detectors arranged from -15 ° to +15 ° out of the horizontal plane of diffraction. The NSFR2 peak fitting program then determines the angle of diffraction, *2θ*, by plotting a Gaussian distribution of neutron count vs. angle. The program then calculates the spacing between crystalline lattice planes, d_{hkl}, through Bragg's Law of Diffraction, shown here as Equation 1 [23].

$$\lambda = 2\mathrm{d}_{hkl} \sin\theta \tag{1}$$

The diffracting lattice planes in this process are those with plane normals parallel to the scattering vector, $\vec{\mathrm{Q}}$, which is defined in Equation 2 [10].

$$\vec{\mathrm{Q}} = \vec{\mathrm{q}}_{\mathrm{incident}} - \vec{\mathrm{q}}_{\mathrm{diffracted}} \tag{2}$$

The diffraction process is shown in Figure 26.

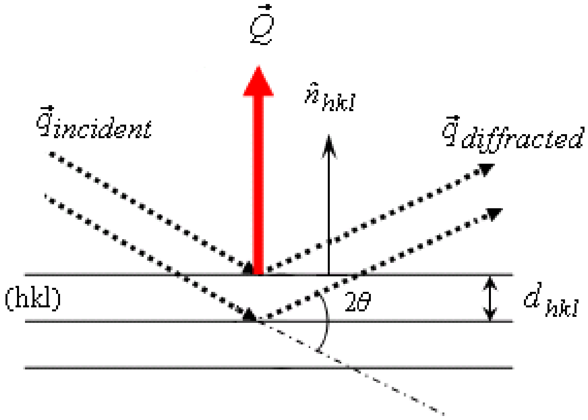

Figure 26. Diffraction of neutrons from crystalline planes.

In the measurement of the LENS™ plates, the {330} planes of the silicon monochormator were selected to diffract neutrons of 1.73 Å wavelength that were then directed onto the sample plates. The measured diffraction angle of the detected neutrons after contacting the sample was approximately 94.6 °. In order to determine what orientation {*hkl*} of lattice planes within the sample material was diffracting, X-ray diffraction was performed on a representative plate sample. In this procedure, monochromatic X-rays of $\lambda \approx 1.5$ Å were directed onto the polished surface of the plate, resulting in a high intensity peak at an angle of approximately 90 °. The measured diffraction profile was referenced against a database of profiles for various materials and was found to closely match that of iron for which the {211} planes diffract at $2\theta \approx 90$ °. Accordingly, the {211} planes were determined to be those diffracting for AISI 410.

In order to determine how the internal stress varied with position within the sample plates, several locations were selected for the placement of gauge volumes, 3-D data sampling regions created by the intersection of the incident and diffracted neutron beams. The values of d_{hkl} calculated from 2θ measurements at these sites would be averaged throughout the gauge volumes to obtain a single value for each selected location. The dimensions of the gauge volumes were determined by those of the incident and diffraction collimator slits through which the neutrons passed before and after contacting the sample, respectively. The need to fully embed the gauge volumes within the geometry of the thin plates required small slit sizes that resulted in rectangular shaped volumes of approximately 2.5 mm^3.

The arrangement of the gauge volumes, show in Figure 27, closely matches that used by Rangaswamy *et al*. [11], shown in Figure 5, with seven volumes equally spaced along the vertical (Z-direction) centerline of each plate and four volumes along the horizontal (Y-direction) centerlines. However, in the case of two of the samples (1,4), nine volumes were used vertically and six horizontally.

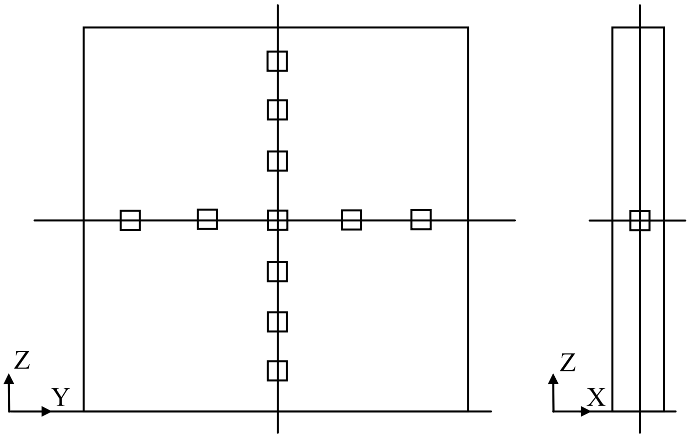

Figure 27. Data sampling locations within AISI 410 LENS™ plates.

The measurements were taken at count times of 6-35 minutes and were performed three times at each gauge volume. Before each repetition, the sample was oriented to align the scattering vector, $\vec{Q}$, with one of the three orthogonal directions of the sample coordinate system (X,Y,Z) in order to measure the average value of d_{hkl} in that direction.

In order to convert the recorded lattice spacing values into strains, a strain-free reference value of d_{hkl} was required. Therefore, a coupon was cut from another LENS™ AISI 410 plate to be measured along with each test sample. Once cut, the elastic strains in the coupon relaxed so that the measured lattice spacing, d_o, represented an unstrained, initial state. The elastic strains were then calculated for the X, Y, and Z directions through Equation 3 [25].

$$\varepsilon_{\mathrm{hkl,i}} = \frac{\mathrm{d}_{\mathrm{hkl,i}} - \bar{\mathrm{d}}_{\mathrm{o}}}{\bar{\mathrm{d}}_{\mathrm{o}}} \tag{3}$$

where $i = \mathrm{X, Y, Z}$

$$\bar{\mathrm{d}}_{\mathrm{o}} = \frac{1}{3}\sum_{\mathrm{i}} \mathrm{d}_{\mathrm{o,i}}$$

In order to avoid the propagation of systematic errors in 2θ measurement into the $\varepsilon_{\mathrm{hkl}}$ calculations, the values of d_o and d_{hkl} for each sample were taken during the same experimental run, so that such errors would cancel in Equation 3. Additionally, to reduce the impact of random errors on the strain calculations, replicate measurements of d_o were taken during each run. Furthermore, to account for any differences in the value of $\mathrm{d}_{\mathrm{o,i}}$ for different directions resulting from any plastic deformation that might be present, the average reference lattice spacing, $\bar{d}_o$, is used instead. The presence of plasticity in the LENS$^{\mathrm{TM}}$ material and the error in recorded d_o values is discussed in more detail in Section 2.2.3.

The relation of the measurement directions to the coordinate system of the sample is expressed by the angles ψ and φ as shown in Figure 28.

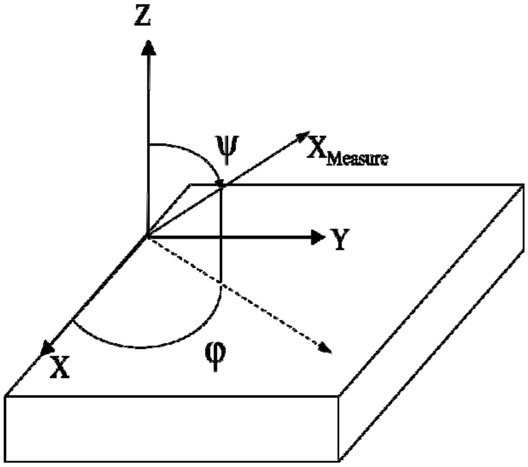

Figure 28. Measurement direction with respect to sample coordinate system.

As such, an alternative form of Equation 3 that represents the strain in the measurement direction in terms of the components of the 2nd order strain tensor is given in Equation 4 [25].

$$\varepsilon_{\varphi\psi} = \varepsilon_{11} cos^2\phi sin^2\psi + \varepsilon_{22} sin^2\phi sin^2\psi + \varepsilon_{33} cos^2\psi + \varepsilon_{12} sin2\phi sin^2\psi + \varepsilon_{13} cos\phi sin2\psi + \varepsilon_{23} sin\phi sin2\psi \quad (4)$$

By aligning the scattering vector $\vec{Q}$ with the orthogonal axes of the LENS™ plates, those values of strain calculated with Equation 3 in the X, Y, and Z directions correspond to $\varepsilon_{0^o,90^o}$, $\varepsilon_{90^o,90^o}$, and $\varepsilon_{0^o,0^o}$ respectively, in Equation 4. Accordingly, in these directions $\varepsilon_{\varphi\psi}$ reduces to ε_{11}, ε_{22}, and ε_{33}, i.e. the principal strains.

Once the principal elastic strains had been determined at all measurement sites, the corresponding principal stresses were calculated using Hooke's Law, shown in Equation 5 [25].

$$\boldsymbol{\sigma}_{\mathrm{hkl,i}} = \frac{\mathrm{E}_{\mathrm{hkl}}\boldsymbol{\varepsilon}_{\mathrm{hkl,i}}}{(1+\boldsymbol{\nu}_{\mathrm{hkl}})} + \frac{\mathrm{E}_{\mathrm{hkl}}\boldsymbol{\nu}_{\mathrm{hkl}}(\boldsymbol{\varepsilon}_{\mathrm{i}} + \boldsymbol{\varepsilon}_{\mathrm{j}} + \boldsymbol{\varepsilon}_{\mathrm{k}})}{(1+\boldsymbol{\nu}_{\mathrm{hkl}})(1-2\boldsymbol{\nu}_{\mathrm{hkl}})} \quad (5)$$

The terms $\mathrm{E}_{\mathrm{hkl}}$ and ν_{hkl} are the elastic constants corresponding to Young's modulus and Poisson's ratio in the direction normal to the {211} planes. The values of these terms were found using an algorithm developed by Behnken and Hauk [26] for calculating {*hkl*}-specific elastic response for polycrystals from the single crystal compliance tensor of a material. Since no such compliance data was available in the literature for AISI 410 single crystals, values of α ferrite compliances recorded by Dever [27] were used instead. The Behnken-Hauk algorithm is based on a polycrystalline elastic model developed by Kröner [28] which assumes a random grain orientation is present within the material under consideration. The applicability of this model to the LENS™ plates was verified through the neutron measurements for which no change in diffracted intensity was detected that would be indicative of a significant texture in the deposited material.

2.2.3 Results and Analysis

Initial data retrieval revealed that the Debye ring, the profile created by the diffracted neutrons as they contact the detectors, was not well defined, indicating that the number of grains in the sample material contributing to diffraction was low. In order to avoid the random errors in d_{hkl} that would result from the poor grain statistics, an omega oscillation was performed whereby the sample was rotated through an angular range of -4° to +4° out of the plane normal to the incoming beam to increase the number of diffracting grains. This procedure was unable to correct the Debye ring profile completely, but did significantly improve the quality.

Based upon the stress vs. position plots produced for the Rangaswamy *et al.* [11], which indicated that the stresses in the X (normal) and Y (transverse) directions were almost negligible over most of the sample, and the limited time available for measurements at the HFIR facility, the data was recorded almost exclusively in the sample Z direction (longitudinal). In order to validate this decision, measurements of Sample 4 were performed in all three directions. The calculated orthogonal stresses for Sample 4 are shown in Figure 30 (a) and (b), where the "free end" in Figure 29 (a) refers to the last deposited layer of material, i.e. the top of the plate.

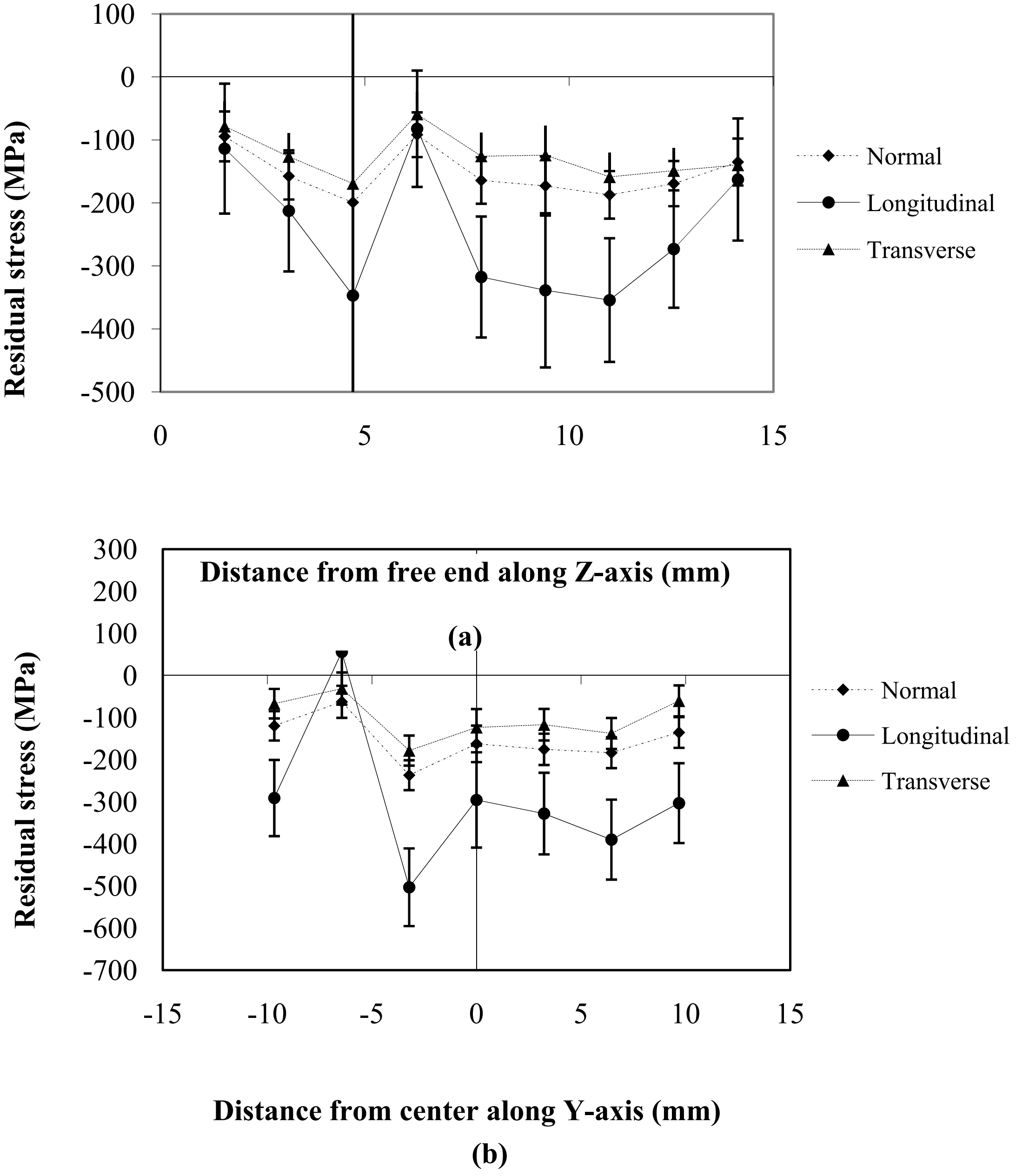

Figure 29. Stress components as functions of position along (a) Z-axis of plate and (b) Y-axis of plate for Sample 4.

The plots in Figure 29 show the stress distribution along the vertical and horizontal plate centerlines with data points corresponding to the arrangement shown in Figure 27.

Contrary to the findings presented by Rangaswamy *et al.* [11], the magnitudes of the X and Y stress components, σ_{X} and σ_{Y} , are here found here to be reasonably large, ranging from 50-200 MPa. However, these stresses are still comparatively small enough in relation to σ_{Z} that the decision to restrict measurements to the Z-direction was reasonable in consideration of the time constraints. The resulting Z-component of stress, σ_z , along vertical and horizontal plate centerlines are shown for each sample in Figures 30 and 31.

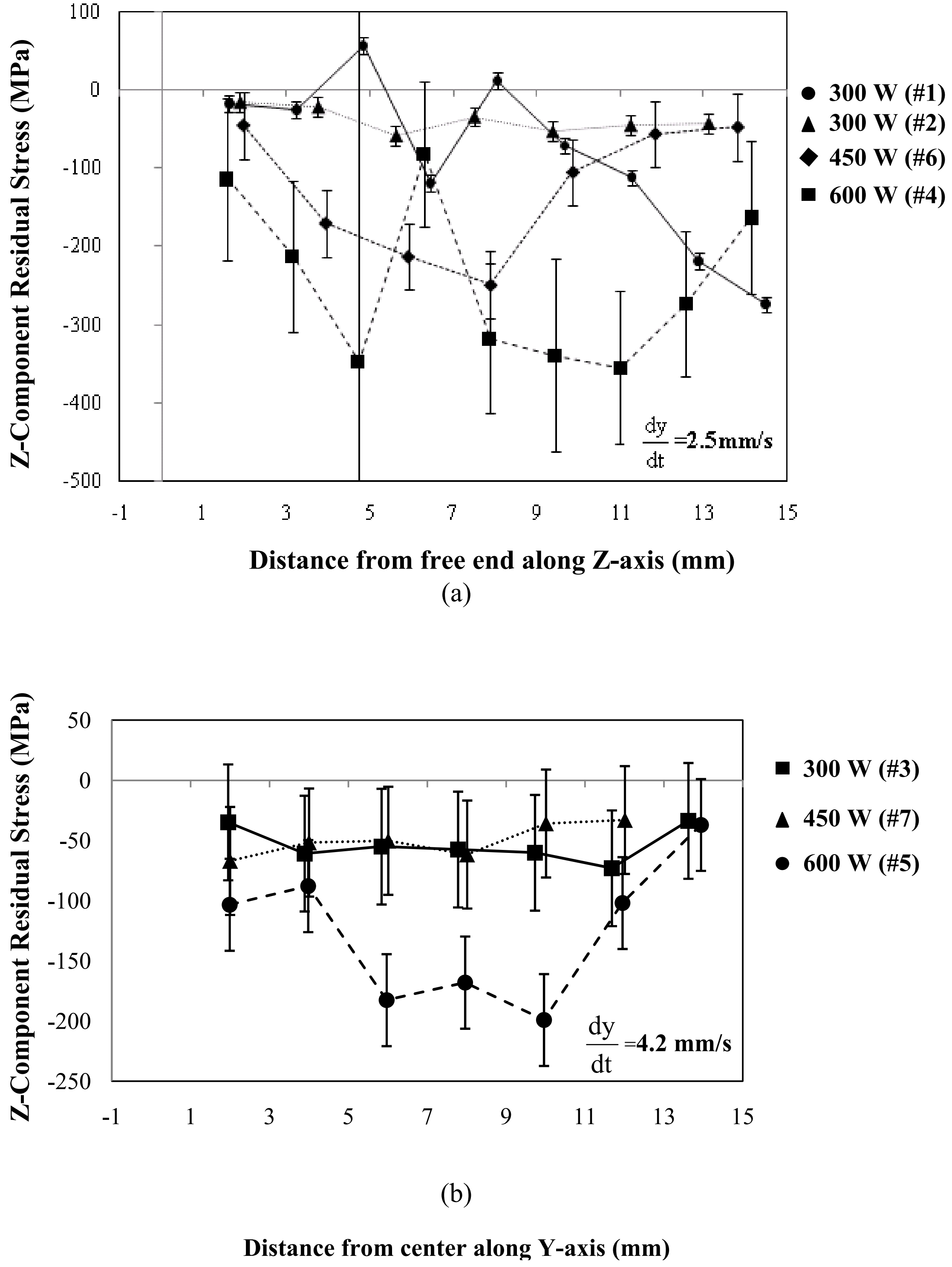

(a)

(b)

Figure 30. σ_z as function of position along Z-axis of plate for different laser powers at $\frac{dy}{dt}$ =(a) 2.5 mm/s (b) 4.2 mm/s.

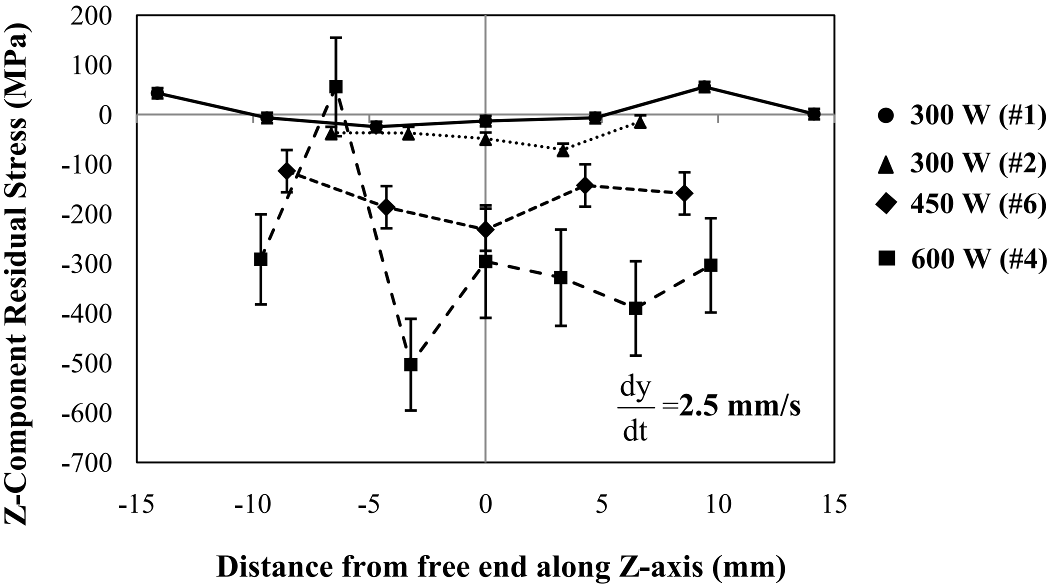

(a)

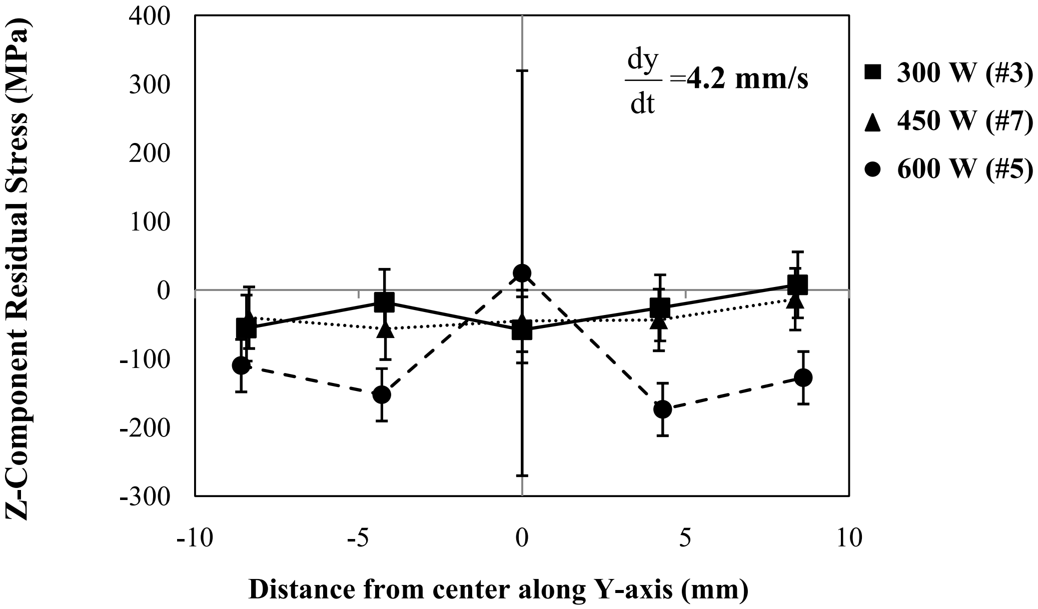

(b)

Figure 31. σ_z as function of position along Y-axis of plate for different laser power at $\frac{dy}{dt}$ =(a) 2.5 mm/s (b) 4.2 mm/s.

The error in calculated stress, shown as bars at each data point in the figures, was obtained by propagation of the random error in 2θ and d_o measurement through Equations 1, 3, and 5. The random 2θ error was determined by the NSFR2 peak fitting program, while that for d_o was determined through replicate measurements taken during each measurement run. An uncertainty analysis of the d_o values for each sample produced a root-mean square deviation from the average ranging from 5×10^{-5} to 4×10^{-4} Å. An extremely large error in stress is shown in Figures 29 (a) and 30 (a) at the third gage volume from the free end for Sample 4. A comparison with the raw data revealed a similarly large variance of 2θ at this location, which may be due to the presence of a large grain or some type of defect within the gauge volume that interrupted the uniformity of the Debye profile across the seven neutron detectors and produce an artificial shift in the Gaussian curve.

Sources of uncertainty in the magnitudes of the stress calculations that were not considered when calculating the error shown in the plots were the choice in elastic constants and plastic strain in the material. Firstly, the elastic constants used in Equation 5, E_{hkl} and ν_{hkl}, were calculated from single crystal compliances for α ferrite, which are likely somewhat different from those of a martensitic steel like AISI 410. However, since no such constants could be found in the literature for AISI 410 or any other martensitic steels, no direct comparison to α ferrite elastic properties could be made and the amount of variation is unknown. Another possible source of error in the stress magnitudes arises from the presence of plastic deformation. Since plastic and elastic strains cannot be differentiated in the neutron measurements, all lattice deformation greater than that measured within the reference coupon is taken to be elastic strain in

Equation 5. If an equal degree of plasticity exists within the all of the plates and the reference coupon, then its effects would be negated in Equation 3. However, if the amount of plastic deformation varied with the processing conditions from sample to sample, then inaccuracies in the calculated stress fields would be introduced in Equation 3 from this non-uniformity. The value of $\mathrm{d}_{\mathrm{o,i}}$ was averaged amongst the three directions in Equation 3 in order to reduce any directionally-dependent plasticity effects, i.e. varying degrees of plastic deformation in the X, Y, and Z-directions, and obtain a value that was more representative of a strain-free state.

Part (a) of Figures 30 and 31 show that the longitudinal stress is mostly compressive along the vertical axis of each plate. Some variation in the stress profiles is observed amongst the different plates; for instance, Samples 1 and 2 show σ_z increasing with distance from farther from the free end, while Samples 3, 4, 5, and 6 show the stress magnitude reaching a maximum near the plate centers and then decreasing closer to the plate bottom. For Sample 7, however, σ_z is a maximum near the free end, while continuously decreasing with distance in the direction of the substrate.

Part (b) of Figures 30 and 31 also show σ_z generally reaching a maximum near the plate center and decreasing with distance on either side. Sample 5, which shows a tensile stress at the center, is an exception, however, a large uncertainty is calculated at this data point, so this may not be a true deviation from the observed trend. The corresponding plot from Rangaswamy *et al.* [11], shown in Figure 6 (b), also shows σ_z to be compressive near the plate center, but then becoming tensile on either side. Since a balanced state of stress exists within the plates, σ_z must necessarily be tensile near the outer surfaces of the samples. By locating their extreme gauge volumes closer to the outer edges of the plates, Rangaswamy *et al.* [11,12] were able to capture this transition, which was only recorded for Sample 1 of this study, shown in Figure 31 (a).

For some cases, such as Sample 1 in Figure 30 (a) and Sample 4 in Figure 31 (a) substantial peaks are seen in the distributions that interrupt the general trends toward increasing or decreasing values of σ_z. Such peaks could be attributable to grain size affects where grains with dimensions on the order of those of the gauge volumes generate shifts in the Gaussian profile. In order to determine if this was the case, several of the sample plates were mounted and polished so that electron back scatter diffraction (EBSD) could be deformed. The EBSD scans were performed at the Center for Advanced Vehicular Systems at Mississippi State University using a SUPRA 40 FEG scanning electron microscope (SEM). The EBSD analysis produced grain size distributions, such as that shown in Figure 32, at several locations within the sample plates.

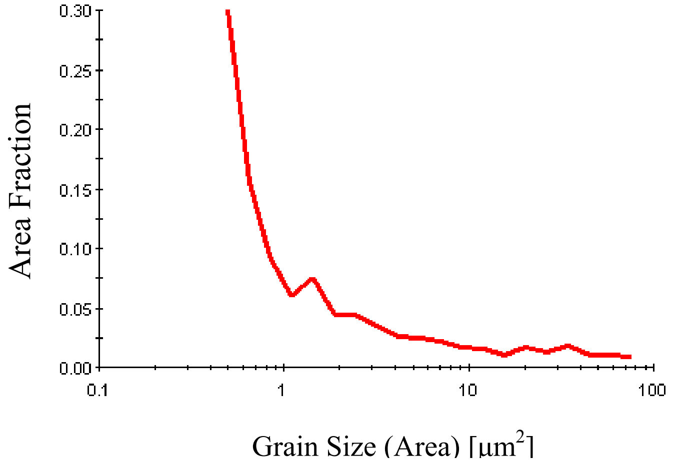

Figure 32. Area fraction of grains of different sizes from plate Sample 4, obtained by EBSD analysis.

Figure 32 shows that approximately 90% of the grains at the measurement location have a cross sectional area of less than 10μm^2, which is significantly less than the cross sectional area of the incoming neutron beam, 3.5 mm^2. These results show that LENS™ material has a very fine grain structure and that the observed peaks are likely not caused by the boundaries of large grains intersecting the sample volumes. In order to determine if other defects were present in the material, the polished samples were examined with optical microscopy. Observation of one of the samples revealed large objects, such as those shown in Figure 33, some of which were approximately 200μm in length These defects are likely pores generated during the LENS™ build process and may be large enough to cause the stress peaks observed in the some of the sample plates by shifting the diffraction profile.

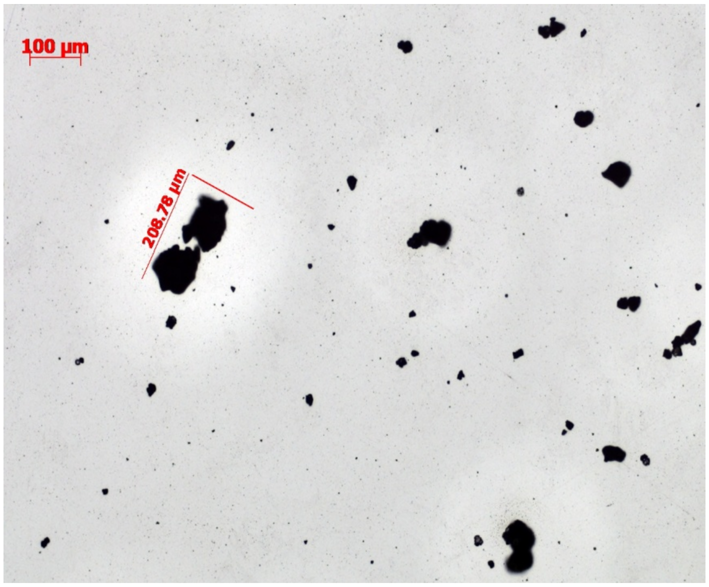

Figure 33. Defects observed in AISI 410 LENS™ plate with optical microscopy at 5x magnification.

An analysis of the data in Figures 30 and 31 seem to indicate larger stress magnitudes associated with larger input laser powers for the same $\frac{dy}{dt}$. In Figures 30 (a) and 31(a), Sample 4, built using P_L = 600 W, has the maximum values of σ_Z, while Sample 6 with P_L = 450 W exhibits the next highest average σ_Z. In Figure 30(b) and 31(b) the maximum values are found in Sample 5, also built with P_L = 600 W. The maximum and average measured values of σ_Z for each plate are shown in Table 2.

Table 2. Maximum and average measured σ_Z in LENS™ plate samples.

Sample #	**Max σ_Z (MPa)**	**Avg. σ_Z (MPa)**	**Laser Power (W)**	**Laser Speed (mm/s)**	**Avg. Stress/Yield Strength of AISI 410**
1	-379.75	-151.43	300	2.5	0.16
2	-70.65	-39.88	300	2.5	0.04
3	-73.08	-43.77	300	4.2	0.05
4	-503.16	-266.13	600	2.5	0.29
5	-199.136	-118.31	600	4.2	0.13
6	-248.69	-143.35	450	2.5	0.15
7	-67.00	-41.78	450	4.2	0.04

Though no mechanical testing was performed to determine the yield strength of LENS™-produced AISI 410, the value for the wrought, as-quenched Fe-Cr 12% type 410 is reported as 930 MPa in the literature [29]. Accordingly, the average measure σ_Z for the cases of Samples 1, 4, 5, and 6 represent an appreciable fraction of the typical yield strength of this material, though the tempering effects of the LENS^{TM} process would likely to result in a somewhat higher actual yield value.

An examination of the yield fraction for plates produced at the same $\frac{dy}{dt}$ supports the previously indicated trend toward greater overall stress magnitudes at higher P_L. However, the magnitudes of the stress field measured within Sample 1 is appreciably higher than that in Sample 2, despite both having been produced at $\frac{dy}{dt}$ = 2.5 mm/s and P_L = 300 W. As shown in Table 1, the length of Sample 1 is nearly twice that of the other specimens, which may suggest that the dimensions of the plates play a key role in the induced stress fields. The precise geometric influence, however, cannot be directly inferred from the measured data. Accordingly, Figure 34 displays the average measured values of σ_Z for $\frac{dy}{dt}$ = 2.5 mm/s and 4.2 mm/s as a function of laser power for a similar plate width, i.e. excluding Sample 1.

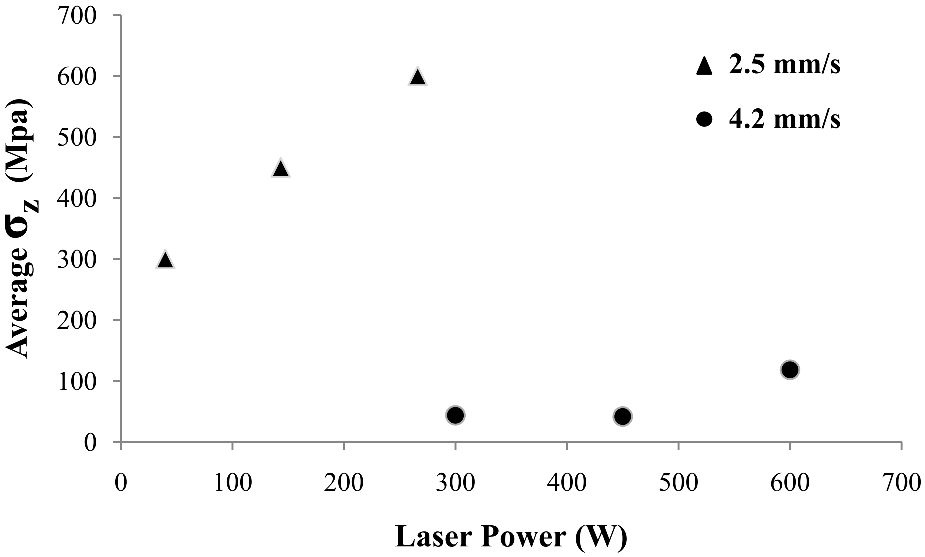

Figure 34. Average measured σ_Z as function of laser power for both translations speeds.

The plots in Figure 34 show a linear relationship of average σ_Z to laser power for $\frac{\mathrm{dy}}{\mathrm{dt}} = 2.5$ mm/s, while that for $\frac{\mathrm{dy}}{\mathrm{dt}} = 4.2$ mm/s is not as clearly defined. The plots indicate that lower stress magnitudes are achievable with reduced $\frac{\mathrm{dy}}{\mathrm{dt}}$ for a given P_L and with reduced P_L for a given $\frac{\mathrm{dy}}{\mathrm{dt}}$ in plates with similar dimensions.

2.2.4 Conclusions

Though some uncertainty exists concerning the accuracy of the calculated stress magnitudes due to the use of α ferrite elastic constants and the possible presence of plastic deformation, a relative comparison between the plates is still valid. A relationship between the measured values of the component of stress in the Z-direction and the input parameters has been identified for plates of similar dimensions in which the average value σ_Z within the samples was linearly proportional to input laser power at $\frac{dy}{dt}$ = 2.5 mm/s, while those plates produced at $\frac{dy}{dt}$ = 4.2 mm/s exhibit a non-linear relationship that still shows lower stress magnitudes obtainable with lower laser powers. The measured values of σ_Z in Sample 1 indicate that a change in geometry may significantly impact the stress fields. However, further measurement of samples with different geometries is needed to fully quantify this effect.

Though more data, i.e. a greater sample population produced with more combinations of P_L and $\frac{dy}{dt}$, would be needed to generate a process map for optimization of the LENS^{TM} process toward minimization of residual stress. The experimentation presented here, specifically the plots in Figure 34, suggest that the magnitudes of the stress fields in simple geometric LENS^{TM} parts may be reduced through a selection of lower values of P_L and $\frac{dy}{dt}$. This finding may be beneficial to industry applications of this process.

2.3 Simulation

2.3.1 Modeling with SYSWELD®

2.3.1.1 Introduction

The same 3-D model used by Wang *et al.* [20] for predicting temperature fields and phase distributions was used in this study to calculate the thermal histories of the deposited AISI 410 plates under varying conditions of laser power and stage translation speed. A more detailed description of the coupled model is provided in Sections 2.3.1.2 and 2.3.1.3., while the constitutive model available in SYSWELD®, for calculating residual stress is presented in detail in Section 2.3.1.4. The implementation of this model and its comparison to the experimental diffraction measurements has been previously published [30].

2.3.1.2 Theoretical Thermodynamic Model

In order to calculate the heat transfer to and from the plate during the LENS^{TM} deposition, a 3-D mathematical model developed by Wang *et al.* [20] was adopted, for which the governing equation is:

$$\left(\sum_i f_i (\rho c_p)_i\right)\frac{\partial T}{\partial t} - \nabla\left(\left(\sum_i f_i k_i\right)\nabla T\right) + \sum_{i<j} L_{ij}A_{ij} = 0 \qquad (6)$$

The heat source, simulating the laser, was modeled with the same Gaussian-conical-distribution used by Wang *et al.* [20] and is described by the equation:

$$Q_r(x,y,z) = Q_o \, \boldsymbol{exp}\left(- \frac{x^2 + y^2}{\left[r_e + \frac{r_i - r_e}{z_i - z_e}(z - z_e) \right]^2} \right) \tag{7}$$

An ambient temperature was used as the initial condition throughout the domain before the start of deposition, while the boundary conditions are described by:

Lower surface of substrate: $T(x,y,z=0) = T_o$ (8)

Sides of plate: $k(\nabla T \cdot \vec{n})\big|_\Omega = h(T - T_a)\big|_\Omega + \varepsilon\sigma\left(T^4 - {T_a}^4\right)\Big|_\Omega - Q_r\big|_\Omega$ (9)

In Equation 9, the RHS represents the net heat flux into the deposited material. The first term on the LHS represents the heat lost to convection, while second is the radiation heat loss and the third is the energy input from the laser.

2.3.1.3 Phase Precipitation Model

The deposited material was considered to be multi-phased with thermal properties that were weighted according to a linear mixture rule. The weighting of the mechanical properties is discussed in Section 2.3.1.4. Volume fractions of phases evolved with changing temperature according to a semi-empirical Koïstinen-Marbürger model in which the phases austenite, ferrite, martensite, and tempered martensite were included. As explained further in the next section, the substrate and deposited material were initially modeled as ferritic before being austenized by the heat source, after which the phase fraction of martensite precipitated after each thermal cycle is given by Equation 10 [31]

$$f_{M_i}(T) = \left(f_{A_i} + f_{A_o}\right)\left[1.0 - \boldsymbol{exp}\left(-k\left(M_s - T_i\right)\right)\right] + f_{M_o} \quad \text{for } T_i \leq M_s \tag{10}$$

while that of retained austenite after each cycle is given by Equation (11)

$$f_{A_i}(T) = f_{A_o}\ \boldsymbol{exp}\left(-k\left(M_s - T_i\right)\right) \quad \text{for } T_i \leq M_s \tag{11}$$

Equations (10) and (11) are applied for all thermal cycles, i.e. every point in the solution domain for each pass of the heat source. Since ferrite was only considered for the initial metallurgical condition, the final state included only retained austenite, martensite, and tempered martensite.

2.3.1.4 Theoretical Thermo-Metallurgical-Mechanical Model

The temperature and metallurgically-dependent mechanical features of the LENS^{TM} process are calculated in SYSWELD® with use of a phenomenologically-based constitutive equation of state model developed by LeBlond [32] to describe the temperature-dependent strain and stress fields that result in processes involving thermally-driven phase transformation. This model partitions the total macroscopic strain field according to Equation 12

$$E^{Total} = E^{E} + E^{P} + E^{Thm} + E^{TRIP} \tag{12}$$

The first three terms on the RHS of Equation 12 describe macroscopic strain fields, while the components of E^{TRIP} are defined as micro-strains.

The elastic strains were considered to be isotropic with separate temperature dependent elastic moduli for each phase present, while simple isotropic strain hardening is chosen to describe the plastic zone. The overall yield strength of the material is determined by a temperature-dependent, nonlinear rule of mixtures shown here as Equation (13)

$$\boldsymbol{\sigma}_y(T) = [1 - F(f_j)]\boldsymbol{\sigma}_y^i(T) + F(f_j)\boldsymbol{\sigma}_y^j(T) \tag{13}$$

The thermo-metallurgical strain is that due to the thermally-activated expansion and contraction of each phase and the volumetric change resulting from phase transformation as described in Equation 14

$$E_{total}^{Thm}(T, f) = \sum_i f_i E_i^{Thm}(T) \tag{14}$$

Transformation-induced-plasticity is microscopic plastic strain resulting from the macroscopic volumetric change included in E^{Thm}. In the case of the LENS ^{TM} material, X20Cr13, the initial ferritic material is melted upon exposure to the heat source so that the TRIP present in the final strain state is related only to austenite/martensite transformations. In the case of such a two phase material, the TRIP occurs in the weaker phase, i.e. austenite for X20Cr13. According to the LeBlond plasticity model [31,32,33], TRIP will contribute to the overall plastic strain if the proper yield conditions are met, i.e. if the equivalent stress ($\sigma_{eq} = \sqrt{\frac{3}{2} S_{ij} S_{ij}}$) is greater than or equal to the combined yield strength defined in Equation 23, then an homogenous classical plastic strain occurs in both phases. However, if $\sigma_{eq} < \sigma_y$, then the total plastic strain tensor receives both a classic macroscopic contribution and one due to TRIP as in Equations 15 and 16.

$$E^P = E^{CP} + E^{TRIP} \tag{15}$$

$$E_{ij}^{TRIP} = -\frac{3}{2}\left(\frac{2\Delta E_{A\to M}^{Thm}}{\boldsymbol{\sigma}_y^A}\right)\boldsymbol{ln}(f_M) S_{ij} h\left(\frac{\boldsymbol{\sigma}_{eq}}{\boldsymbol{\sigma}_y}\right) f_M \tag{16}$$

2.3.1.5 Finite Element Model Development

The same 3-D finite element model presented by Wang *et al.* [20] was used to approximate the experimental build conditions. The geometry consisted of a 5 mm x 1 mm x 10 mm plate, composed of 10 deposited layers 0.5 mm x 1 mm x 10 mm each, and a 1mm x 4 mm x 10 mm substrate. The computational domain along with the applied mesh is shown in Figure 35 below.

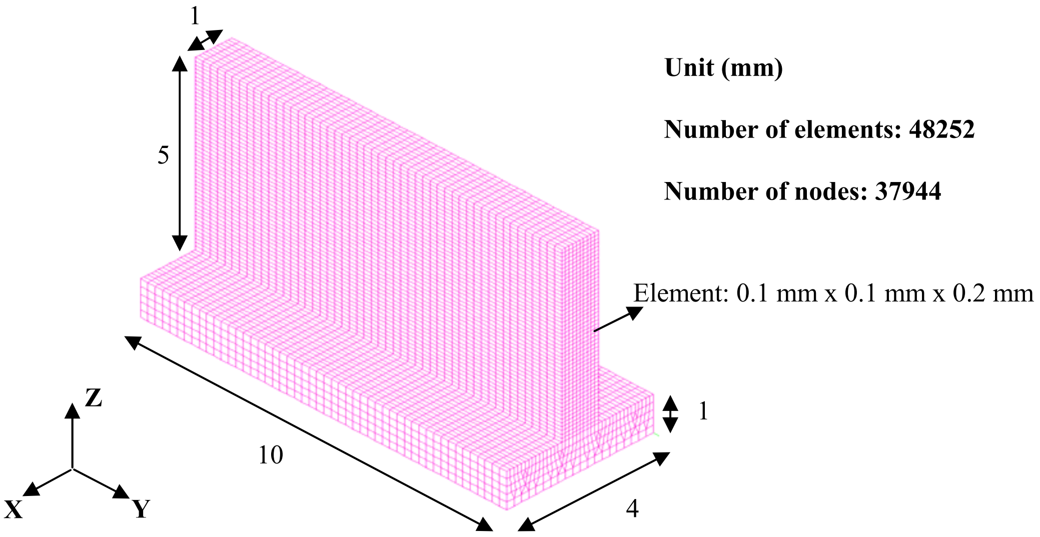

Figure 35. Computational domain used for LENS$^{\text{TM}}$ thin plate thermal analysis.

2.3.1.6 Finite Element Model Implementation

2.3.1.6.1 Thermal Calculations

For each case modeled, an initial temperature of 20 °C was applied over the whole domain, while the bottom surface of the substrate was constrained to remain at 20 °C throughout the process. The convective heat transfer coefficient was specified as $h = 100\ W/m^2 °C$ and the emissivity as $\varepsilon = 0.62$. A SYSWELD® subroutine was used to model the Gaussian-distributed heat input as a moving heat source with a user-specified velocity of 2.5, 4.2, and 8.5 mm/s. The initial beam radius, r_e, used in Equation 7 was set to 0.5mm. Since most manufacturing applications of LENS^{TM} control the applied laser power through a thermal imaging feedback system similar to that presented by Hofmeister *et al.* [8] to maintain near constant molten pool dimensions throughout the build, a sequence of input energy densities, Q_o, was established here for each value of $\frac{dy}{dt}$ studied that would produce the same effect in the modeling. The calculated results at some $\frac{dy}{dt}$ were compared to the measured stress values collected by neutron diffraction for cases in which the average value of Q_o used for all ten layers was close to the constant applied laser power used to build the sample plate. These sequences are shown in Figure 36 below.

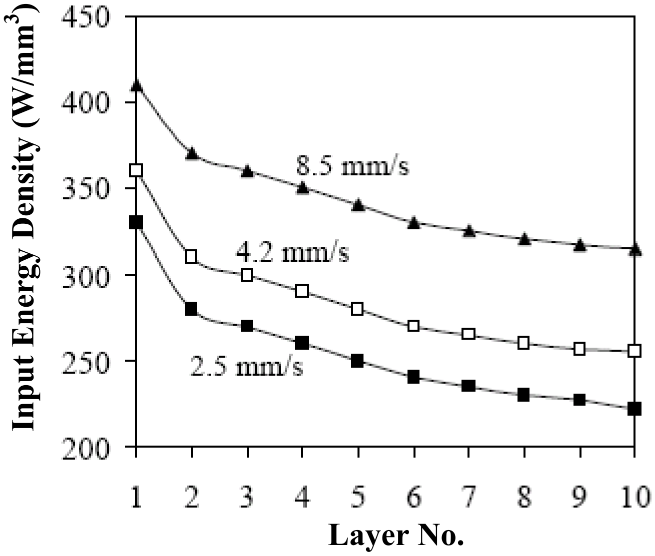

Figure 36. Value of Q_o applied at each deposited layer for $\frac{dy}{dt}$ = 8.5, 4.2, 2.5 mm/s to maintain constant molten pool size.

As Wang *et al.* [21] reported, Figure 36 indicates that higher translation speeds require higher heat inputs to maintain steady molten pool conditions. In order to compare the modeling results with the experimental data, which corresponded to constant input laser powers, the values of Q_o were averaged over Layers 1-10. The average values were approximately 254 W, 285 W, and 344 W for $\frac{dy}{dt}$ = 2.5, 4.2, and 8.5 mm/s, respectively.

The heat source moved in the same direction for each layer and was deactivated between consecutive layer depositions for a specified idle time, Δt, that depended on the velocity of the source. The computational domain was chosen to represent an actual plate 25mm long, the length of several of the samples. Accordingly, the value of the idle time was specified to account for the excluded 15 mm of deposition. This approach is validated by the high cooling rates Wang *et al.* [21] had previously calculated for a fixed location, shown here as Figure 19 and those measured by Wang *et al.* [20] that are shown in Figure 13, which revealed that the heating effects were very much localized.

The properties of the stainless steel alloy X20Cr13, which are provided in the SYSWELD® material database, were applied to both the substrate and deposited material since the chemical composition of this steel, shown in Table 3, is very similar to that of AISI 410.

Table 3. Comparison of chemical compositions for AISI 410 and X20Cr13 stainless steels.

Material	**Chemical Composition**
AISI 410	C=0.15%, 11.5.%≤Cr≤13.0%, Mn=1.0%, Si=1.0%, S=0.03%, P=0.04%
X20Cr13	0.16%≤C≤0.25%, 12.0%≤Cr≤14.0%, Mn≤1.5%, Si≤1.0%, S≤0.03%, P≤0.04%

2.3.1.6.2 Coupled Thermo-Mechanical Calculations

The calculation procedure in SYSWELD®, shown here in Figure 37, involves a strong coupling between thermal and metallurgical processes, where temperature and phase proportions are solved simultaneously through Equations 6, 10 and 11.

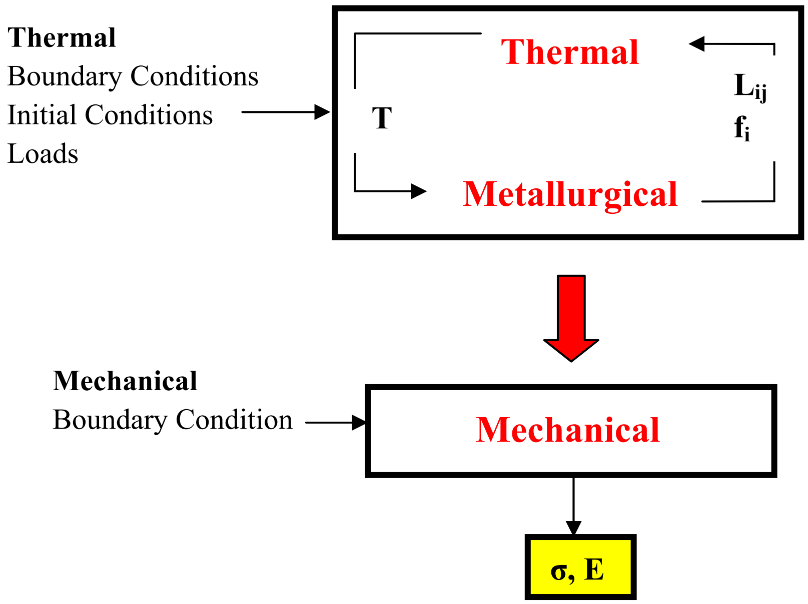

Figure 37. Calculation scheme for thermal, metallurgical, and mechanical analyses in SYSWELD®.

A weak coupling relation is then employed for the mechanical calculations whereby the temperature and metallurgical results are used as input for the model in Section 2.3.1.4.

2.3.1.7 Residual Stress Calculations

To provide comparison with the experimental results, the calculated Z-component of stress, σ_Z, is analyzed. The 3-D distributions of the calculated stress values for $\frac{dy}{dt}$ = 2.5, 4.2, and 8.5 mm/s are shown in Figure 38 for all ten layers.

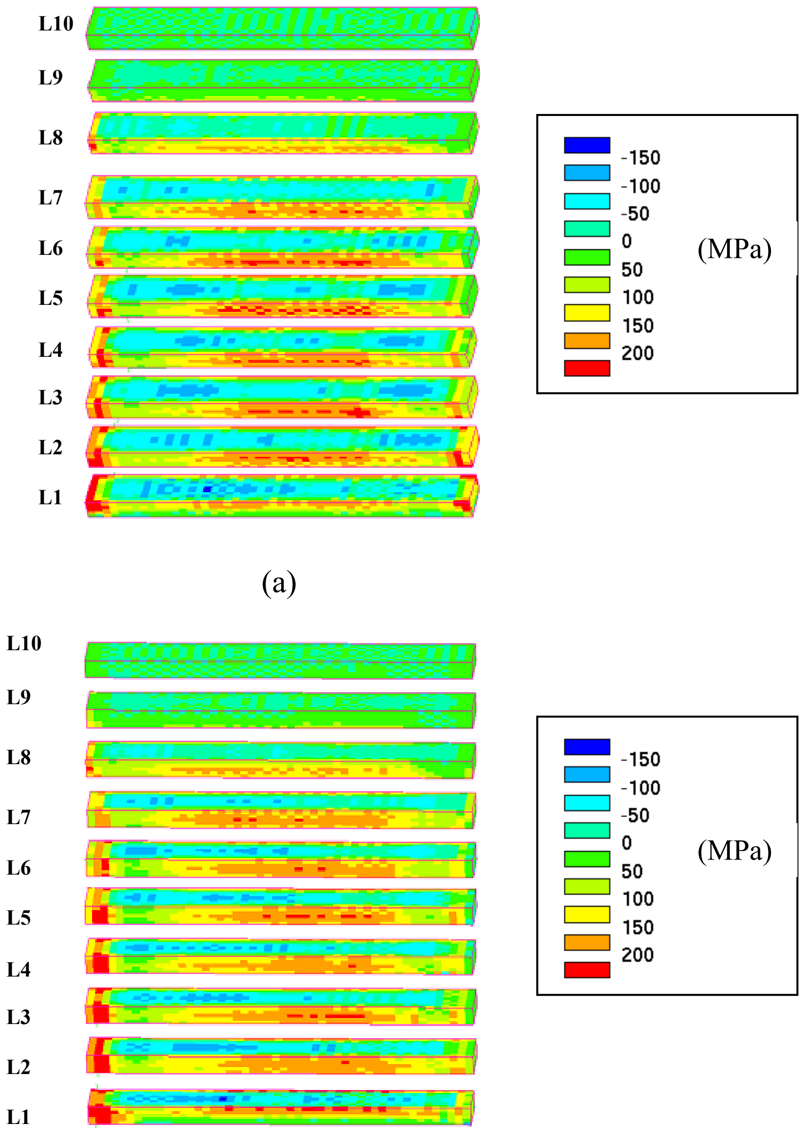

(a)

(b)

Figure 38. Distributions of σ_z (MPa) in completed 10-layer plates for $\frac{dy}{dt}$ = a) 2.5 mm/s, b) 4.2 mm/s, c) 8.5 mm/s.

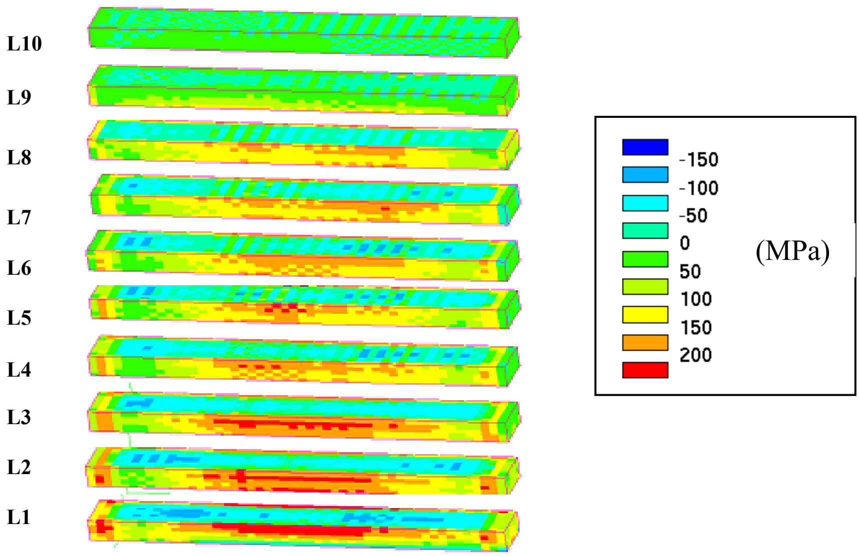

(c)

Figure 38 (Continued).

The contours on Figure 38 appear highly pixilated since an average value is calculated for each element and no smoothing was applied. However, the results clearly show a congregation of tensile stresses at the outer surfaces of the plates and compressive values near the plate centers. Additionally, the top layers, which are close to the free end, show very small or zero values of residual stress. The calculated results compare well in a qualitative manner with the measured distributions shown in Section 2.2.3 and those collected by Rangaswamy, *et al.* [11].

Though little experimental data was available for comparison, the other principal stress components σ_y and σ_x were also included in the calculations for the three values of $\frac{dy}{dt}$. Figure 39 compares the calculated distributions of σ_z and σ_y for Layers 1, 3, 5, 7, and 9 in the direction of stage travel for at all three translation speeds.

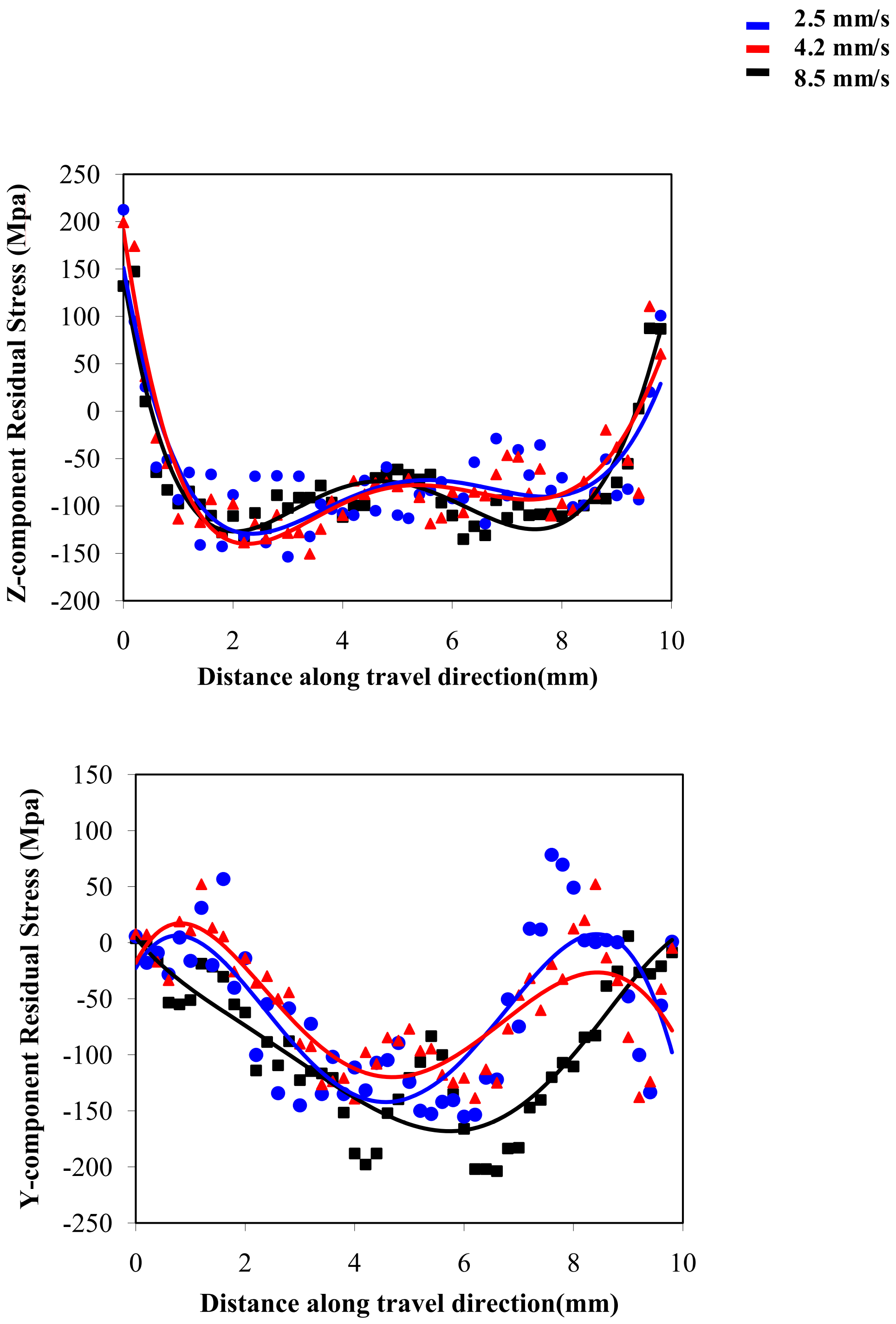

(a)

Figure 39. σ_{Z} and $\boldsymbol{\sigma}_{y}$ along width of plate at all $\frac{dy}{dt}$ in Layers a) 1, b) 3, c) 5, d) 7 and e) 9.

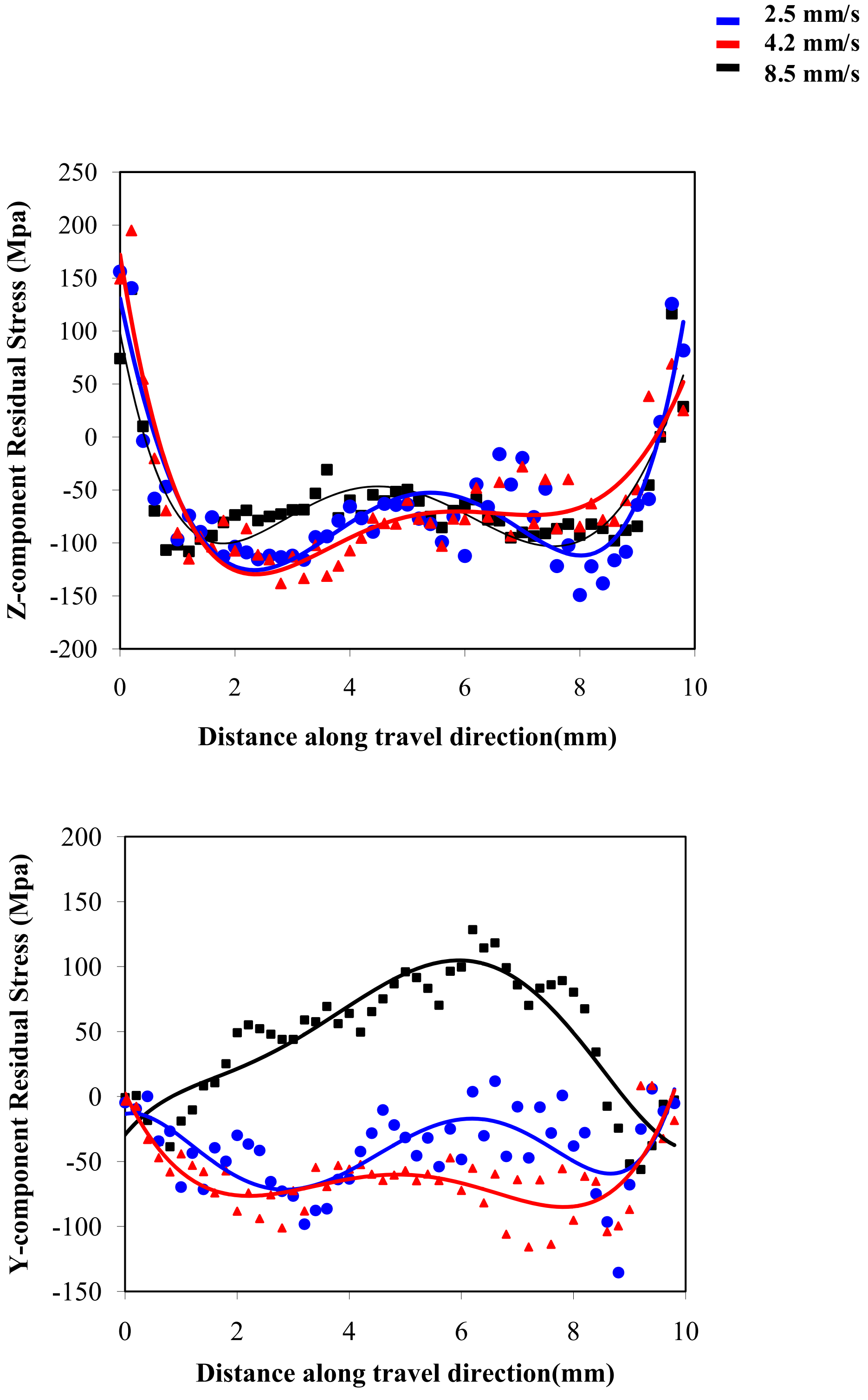

(b)

Figure 39 (Continued).

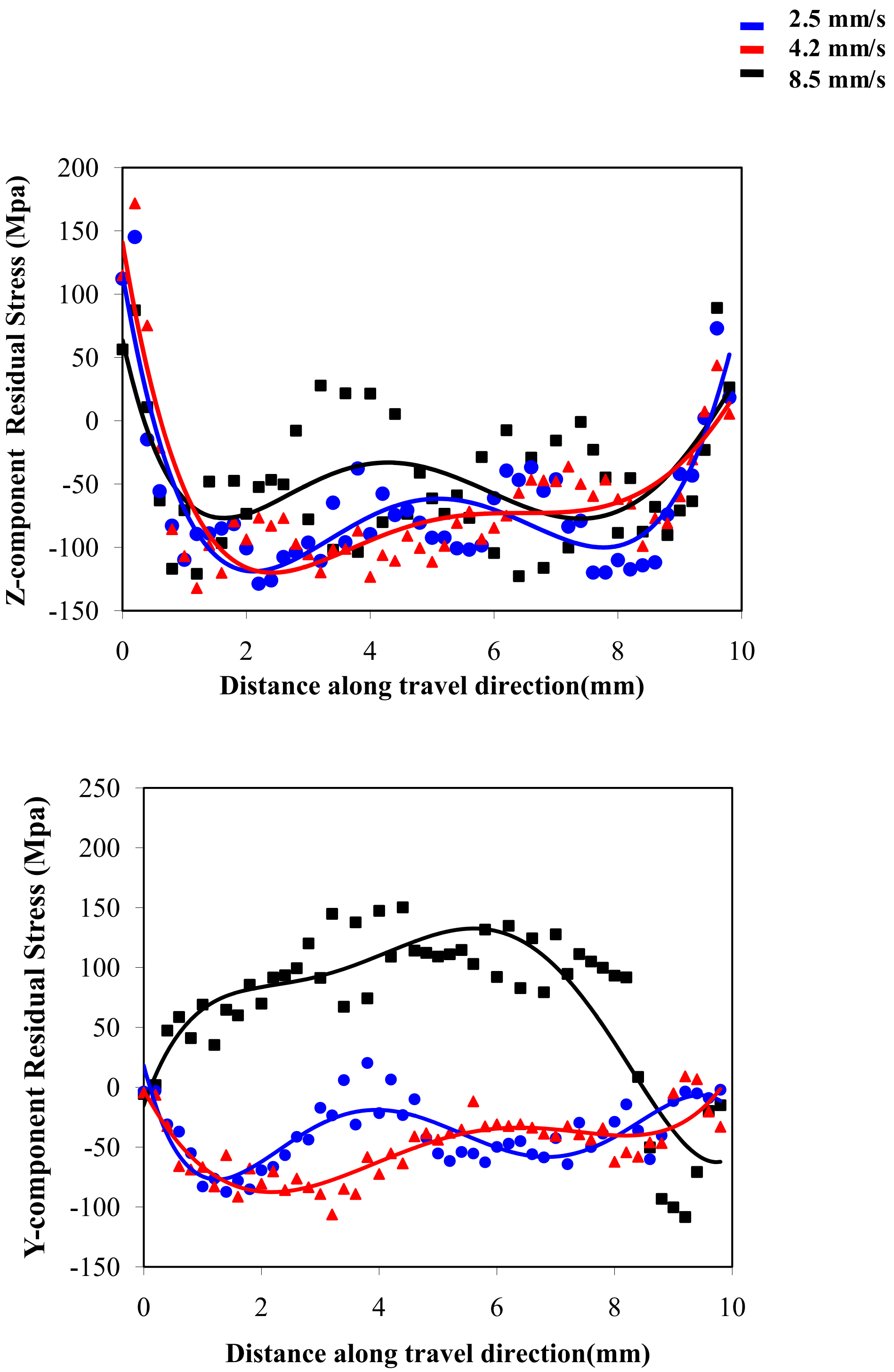

(c)

Figure 39 (Continued).

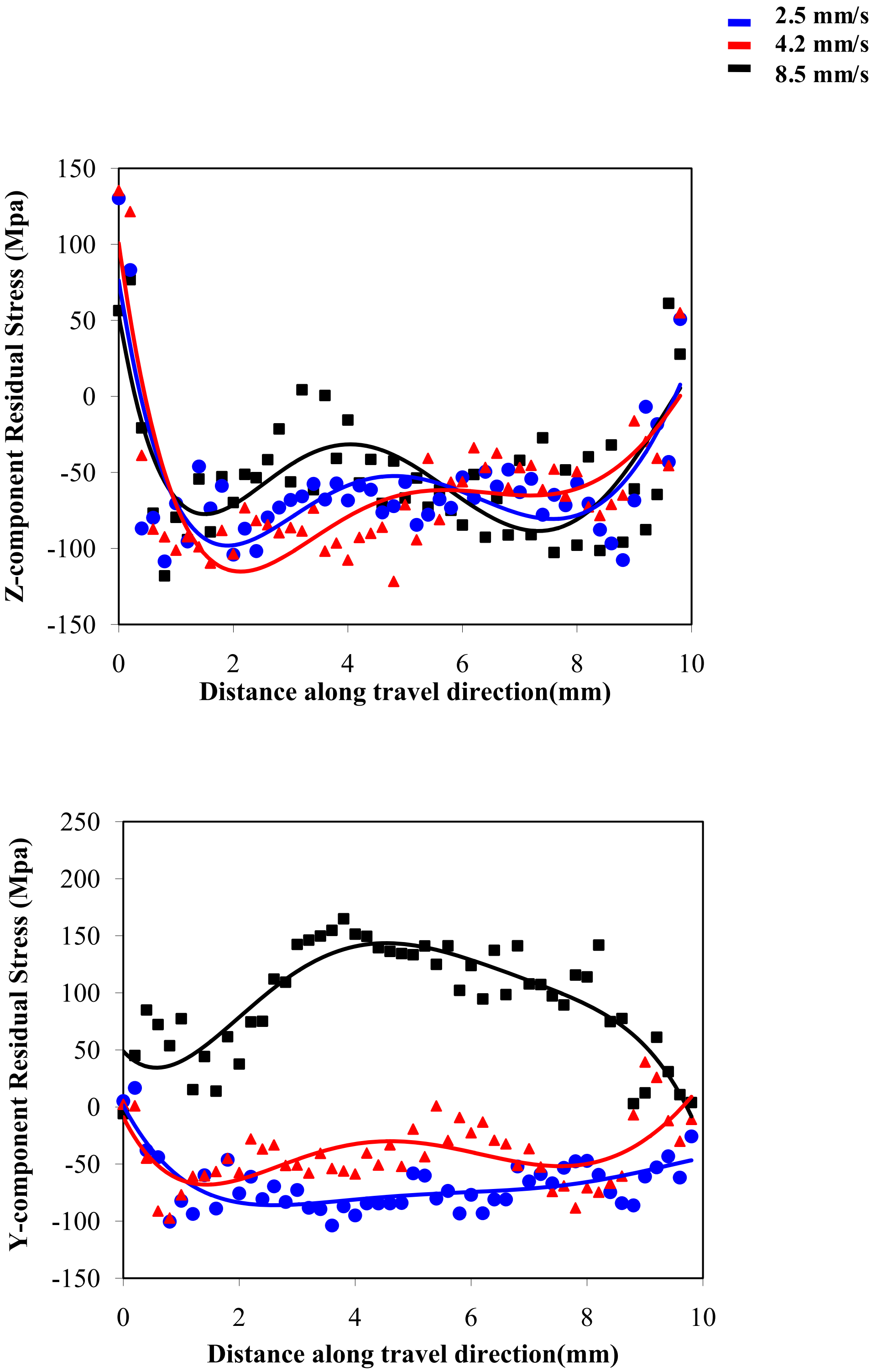

(d)

Figure 39 (Continued).

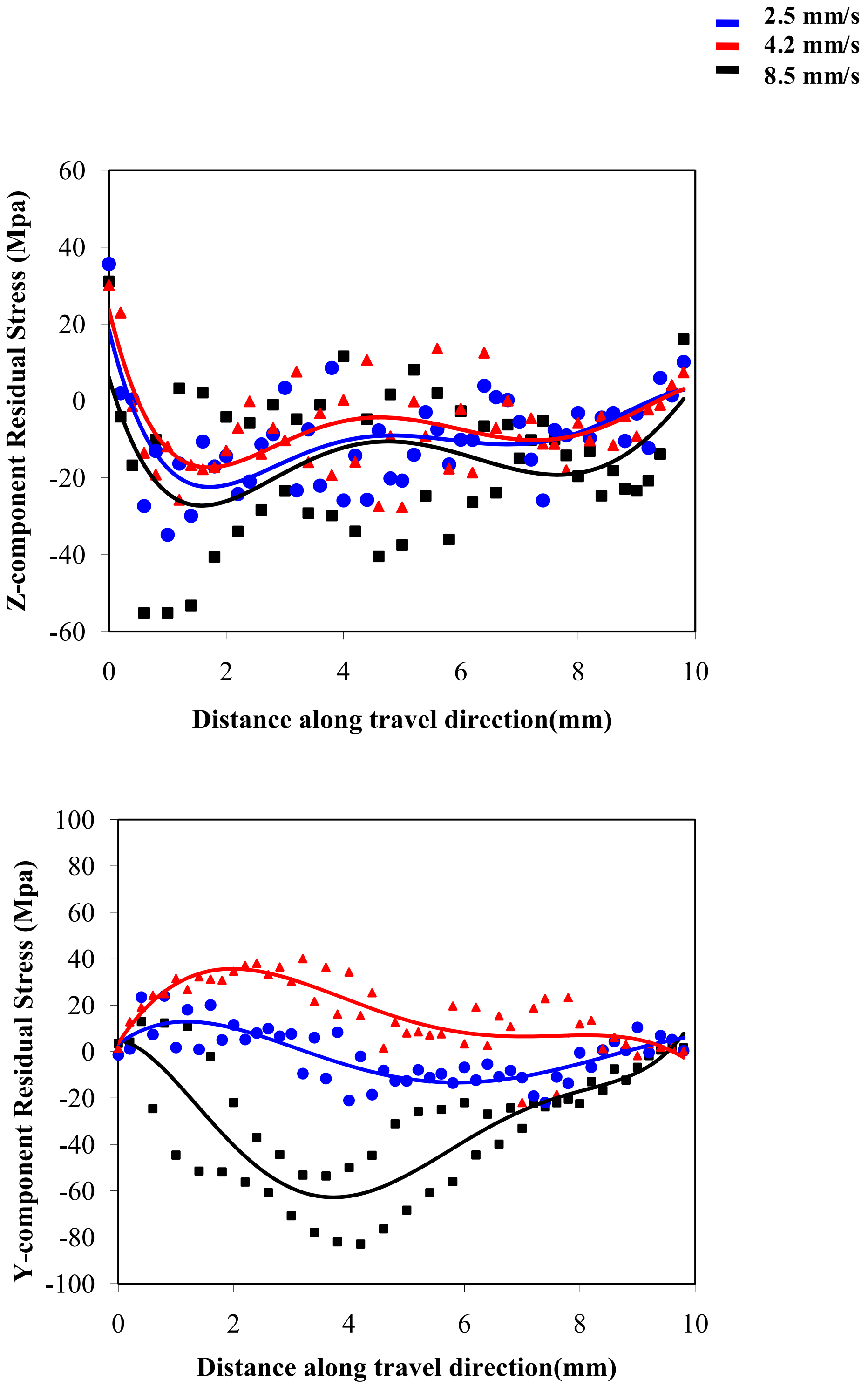

(e)

Figure 39 (Continued).

The solid lines in Figure 39 are the fitted curves for the numerical data points. The plots show that σ_z and $\boldsymbol{\sigma}_y$ are similarly compressive at the two lower speeds, but that $\boldsymbol{\sigma}_y$ becomes tensile at $\frac{dy}{dt} = 8.5$ mm/s in all layers except Layer 9, where the tensile values are instead taken on by σ_z and $\boldsymbol{\sigma}_y$. Wang *et al.* [30] theorized that the tensile nature of $\boldsymbol{\sigma}_y$ at $\frac{dy}{dt} = 8.5$ mm/s is due to the higher cooling rates predicted at higher speeds, as shown in the parametric study in Reference [21]. These rapid cooling rates may prevent relaxation of the internal stresses after the initial deformation.

Interestingly, the results show magnitudes and distributions of $\boldsymbol{\sigma}_y$ similar to those measured for Sample 4 in Section 2.2.3. However, contrary to the measured data in which the values of $\boldsymbol{\sigma}_y$ were significantly less than those of σ_z, the computed results show the two components as being approximately the same size, though no precise comparison can be made, since the combination of laser power and speed used to build Sample 4 was not modeled.

The calculated distributions of σ_z and $\boldsymbol{\sigma}_y$ along the vertical plate centerline for all values of $\frac{dy}{dt}$ are shown in Figure 40. The plots in Figure 40 pertain to Layers 3-10 of the computational domain, which closely approximates the region of the sample plates in which data was collection. The computed σ_z profile is quite similar in a qualitative sense to the measured data, whereby increasing compressivity results with increased depth from the top surface. As in the horizontal direction, $\boldsymbol{\sigma}_y$ becomes tensile at $\frac{dy}{dt}$ = 8.5mm/s.

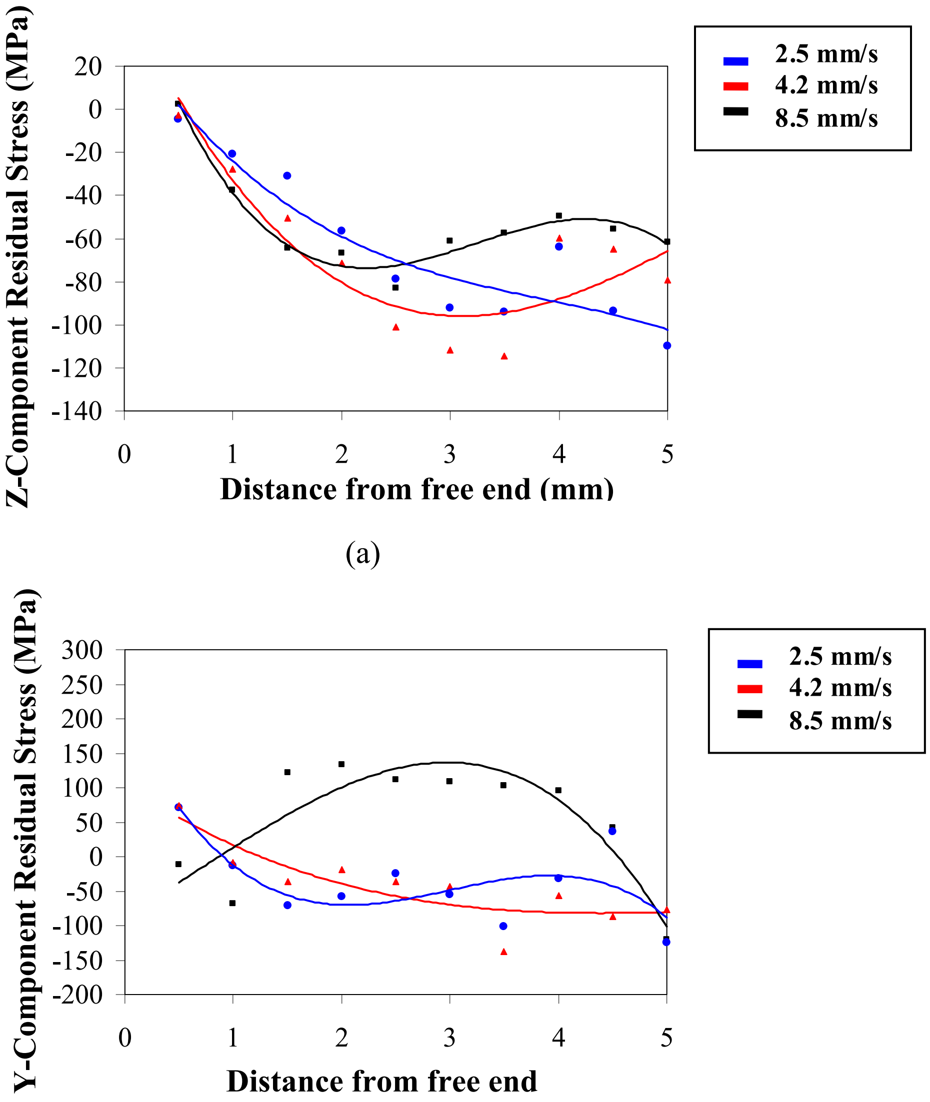

(a)

(b)

Figure 40. Distribution of a) $\boldsymbol{\sigma}_z$ and b) $\boldsymbol{\sigma}_y$ along vertical center line for all $\frac{dy}{dt}$.

A direct comparison between the experimental and modeling results is difficult due to the constant versus variable heat inputs used for the actual builds and simulated builds, respectively. An additional complication arises from the reduced dimensions of the computational domain in relation to the sample plate geometries. Accordingly, a qualitative evaluation is made amongst the experimental and modeling results with same $\frac{dy}{dt}$. To account for the geometrical differences, the experimental and calculated distributions of σ_Z are compared in a region from the top layer to a depth of 5mm along the vertical plate centerline. For the horizontal distributions, values of σ_Z are examined in a region extending 5mm in the Y-direction from either side of the vertical centerline. The modeling results were taken along Layer 5, which corresponded to the horizontal centerline of the computational domain. The experimental and modeling results for $\frac{dy}{dt} = 2.5$mm/s are shown in Figure 41.

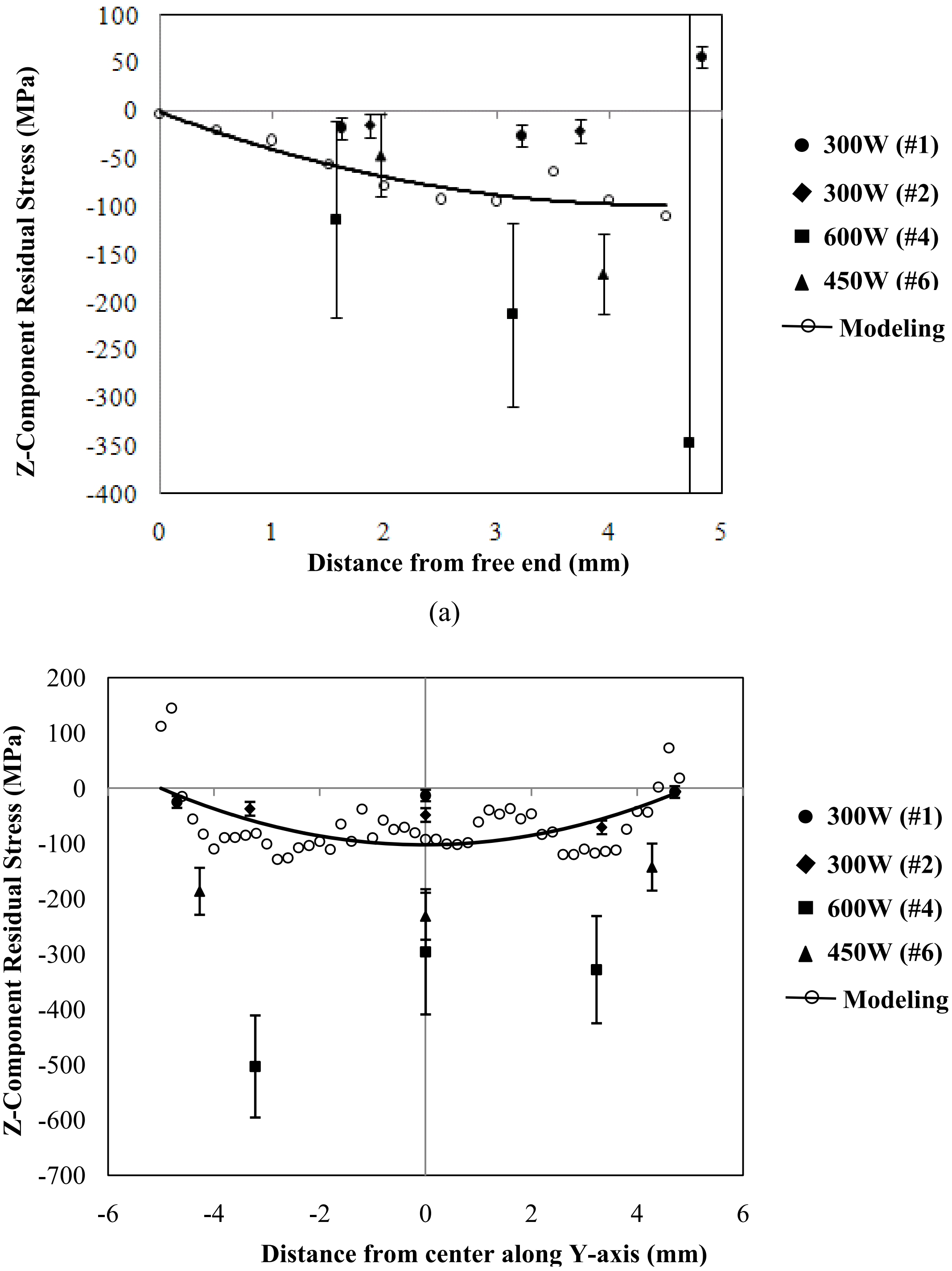

(a)

(b)

Figure 41. Experimental and computational σ_y distributions for $\frac{dy}{dt}$ =2.5 mm/s along a) vertical plate axis and b) along width from vertical centerline.

The plot in Figure 41(a) shows that the modeling results, which correspond to an average energy input density of 254 W/mm^3, follow the same general trend of increasingly compressive stress with the distance from the free end as the measured distributions. The calculated results presented in Figure 41(b) are closest to those measured values associated with an input laser power of 300 W.

A comparison between the experimental and computational distributions of $\boldsymbol{\sigma}_z$ at a translation speed of 4.2 mm/s is shown in Figure 42. As in Figure 41, the plots in Figure 42 show that the calculated values lie within the range of the experimental data, for which the measured values of $\boldsymbol{\sigma}_z$ were close for all samples at these locations. Since no diffraction measurements were performed on plates produced with $\frac{dy}{dt} = 8.5$ mm/s, no experimental comparison could be performed for with those calculations.

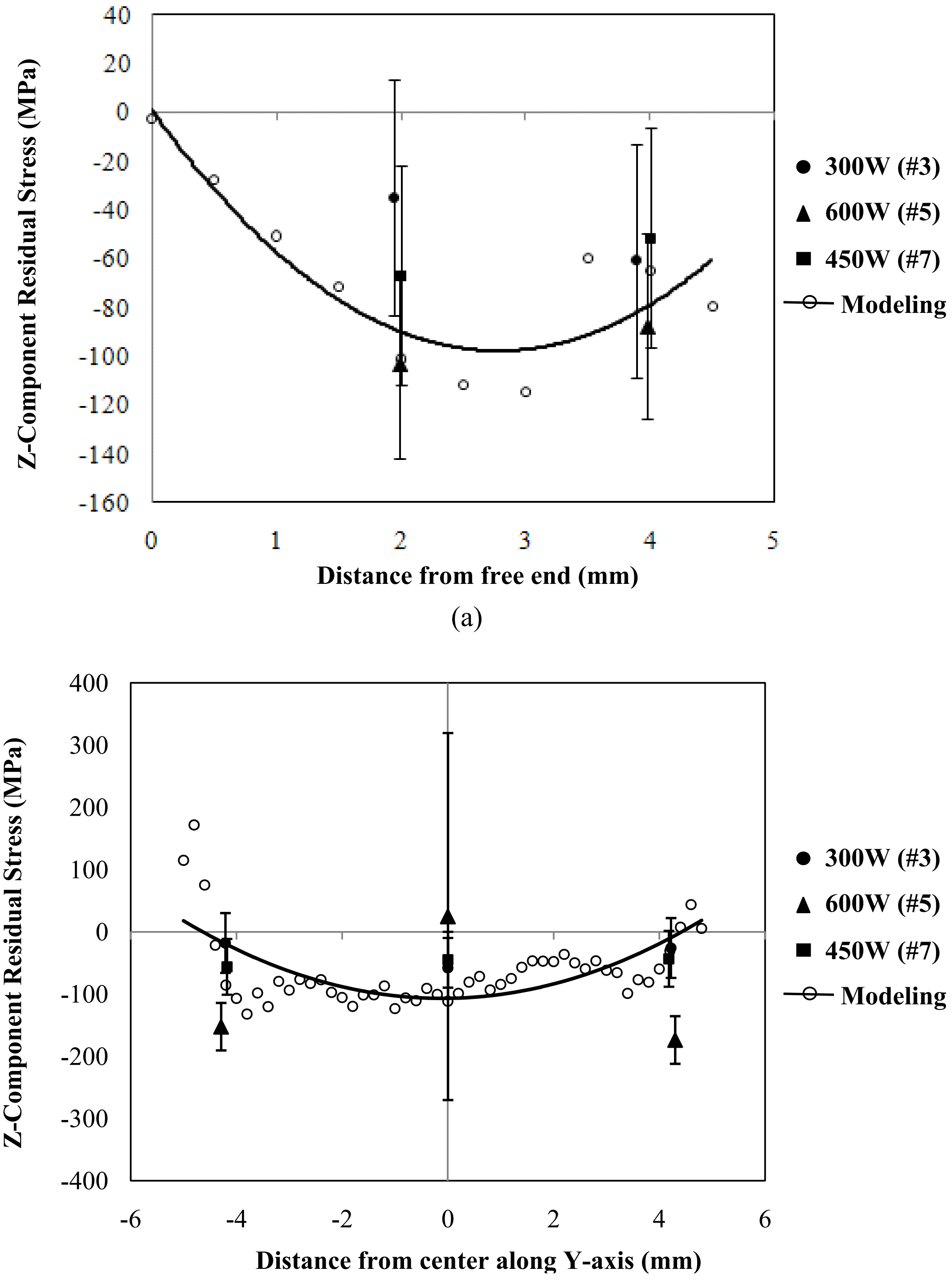

(a)

(b)

Figure 42. Experimental and computational σ_z distributions for $\frac{dy}{dt} = 4.2$ mm/s along a) vertical plate axis and b) along width from vertical centerline.

2.3.1.8 Conclusions

The comparison of the measured and modeled results in Figure 41 shows the calculated distributions of $\boldsymbol{\sigma}_z$, with average heat inputs of $Q_o = 254$ W/mm^3, aligning most closely with the sample plates built with 300 W laser power, indicating that the FE model is able to capture this parametric relation for a given speed. At $\frac{dy}{dt} = 4.2$ mm/s, the relationship between $\boldsymbol{\sigma}_z$ and input laser power is not as clear in the regions examined. However, the calculated results reside within the limits set by the measured data.

The comparisons presented in Figures 41 and 42 for $\boldsymbol{\sigma}_z$ show that the calculations made with SYSWELD® can provide reasonable approximations of the measured data for different values of $\frac{dy}{dt}$. Additionally, the numerical values of $\boldsymbol{\sigma}_y$ were similar to those observed in one of the sample plates. However, additional experimental samples produced under more combinations of input parameters and further simulations would be needed to ascertain whether the model is truly able to predict residual stresses for a wide range of values for $\frac{dy}{dt}$ and P_L.

2.3.2 Modeling with ABAQUS®

2.3.2.1 Introduction

The previously presented modeling results produced using SYSWELD® have shown that this FE package is capable of giving reasonably accurate predictions of residual stresses generated during the LENS™ process in multi-phase steel alloy. However, the LeBlond constitutive model used by SYSWELD® to predict the stress state is an equation of state model based in part on external observations and excludes several important physically-grounded aspects of deformation. Though this type of model is reasonably accurate within the elastic limit, it cannot properly account for the dissipative effects that take place in inelastic materials. An internal state variable (ISV) type model, which is characterized by the use of rate equations to track the evolution of unobservable, macroscopic state variables, is better suited for describing irreversible processes and is a more appropriate choice for modeling the complexities of LENS™. One such model was developed by D. Bammann at Sandia National Laboratory and, in conjunction with M. Chiesa and G. Johnson [34] and was incorporated into a computational formulation widely known as the BCJ plasticity code. This code has been used to model complex thermo-mechanical processes, such as welding and heat treating for single-phase materials by Dike *et al* [35] and Bammann *et al.* [36]. The theoretical model was expanded by Bammann *et al.* [37] to describe a two-phase material that undergoes austenite/martensite transformation through a kinetic model developed by Oddy *et al.* [38].

The two-phase model can be implemented in ABAQUS® via the BCJ code as a user defined material subroutine or UMAT. Though such a subroutine has been developed that incorporates a two phase version of the BCJ code, to date no calculations have been performed as the material input parameters needed for the model are not currently available for either X20Cr13 or AISI 410 stainless steels in the literature. However, when these parameters are recorded or when experimental data is measured for

LENS™ deposition of some material for which parameters already exist, the model can be implemented through ABAQUS® and compared to measured values.

A prerequisite to thermo-mechanical LENS^{TM} modeling in ABAQUS® is the ability to accurately predict the thermal conditions generated during the deposition that would subsequently drive microstructural transformations and thermally-initiated deformation. Accordingly, ABAQUS® 6.7 was used to model the thermal characteristics of the LENS™ deposition of a 10-layer thin plate to validate that this FEA package is capable of accurately predicting the thermal histories. The calculated temperature distributions were then compared to experimentally measured data from Hofmeister *et al.* [6] and also to modeling results produced with SYSWELD® by Wang *et al.* [21]. Additionally, simulations for 10-layer thin plate deposition were made with the ABAQUS® for different values of $\frac{dy}{dt}$. The resulting molten pool sizes were measured and compared to those found using SYSWELD® by Wang *et al.* [30], which were validated experimentally in that study.

2.3.2.2 Theoretical Thermal Model

The mathematical thermal model used for the ABAQUS® calculations are essentially the same as those in the SYSWELD® model except for simplification, the material is modeled as single-phased, where each thermal property (ρ, k, c_p, and L) is calculated as a temperature-dependent average of those for the included phases. Accordingly, phase transformation is not accounted for in the thermal calculations, i.e. no temperature-dependent weighting scheme is used. The resultant governing equation is presented here as Equation 27.

$$\overline{\rho}(T)\overline{c}_p(T)\frac{\partial T}{\partial t} - \nabla\left(\overline{k}(T)\nabla T\right) + \overline{L}(T)\frac{\partial}{\partial t}\left(\frac{T - T_s}{T_l - T_s}\right) = 0 \tag{27}$$

The applied boundary conditions thermal loads are the same as those given as Equations 7-9 in Section 2.3.1.2.

2.3.2.3 Finite Element Model

The computational domain used for the ABAQUS® modeling was given the same dimensions previously presented in Section 2.3.1.4. The mesh was composed of linear, 8-noded DC3D8 heat transfer brick elements. The details of the mesh geometry are shown in Figure 43.

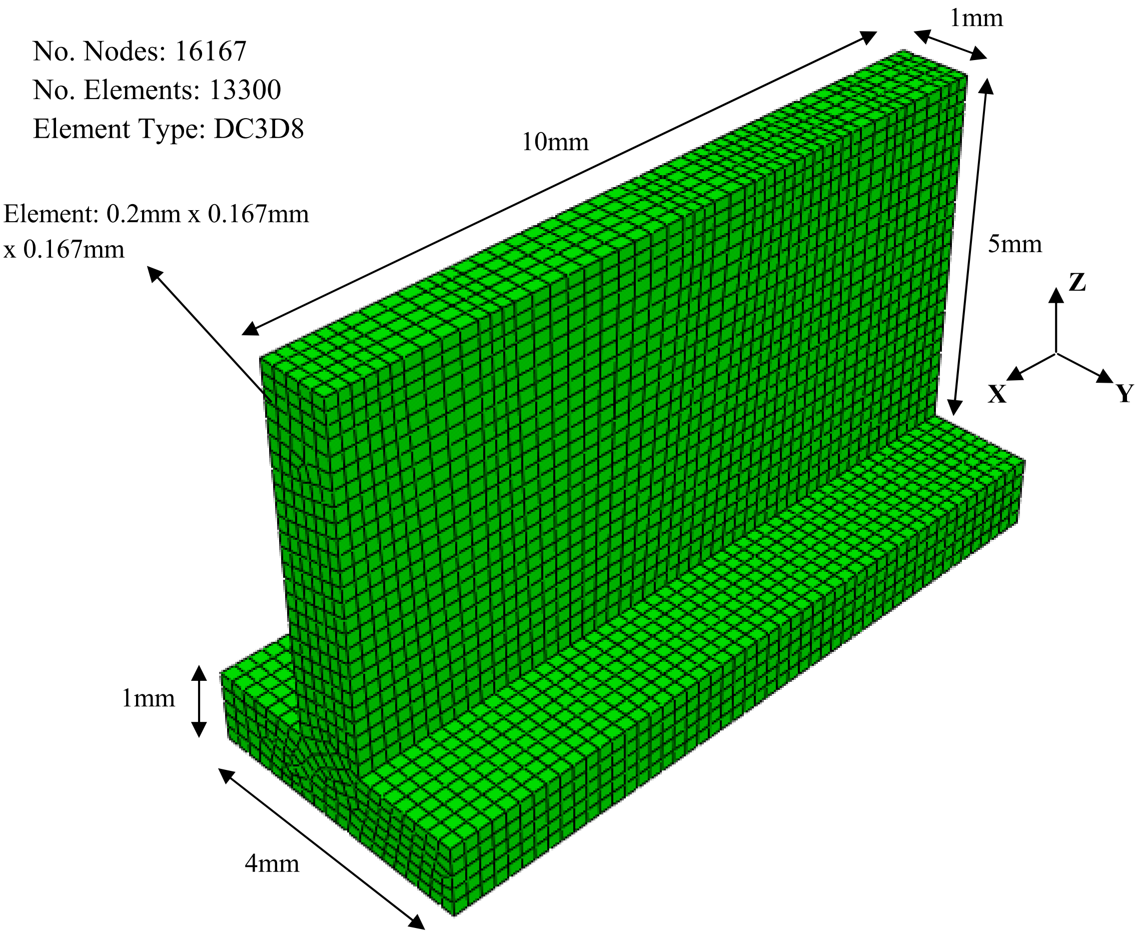

Figure 43. Computational mesh for 10-layer LENS™ thin plate in ABAQUS®.

The mesh created in ABAQUS® is not as fine as that used for the SYSWELD® calculations. The appropriate degree of refinement was determined by first modeling the thermal process with a coarse mesh of 1197 nodes and 1184 elements to obtain a temperature field. The mesh refinement was then doubled and a subsequent simulation performed. The new temperature field was compared to the previous results to determine whether the solution was mesh-dependent. This procedure was repeated until the deviation in field values between consecutive meshes was acceptably small, indicating mesh-independency.

2.3.2.4 Model Implementation

The heat transfer analysis performed in ABAQUS® is an un-coupled thermal calculation in which the temperature field is solved for conditions of solid-body conduction, basic convection and radiation heat transfer, as well as latent heat generation. The thermal loading of the plate is modeled as a transient temperature analysis with a semi-automatic time incrementation scheme, in which an upper limit is placed on the length of the time increments by a user-specified maximum temperature change [39].

The deposition process is modeled with the same element activation function used by Neela and De[16] and Deus and Mazumder[17], which is defined as the *MODEL_CHANGE* feature in ABAQUS® 6.7. For these calculations, each layer was composed of ten 0.5 x 1.0 x 1.0 mm^3 element sets, containing 60 elements. A new element set was activated at the beginning of a user-defined time step, entering the active domain with an artificially low value of thermal conductivity that was ramped up to the specified values of X20Cr13 to ensure a smooth transition [39]. Upon entering the active domain, the new element set was loaded with a stationary heat source, Q_r from Equation 7, which was applied for the length of the time step. A total of 100 time steps was used to model the deposition of the plate, where every time step corresponded to the activation and heating of an element set. During each time step the coordinates of the heat source were set to coincide with the center of the newly activated element set. For simplicity, this approach was used to approximate the moving laser instead of using a user-defined subroutine. The length of the time step, i.e. the element set activation rate, depended on the translation speed being examined as seen in Equation 28.

$$dt = \frac{L_e}{\frac{dy}{dt}} \tag{28}$$

Additionally, the same idle times described in Section *2.3.1.5.1* are again used between consecutive layers to account for geometric differences between the computational domain and a 25 mm long plate.

2.3.2.5 Thermal Calculations

Hofmeister *et al.* [6] produced a thin plate of AISI 316 stainless steel was deposited by LENS^{TM} using P_L=275 W and $\frac{dy}{dt}$=7.62 mm/s. During the deposition of one of the layers, thermal imaging was used to capture the temperature distribution with distance from the center of the molten pool in the direction opposite to heat source travel when the laser was located at the mid-width of the deposited plate. The plotted distribution is shown here as Figure 3 in Section 1.2.1. These measured values were compared by Wang *et al.* [21] to a calculated temperature distribution for a simulated plate using SYSWELD® under the same processing conditions. The modeling results were shown to closely approximate the actual temperature field, and this comparison was presented as a validation of the FE model [21].

Similarly, this deposition was modeled in ABAQUS® to gauge the accuracy of the model presented in Section 2.3.2.3. Applying single phase thermal properties of AISI 316 to the elements and the same load and boundary conditions specified by Wang *et al.* [21], the temperature field was calculated with the heat source located at the mid-width of the domain for the 10th deposited layer. The resulting temperature distribution was plotted as a function of distance from the center of the molten pool in the direction opposite to deposition and compared to both the measured values and those found with SYSWELD®. This comparison is shown here as Figure 44. The plots in Figure 44 show the calculations made with ABAQUS® are in good agreement with the experimental data as well as the SYSWELD® predictions, though in both instances, the modeling under-predicts the temperature in the region from 1 mm-4mm from the molten pool center, which may indicate that the specified convective and radiation boundary conditions need to be adjusted.

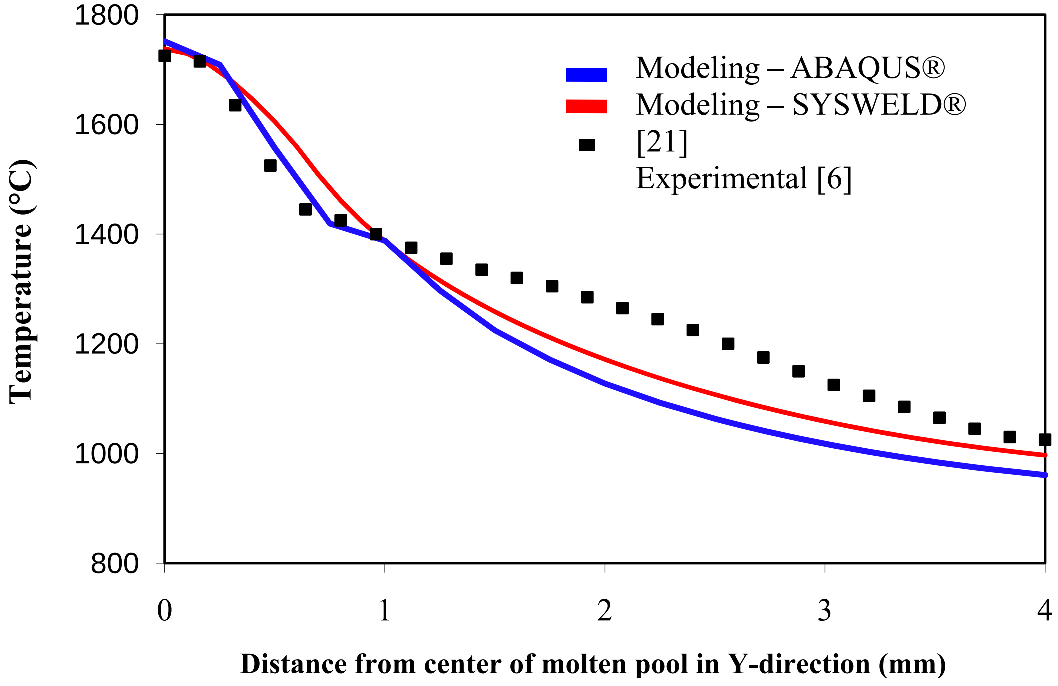

Figure 44. Comparison of numerical and experimental temperatures measured from center of molten pool in top layer of LENS™ AISI 316.

In order to further validate the ability of the model presented Section 2.3.2.3 to accurately predict thermal LENS^{TM} conditions, calculations were performed for the LENS^{TM} deposition of a ten layer plate of X20Cr13 stainless steel at values of $\frac{dy}{dt} = 4.2$ mm/s, and 8.5 mm/s using the same thermal boundary conditions and sequences of Q_o shown in Section *2.3.1.6.1*, Figure 36. The same idle time between consecutive layer depositions was also imposed. The resulting molten pool dimensions in each layer were then compared to the corresponding SYSWELD® predictions, which were experimentally verified by Wang *et al.* [20].

In the calculations X20Cr13 was considered as a two-phase material composed of martensite and austenite, the thermal properties of which were obtained for each phase from the SYSWELD® material database. Each thermal property (ρ, k, c_p, and L) was calculated as a temperature-dependent average of those given for the two phases over a range of 20°C to 1530°C, i.e. from room temperature to the liquidus of X20Cr13.

2.3.2.6 Results and Comparison with SYSWELD®

The resulting molten pool widths (Y-direction) are shown in Figure 45 for each layer when the heat source is located at the plate center. The corresponding SYSWELD® predictions are also shown for comparison. The shapes of the pools appear quite different due to the differing techniques used for simulating the material deposition. Specifically, the SYSYWELD® "dummy element" operation activates entire layers, while the *MODEL_CHANGE* operation in ABAQUS® allows user-defined element sets to be activated individually during the deposition of a layer. The maximum pool size observed at the center of the plates for all ten layers is displayed in Figure 45.

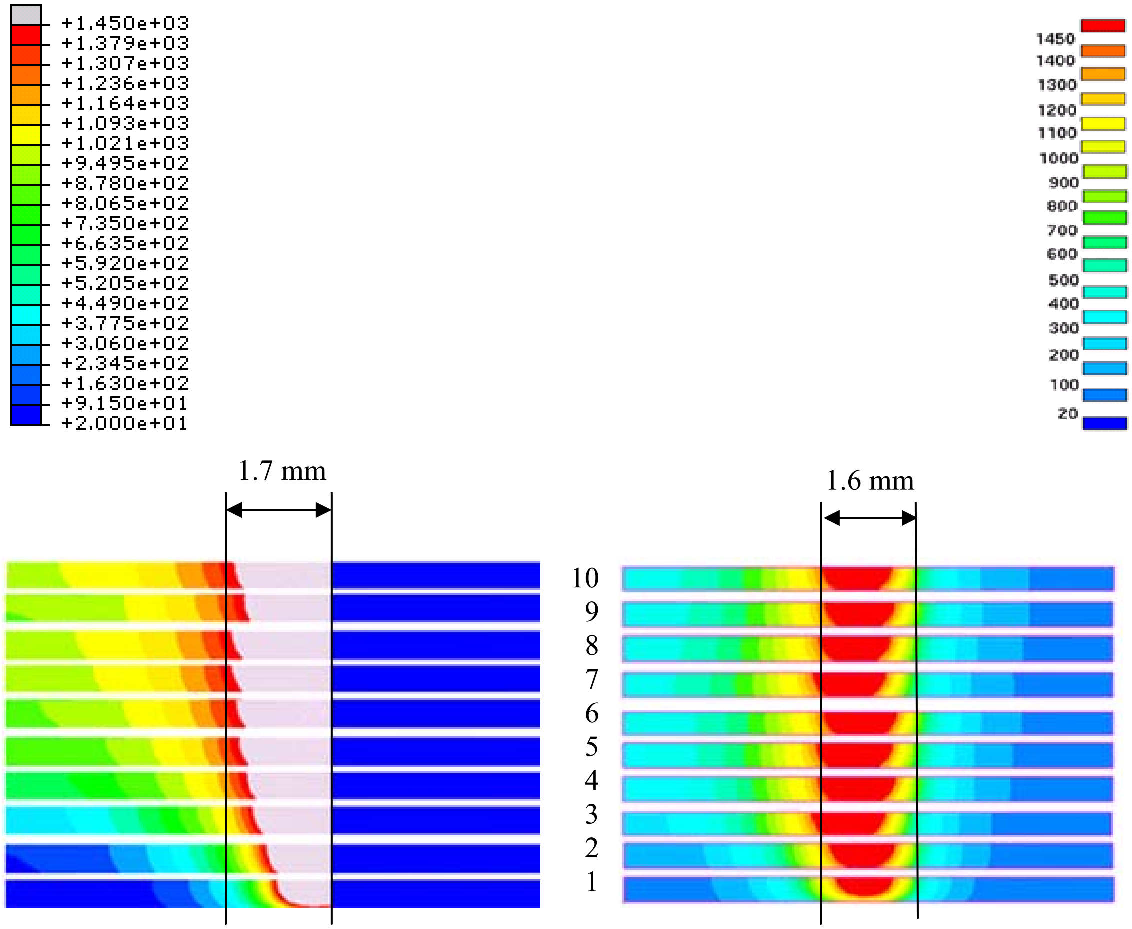

(a)

Figure 45. Comparison of molten pool sizes calculated with ABAQUS® and SYSWELD® for $\frac{dy}{dt}$ = a) 4.2 mm/s and b) 8.5 mm/s.

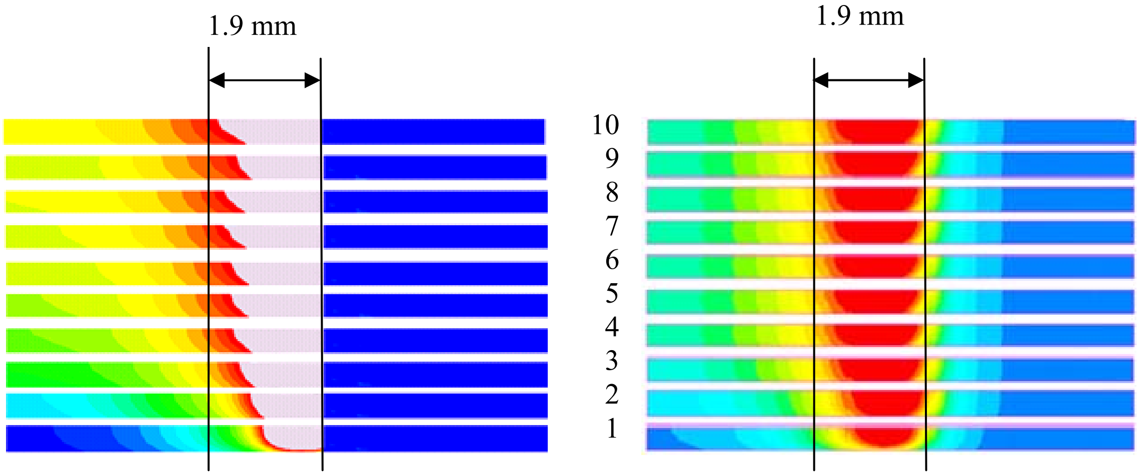

(b)

Figure 45 (Continued).

The ABAQUS® results show more growth of the molten pool from layer to layer, which may be due to the exclusion of phase transformation from these calculations. However, despite the variations in approach, reasonable agreement is found between the two models. Accordingly, Figures 45 shows that essentially the same thermal histories can be generated in the computational domain when the same process parameters are applied.

CHAPTER 3

CONCLUSION

The LENS™ process is a laser deposition technique that is able to economically repair and fabricate metallic components of various geometries, but the relation between final form mechanical properties and the process parameters are not well understood. A thorough review of the published literature on parametric research of LENS™ has been performed here and the major findings reported. A study was then presented in which the finite element method was used to model the thermal, metallurgical, and mechanic features in the deposition of a single-pass, stainless steel plate built with different values of the input parameters, stage translation speed and laser power. Calculations were first performed with the finite element software, SYSWELD®. The residual stress state resulting from each simulation was compared to measured values collected via the neutron diffraction method. The modeling was found to provide reasonably accurate predictions. Further thermal calculations were performed using the finite element software ABAQUS® 6.7 to predict temperature fields and molten pool sizes in the same stainless steel plate with the same process parameter combinations previously used. The calculated temperature profiles closely matched those found with SYSWELD®, which had already been validated through experimental comparison. Accordingly, the ability of ABAQUS® to provide accurate thermal output was qualified, so that a two-phase version of the BCJ internal state variable plasticity model could be applied to modeling residual stresses in LENS™ and implemented via an ABAQUS® user-defined subroutine.

Future efforts to model the effects of process parameters on resulting LENS^{TM} deposits of multi-phase ferrous alloys may make use of the model presented in Section 2.3.2 and the two-phase ISV model developed by Bammann *et al.* [37] in a coupled thermo-metallurgical-mechanical analysis if mechanical testing is performed to obtain the appropriate material properties of X20Cr13 stainless steel or AISI 410 stainless steel as inputs for the ABAQUS® user-defined material subroutine. These material properties and their significance in terms of material behavior have been described by Bammann et al. [36]. Residual stress magnitudes and distributions obtained using this model may then be compared to the experimental measurements and the SYSWELD® predictions presented in section 2.3.1 to determine if the ISV is truly capable of more accurately representing the thermo-metallurgical-mechanical characteristics of the LENS^{TM} process.

BIBLIOGRAPHY

[1] Vilar, R. J. Laser Cladding. Laser Appl. Vol 11. No 2. 1999. Pp. 64-79.

[2] Atwood, C., Griffith, M., Harwell, D., Reckaway, D., Ensz, M., Keicher, D., Schlienger, M., Romero, M., Oliver, M., Jeanette, F., Smugeresky, J. Laser Spray Fabrication for Net-Shape Rapid Product Realization LDRD. Sandia Report.1999.

[3] Sandia National Laboratories website. (http://www.sandia.gov/mst/technologies/net-shaping.html).

[4] Griffith, M., Ensz, M., Puskar, J., Robino, C., Brooks, J., Philliber, J., Smurgeresky, J., Hofmeister, W. Understanding the microstructures and properties of components fabricated by laser engineered net shaping(LENS). Mat. Res. Soc. Symp. Proc. Vol 625. Warrendale, PA. 2000. Pp. 9-21.

[5] Keicher, D. Jellison, J., Schanwald, L., Romero, J. Towards a reliable laser spray powder deposition system through process characterization. 27th Int. Tech. Conf. Soc. Adv. Mat. Pro. Eng. Alburquerque, NM. 1995. Pp. 1009-1018.

[6] Hofmeister, W., Wert, M., Smurgeresky, J., Philliber, J., Griffith M., Ensz, M. Investigating solidification with the laser-engineering net shaping (LENS™) process. JOM-e. http://www.tms.org/pubs/journals/JOM/9907/Hofmeister/Hofmeister-9907.html. Accessed Aug 2007.

[7] Hofmeister, W., Griffith, M., Ensz, M., Smurgeresky, J. Solidification in direct metal deposition by LENS processing. JOM. Vol.53. No 9. 2001. Pp. 30-34.

[8] Hofmeister, W., MacCalum, D., Knorovsky, G. Video monitoring and control of the LENS process. American Welding Society 9th International Conference of Computer Technology in Welding. Detroit, MI. 1998. Pp. 187–196.

[9] Smugeresky, J., Keicher, D., Romero, J., Griffith, M., Harwell, L. Laser engineered net shaping (LENS^{TM}) process: optimization of surface finish and microstructural properties Proc. of the World Congress on Powder Metallurgy and Particulate Materials. Princeton, NJ. 1997. Part 21.

[10] Kahlen, F.-J., Kar, A. J. Tensile strengths for laser-fabricated parts and similarity parameters for rapid manufacturing. Manuf. Sci. Eng. Vol 123. No 1. 2001. Pp. 38-44.

[11] Rangaswamy, P., Holden, T., Rogge, R., Griffith, L. J. Residual stresses in components formed by the laser-engineered net shaping (LENS®) process. Strain Analysis. Vol 38. No 6. 2003. Pp. 519-528.

[12] Rangaswamy, P. Griffith, M., Prime, M., Holden, T., Rogge, R., Edwards, J., Sebring, R. Residual stresses in LENS® components using neutron diffraction and contour method.Mat. Sci. Eng. A. Vol 399. 2005. Pp. 72-83.

[13] Riqing, Y., Smugeresky, J., Zheng, B., Zhou, Y., Lavernia, E. Numerical modeling of the thermal behavior during the LENS® process. Mat. Sci. Eng. A. Vol 428. 2006. Pp. 47-53.

[14] Lindgren, L.-E. Finite element modeling and simulation of welding part : increased complexity. Journal of Thermal Stresses. Vol 24. 2001. Pp. 195-231.

[15] Wang, L., Felicelli, S. Analysis of thermal phenomena in LENS™ deposition. Mater. Sci. Eng. A. Vol 435-436. 2006. Pp. 625-631.

[16] Neela, V., De, A. Numerical modeling of LENS™ process using special element features.2007 Abaqus India Regional Users' Meeting. 2007. http://www.simulia.com.

[17] Deus, A., Mazumder, J. Two-dimensional thermo-mechanical finite element model for laser cladding. Proc. ICALEO. Duley, W., Shibata, K., Poprawe, R., eds. Orlando, FL. Laser Institute of America. 1996. Pp. B/174-B/183.

[18] Labudovic, M., Hu, D., Kovacevic, R. A three dimensional model for direct laser metal powder deposition and rapid prototyping.J. Mat. Sci. Vol 38. 2003. Pp. 35-49.

[19] Costa, L., Vilar, R., Reti, T., Deus, A. Rapid tooling by laser deposition : process simulation using finite element analysis Act. Mat. Vol 53. 2005. Pp. 3987-3999.

[20] Wang, L., Felicelli, S., Craig, J. Thermal modeling and experimental validation in the LENS^{TM} process. 18th Solid Freeform Fabrication Symposium. Austin, TX. Aug 6-7, 2007. Pp 100-111.

[21] Wang, L., Felicelli, S., Gooroochun, Y., Wang, P., Horstemeyer, M. Optimization of the LENS® process for steady molten pool size.Mater. Sci. Eng. A. Vol 474. 2007. Pp. 148-156.

[22] Vasinonta, A., Beuth, J. Process maps for controlling residual stress and melt pool size in laser-based SFF process. Proc. 11th Solid Freeform Symposium. Austin, TX. Aug 7-9, 2000. Pp. 200-208.

[23] Allen, A., Hutchings, M., Windsor, C. Neutron diffraction methods for the study of residual stress fields. Adv. Phys. Vol 34. 1985. Pp. 445-473.

[24] Pratt, P., Felicelli, S., Wang, L., Hubbard, C. Residual stress measurements of LENS AISI 410 thin plates via neutron diffraction Met. Mat. Trans. A. 2008. (Accepted)

[25] Winholtz, R. *Analysis of Residual Stress by Diffraction using Neutron and Synchrotron Radiation*. Fitzpatrick, M. and Lodini, A., eds. Taylor and Francis, NY. 2003. Pp. 60-77.

[26] Behnken, V., Hauk, Z. Berechung der röntgenographischen elastizitätskonstanten (REK) des vielkristalls aus den einkristalldaten für beliebige kristallsymmetrie. Z. Metallkd. Vol 77. 1985. Pp. 620-626.

[27] Dever, D. J. Temperature dependence of the elastic constants in α-iron single crystals: relationship to spin order and diffusion anomalies.Appli. Phys. Vol 43. 1972. Pp. 3293-3301.

[28] Kröner, E. Berechung der elastischen konstanten des vielkristalls aus den konstanten des einkristalls.Z. Phys. Vol 5. 1958. Pp. 504-518.

[29] Smith, W. Stainless Steels in *Structures and Properties of Engineering Alloys*. 2nd Edition. McGraw-Hill. NY. 1993. p 310.

[30] Wang, L., Felicelli, S., Pratt, P. Residual stresses in LENS-deposited AISI 410 Stainless Steel Plates. Mat, Sci. Eng. A. Vol 496. 2008. P. 234-241.

[31] SYSWELD 2005 Reference Manual, ESI Group, 2005.

[32] LeBlond, J. A theoretical and numerical approach to the plastic behavior of steels during phase transformations – I. derivation of general relations. J. Mech. Phys. Solids. Vol 34. No 4. 1986. Pp. 395-409.

[33] LeBlond, J. A theoretical and numerical approach to the plastic behavior of steels during phase transformations – II. Study of classical plasticity for ideal-plastic phases. J. Mech. Phys. Solids. Vol 34. No 4. 1986. Pp. 411-432.

[34] Bammann, D., Chiesa, M., Horstemeyer, M., Weingarten, L. Failure in ductile materials using finite element method, in *Structural Crashworthiness and Failure*. Jones, N. and Weirzbicki, T., eds. Elsevier, Amsterdam. 1993. pp 1-54.

[35] Dike, J., Brooks, J., Bammann, D., Li, M. Finite element modeling of weld solidification cracking in 6061-T6 aluminum – applicability of strain-based failure criteria. Proceedings of the 2nd International Symposium on Thermal Stresses and Related Topics. Rochester, NY. 1997.

[36] Bammann, D., Prantil, V., Kumar, A., Lathrop, J., Mosher, D., Callabresi, M., Lusk, M., Krauss, G., Jou, H., Elliot, W., Ludtka, G., Dowling, W., Nikkel, D., Lowe, T., Shick, D. Development of a carburizing and quenching simulation tool: a material model for low carbon steels undergoing phase transformations. American Society of Metals 2nd International Conference on Quenching and Control of Distortion. Cleveland, OH. 1996. Pp. 367-375.

[37] Bammann, D., Prantil, V., Lathrop, J. A model of phase transformation plasticity, in Modeling of Casting, Welding and Advanced Solidification Processes VII. Cross, M., and Campbell, J., eds. TMS. 1995. Pp. 275-284.

[38] Oddy, A., McDill, J., Karlsson, L. Microstructural predictions including arbitrary thermal histories, reaustenization and carbon segregation effects. Canadian Metallurgical Quaterly. Vol 35. No 3. 1996. Pp. 137-146.

[39] *ABAQUS® Analysis User's Manual*, Version 6.7. 2007. Simulia, Inc.